Two-Dimensional Electronic Spectroscopy of the Photosystem II D1D2-cyt.*b559* Reaction Center Complex: Experiment and Simulation

by

Kristin Lee Morgenstern Lewis

A dissertation submitted in partial fulfillment
of the requirements for the degree of
Doctor of Philosophy
(Physics)
in The University of Michigan
2011

Doctoral Committee:

Assistant Professor Jennifer P. Ogilvie, Chair
Professor Eitan Geva
Professor Roseanne J. Sension
Professor Duncan G. Steel
Associate Professor Çagliyan Kurdak

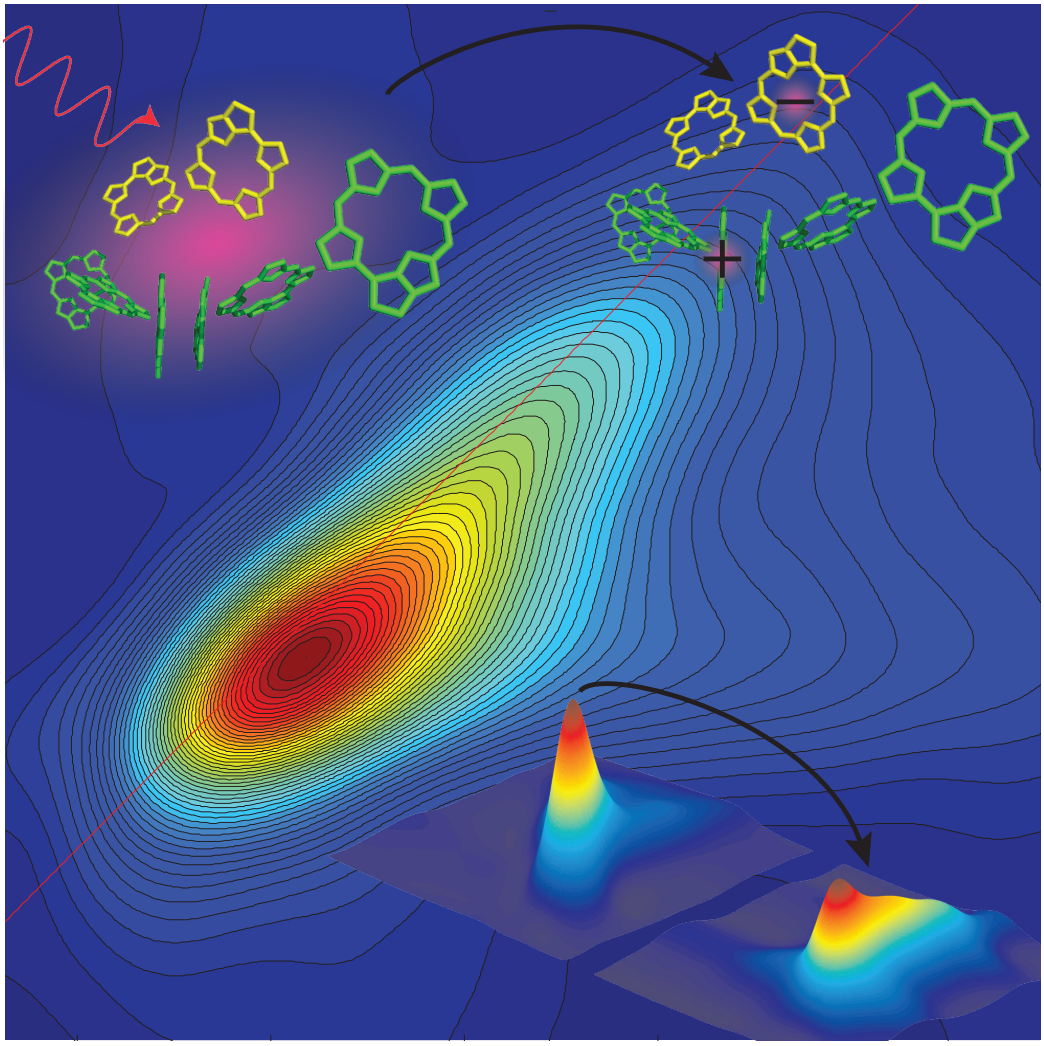

To Logan

ACKNOWLEDGEMENTS

If you would have asked me, as a high school junior, what I expected to be doing after college, physics grad school wasn't even on my radar. Chemistry, perhaps, but I didn't even want to take the physics class offered at my school. Thankfully, my parents encouraged me to sign up for the class, and Patricia Westphal ignited a love for physics I never expected to have. Her passion and skill for teaching set me on the path leading to this dissertation.

Mark Eriksson and Don Cox kept me on this path as my professors for a unique series of introductory physics classes for physics majors. As a sophomore looking to dip my toes into research, Mark's lab provided a great place for an undergraduate, and grad students Keith and Emma were terrific mentors. This lab was my academic home for the duration of my undergraduate career, and I am thankful for the headstart it gave me as a future graduate student.

A dissertation in experimental physics is rarely a solo endeavor and I have had the pleasure of working with many colleagues at the University of Michigan who have each contributed to this work in their own way. Jessica's expertise in building NOPAs and her willingness to share caffeine and apple fritters will not soon be forgotten. Meredith, while on the other side of the laser curtain or office wall, has shared conversations with me that have helped to add some balance to the work day. Brandon and Sarah, also on the other side of the curtain, have always been willing to talk through a problem, and Sarah graciously taught me how to make my own jam. Patrick pushed forward the use of a continuum probe and its challenges, and helped

solidify the analysis needed for proper scatter subtraction. Frank was always willing to delve into intense theoretical discussions, and I do not envy him the work he's done in perfecting the PSII purification prep. Dan has often had programming tips and the update to the analysis code is much appreciated. I know Frank and Dan will serve future multidimensional experiments well. Finally, Jeff, with whom I've shared far too many late nights blasting Stevie Nicks and eating sushi. This work could not have been accomplished without him.

Professor Jennifer Ogilvie herself has been a terrific advisor, and her excitement for her work shows. Upon returning from every conference, she has a few new ideas up her sleeve and is re-energized about understanding the questions before her. She is patient and encouraging, and is a great role model for an aspiring physicist.

I gratefully acknowledge the willingness of Professors Shaul Mukamel and Darius Abramavicius for hosting me in their respective institutions and for their guidance in simulating 2D spectra. Professor Eitan Geva has been helpful in leading our group through the theoretical underpinnings of nonlinear spectroscopy. Professor Charlie Yocum has been instrumental in the preparation of photosystem II samples and patient with us physicists as we tried our hands in a biological setting for the first time. Similarly, Professor Roseanne Sension shared with us the thesis of her student, Brent Donovan, which gave further insight into the materials and methods required to extract isolated reaction centers.

I thank each member of my committee, Professors Geva, Sension, Steel, and Kurdak for taking precious time to help me succeed in these final stages and to improve this work.

I thank the help of those who gave their time and sanity to proofread and edit my thesis: Frank, Laura, Jana, Logan, and Jennifer. Any errors that may have been overlooked are mine alone.

My parents have always advocated for me and both indulged and encouraged

my intellectual pursuits. I truly appreciate all the gifts they have given me: their creativity, their love of learning, and their dedication. My sister, too, for cheering me on through everything.

To Jana, for being there when I needed her and always believing in me.

And finally, Logan, who has always pushed me to achieve my goals, and for always believing in my intellectual abilities, even when I doubted them myself. I thank him for being a fixer and always helping with computational issues, from programming to compiling. Without his love and support I would not have come this far.

TABLE OF CONTENTS

LIST OF FIGURES

Figure

LIST OF TABLES

Table

LIST OF APPENDICES

Appendix

ABSTRACT

Two-Dimensional Electronic Spectroscopy of the Photosystem II D1D2-cyt.*b559* Reaction Center Complex: Experiment and Simulation

by

Kristin Lee Morgenstern Lewis

Chair: Jennifer P. Ogilvie

Oxygenic photosynthesis is key to life on this planet, and photosystem II is key to oxygenic photosynthesis. The only natural molecule capable of splitting water, it has been studied extensively with a wide range of linear and nonlinear spectroscopic methods. Still, the energy and charge transfer pathways remain poorly understood. Two dimensional electronic spectroscopy (2DES) extends previous non-linear spectroscopies into an additional frequency axis, uncovering information about electronic coupling and energy transfer that is difficult to discern in other methods.

This thesis presents technical advances to 2DES with a pulse shaper in the pump-probe geometry, particularly phase-cycling for isolating signals of interest and for reducing scatter signals. This method is applied to the first 2DES measurements of the Q_y band of the D1D2-cyt.*b559* reaction center of photosystem II (PSII RC). A new method for extracting kinetic information from such a rich data set is presented: two dimensional decay associated spectra. The 2DES data directly reveal excitonic coupling between blue and red states within the band. The rapid growth of

a cross-peak below the diagonal provides unambiguous evidence for energy equilibration within the reaction center on the order of 100 fs. Spectrally dependent lifetimes of 2-3 ps are observed, in agreement with a recent model in which charge separation occurs along two distinct pathways. Slower time constants of $\sim$7 ps and $\sim$50 ps are consistent with slow energy transfer from peripheral chlorophylls and secondary charge transfer, respectively.

The first simulations of the PSII RC are presented and compared to experiment. The simulations examine a well-tested model for the excitonic structure of the PSII RC, which provides a good description for linear absorption, linear dichroism, circular dichroism, steady-state fluorescence, triplet-minus-singlet as well as Stark spectra. The resulting simulations match neither the experimental lineshapes nor the observed kinetics, revealing the power of 2DES for constraining theoretical models. An improved version of this model is proposed that gives qualitatively better lineshapes, although still fails to predict the observed kinetics. The thesis concludes with a brief discussion of future experimental and simulation work that is needed that builds on the work presented here.

CHAPTER I

Introduction

Oxygenic photosynthesis plays a critical role in supporting life on Earth. Nearly all life on this planet subsists either on solar energy or on another organism that does (at some point in the food chain). To efficiently use solar energy, photosynthetic organisms use a variety of pigments in light-harvesting antennae to absorb frequencies that span the solar spectrum. Once the energy is collected, it must be transferred to a reaction center to be converted into long-lived charge separations and eventually to ATP or the chemical bonds within sugar. After taking such care to collect large quantities of solar energy, plants have also developed efficient energy transfer pathways from the antenna complexes to the reaction center which can have $\sim$95% quantum efficiency or greater [1].

Despite the importance oxygen evolution plays, only a single protein complex is capable of generating a redox potential large enough to split water: photosystem II (PSII) [1]. This unique complex has its own light harvesting subunits that direct energy towards the reaction center, where it is converted into a charge separation that ultimately performs water splitting. Understanding the unique properties of PSII that are responsible for this capability and the extremely high efficiency of energy transfer are of great interest, not least because of the potential applications for the field of solar energy and artificial photosynthesis [2–5].

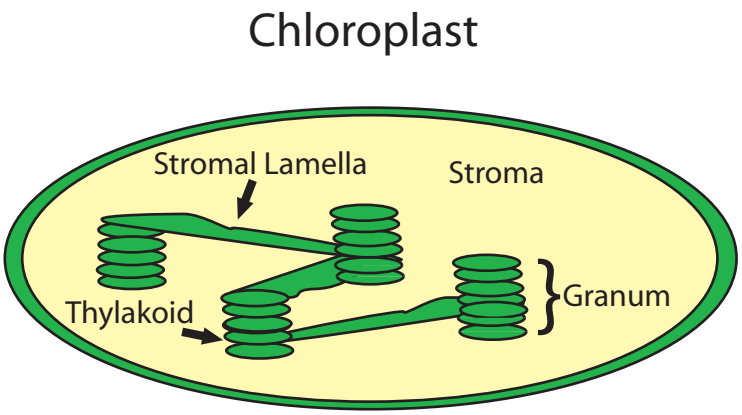

Figure 1.1: Cartoon showing the structure of the chloroplast [6].

1.1 Photosystem II: structure and function

1.1.1 Structural context

In higher plants, photosynthesis within the cell occurs in an organelle called the chloroplast. These organelles are responsible for harvesting solar energy and storing it within chemical bonds. The chloroplast has its own internal structure, shown in Figure 1.1. The organelle is filled with a fluid called the stroma. The proteins responsible for photosynthesis reside in the thylakoid membrane, which forms vesicles. These can form folded stacks of disc-liked membranes called grana, or they can be unfolded as stromal lamellae and span the regions between grana. Photosystem II is preferentially found in the grana, a fact that is exploited when extracting and purifying photosystem II (see Appendix A), while photosystem I resides primarily in the stromal lamellae. Cytochrome b_6f, another membrane-bound protein in the photosynthetic process is found throughout the thylakoid.

1.1.2 Functional context

Briefly, photosynthesis follows the "Z-scheme," involving a combination of light and dark reactions, summarized in Figure 1.2. The process begins with photoexcita-

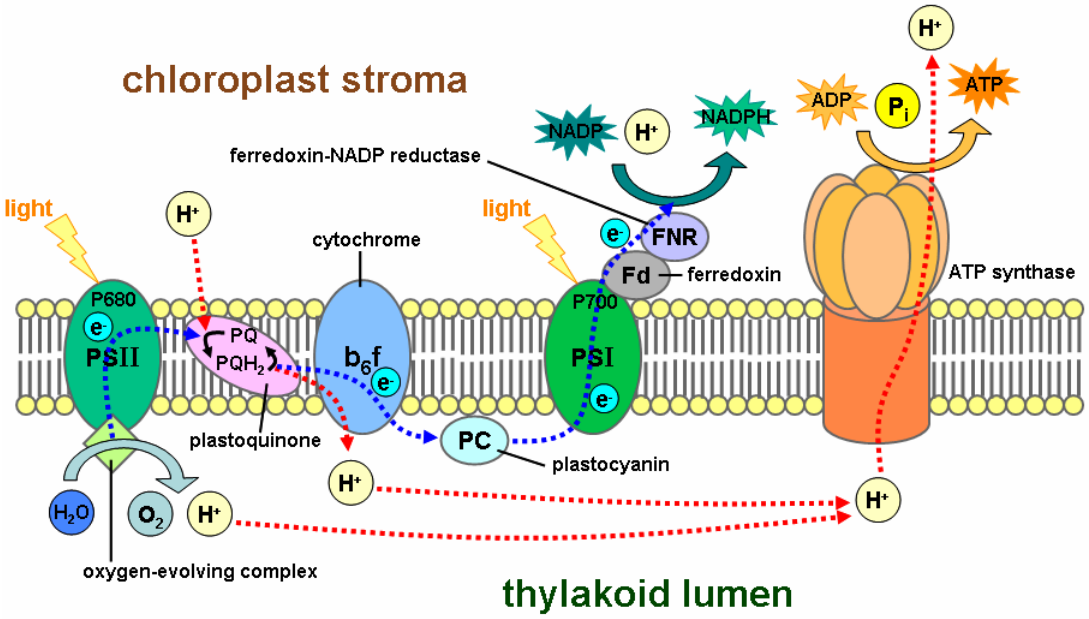

Figure 1.2: Z-scheme of photosynthesis [7].

tion of photosytem II. This causes a charge-separated state with a quinone molecule as the final electron acceptor. When the quinone is doubly reduced, PSII is able to split water via the oxygen evolving complex (OEC). The quinones reside near the stromal surface where they combine with hydrogen ions and are transported to cytochrome b_6f, which acts as a proton pump, returning the quinones to their original state and creating a pH gradient across the thylakoid membrane. The additional electrons are passed to photosystem I, which, in conjunction with its own photoexcitation event, converts NADP into NADPH, an intermediate electron acceptor. Meanwhile, ATP synthase takes advantage of the pH gradient to convert ADP into in ATP. Carbohydrates are produced through a series of dark reactions called the Calvin cycle [1].

The photosynthetic process is a complicated one, involving many different time scales: from the ultrafast energy and charge processes within photoystem II and photosystem I, to the slow processes involving carbohydrate creation. Entire books have been written about the processes within the photosystem II complex alone [8].

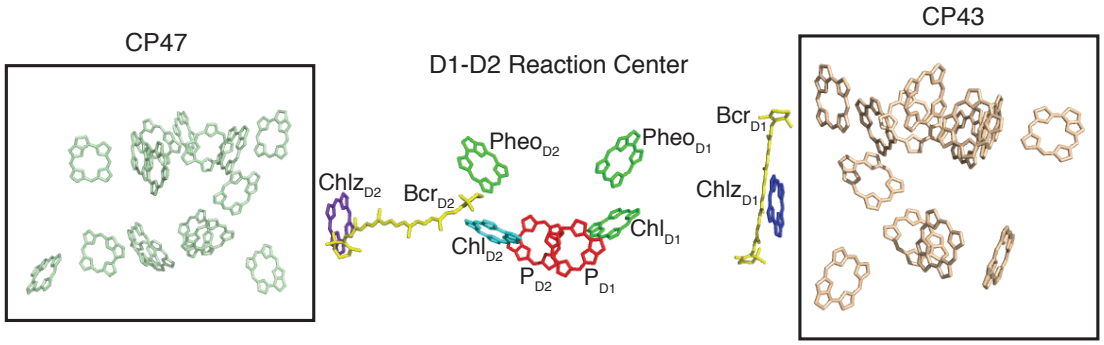

Figure 1.3: The crystal structure of photosystem II chromophores within the D1D2-cyt.*b559* reaction center and the CP43 and CP47 light harvesting subunits [9].

This dissertation cannot hope to address the energy and charge transfer processes within the whole of photosynthesis; instead, we focus our attention on the very first steps involving the excitation of the D1D2-cyt.*b559* reaction center, and the primary photophysical processes that occur therein. Our goal is to understand the relationship between the structure of the D1D2-cyt.*b559* reaction center and its function: what role do the different pigments play in determining the pathways and timescales of energy and charge transfer leading to the initial charge-separated state?

1.1.3 Reaction center details

The photosystem II complex contains over 250 chlorophylls within more than 25 subunits. The majority of these chlorophylls are involved in light harvesting antennae that funnel absorbed solar energy toward the reaction center. The antenna complexes most closely associated with the reaction center are CP43 and CP47. The pigments of CP43, CP47 and the reaction center are shown in Figure 1.3. A recent 1.9 Å crystal structure provides a detailed picture of the internal structure [10]. Stripping away the CP43 and CP47 leaves only the D1D2-cyt.*b559* reaction center, which contains 6 chlorophyll molecules, two pheophytins and one or two β-carotenes [11, 12]. The quinones mentioned above in the discussion of the Z-scheme are also stripped away

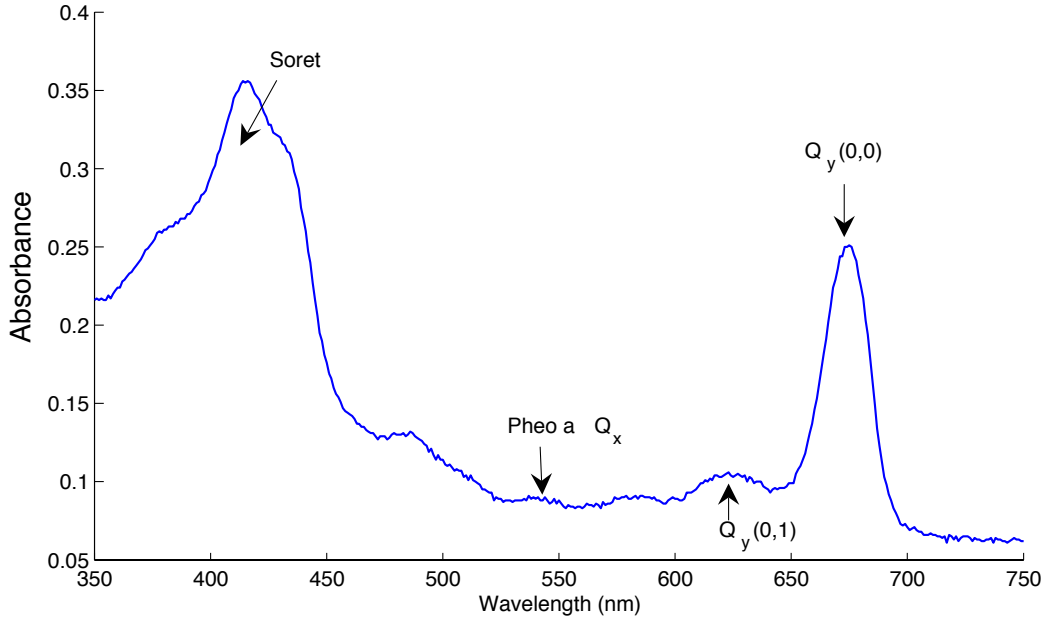

Figure 1.4: Absorption spectrum of room temperature D1D2-cyt.*b559* reaction centers.

in the D1D2-cyt.*b559* reaction center preparation, leaving a pheophytin as the final electron acceptor. The reaction center is roughly mirrored in two branches, named for their protein subunit scaffold: the D1 branch and the D2 branch. As in the bacterial reaction center, the charge separation process occurs only along one branch of the system; in photosystem II this is the D1 branch.[1]

The room temperature absorption spectrum of photosystem II is shown in Figure 1.4 and is composed of many different spectral bands. The Q_y band occurs around 680 nm and is the main focus of this dissertation. Here, we find the primary absorption from the $\pi \rightarrow \pi^*$ transitions of both the chlorphyll a and pheophytin a molecules. With 8 contributing pigments that have absorption in this region, it is quite spectrally congested, and difficult to resolve the contribution from any single pigment. At 77K, the Q_y band partially resolves into two peaks, but the congestion is still strong, and the situation does not improve much even at significantly lower temperatures. The

[1]For a full discussion of the evidence for transfer along a single branch, see the review by Rappaport and Diner [13].

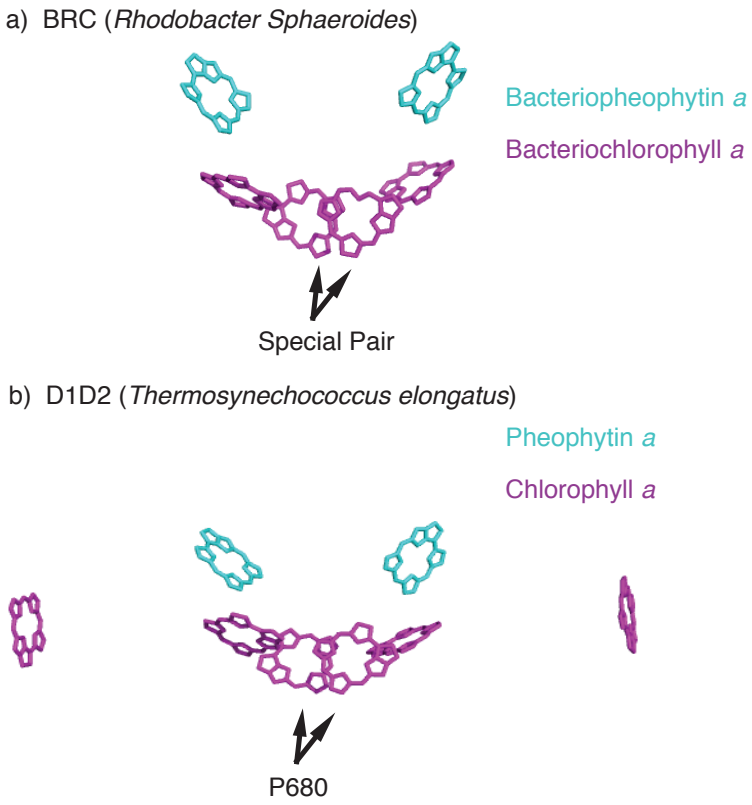

Figure 1.5: The crystal structure of the bacterial reaction center [17] and the similar reaction center of photosystem II [9].

Soret band from 400-450 nm is primarily used for pigment stoichiometry and sample purity measurements, as the ratio of the absorption at 416 nm and 435 nm can give information about the chlorophyll/pheophytin ratio [14].

The reaction center of photosystem is often compared to the bacterial reaction center (BRC), and the crystal structures reveal striking similarities, as seen in Figure 1.5. The central 6 chromophores (chlorophyll a and pheophytin a in PSII and bacteriochlorophyll a and bacteriopheophytin a in the BRC) share the same basic structure, while PSII contains two additional chlorophyll molecules on the periphery of the reaction center. These are believed to facilitate energy transfer from external light harvesting antennae. Since the BRC was crystallized first [15] and initially to a higher resolution [16], it was often used as a proxy for understanding PSII.

Despite the structural similarities of the two reaction centers, they exhibit marked spectral differences. Unlike chlorophyll *a* and pheophytin *a*, bacteriochlorophyll *a* and bacteriopheophytin *a* have distinct Q_y absorption bands. Additionally, the two central bacteriochlorophylls form a so-called special pair in the bacterial reaction center. They are quite strongly electronically coupled, leading to significant spectral splitting, such that there is a distinct spectral band due to the special pair. Combined with the earlier crystal structure, these facts have led to a more complete understanding of the BRC. The spectral congestion in PSII complicates the interpretation of spectroscopic data, and limits the ability to spectrally select excitation of one particular pigment over another.

1.2 Previous spectroscopic studies

A large number of studies have aimed to determine the primary energy and charge transfer events in the D1D2-cyt.*b559* reaction center. Methods of study include transient absorption (TA) [18–40], time resolved fluorescence (TRF) [33, 41–47], spectral hole burning (SHB) [48–55], and two-pulse photon echo (2PE) [53, 55–57]. While low temperature studies are useful for the partial spectral resolution of the Q_y band, other studies are done at room temperature to provide more physiological conditions. To this large body of work, this dissertation adds the first measured two-dimensional electronic spectra of the reaction center at 77K [58].

The D1D2-cyt.*b559* reaction center is the smallest component of photosystem II that undergoes primary charge separation. Without the overlapping spectral contributions from nearby light-harvesting antennae, studying this isolated system simplifies the interpretation and assignments of spectroscopic signatures. The purification procedure used to extract the D1D2-cyt.*b559* reaction center, however, is harsh, and some question whether the photophysical properties of the isolated system are representative of the intact photosystem [59, 60]. To this end, "core" complexes can also

be purified from photosystem II; these contain the D1D2-cyt.*b559* reaction center, as well as the CP43 and CP47 antenna complexes. Comparative studies of the D1D2-cyt.*b559* reaction center and core complexes indicate that the primary and charge transfer events in the isolated reaction center are representative of the larger complex [40].

1.2.1 Charge transfer

Early models of the charge transfer process in photosystem II were based on the analogous process in the bacterial reaction center, where the "special pair" is the initial electron donor, and the electron subsequently hops to Chl_{D1} and then to $Pheo_{D1}$ [61]. More recently, a low temperature photon echo experiment on the isolated reaction center suggested that Chl_{D1} was the primary electron donor [56], and this has been supported by a wide variety of experiments at room temperature [37, 40], low temperature [51], ones using site-directed mutants [62], as well as theory [63, 64] (see Figure 1.6). Recent transient absorption work has suggested two potential charge transfer pathways such that the static disorder within complex dictates which pathways is more favorable [39] (see Figure 1.7). The two-pathways model has been supported through modeling of the transient absorption kinetics of Pheo Q_x and $Pheo^-$ bands at 545 nm and 460 nm, respectively [65].

A summary of the major experimental results regarding charge transfer can be found in Table 1.1, adapted from the reviews of Wasielewski [66] and Sension [61] to include recent research. Many of the studies have used dithionite-treated samples to support their conclusions. Treating the PSII reaction center with dithionite pre-reduces the pheophytin, effectively blocking charge transfer to that pigment. There have been some discrepancies in the time scales reported with early studies showing values in the tens of picoseconds. More recent studies have settled on values from ∼1-3 ps for primary charge transfer events. Still, it is unclear whether charge transfer

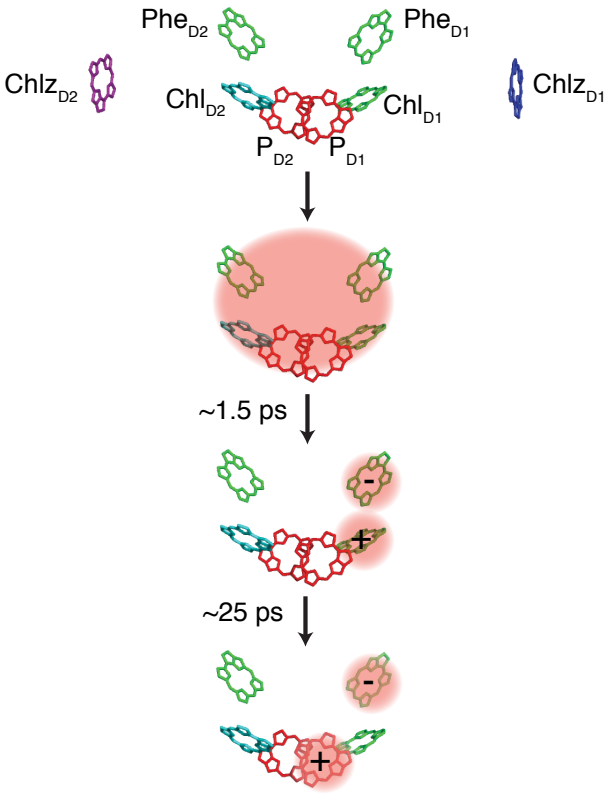

Figure 1.6: The charge transfer pathway of Prokhorenko and Holzwarth [56] overlaid on the 2.9 Å crystal structure [9].

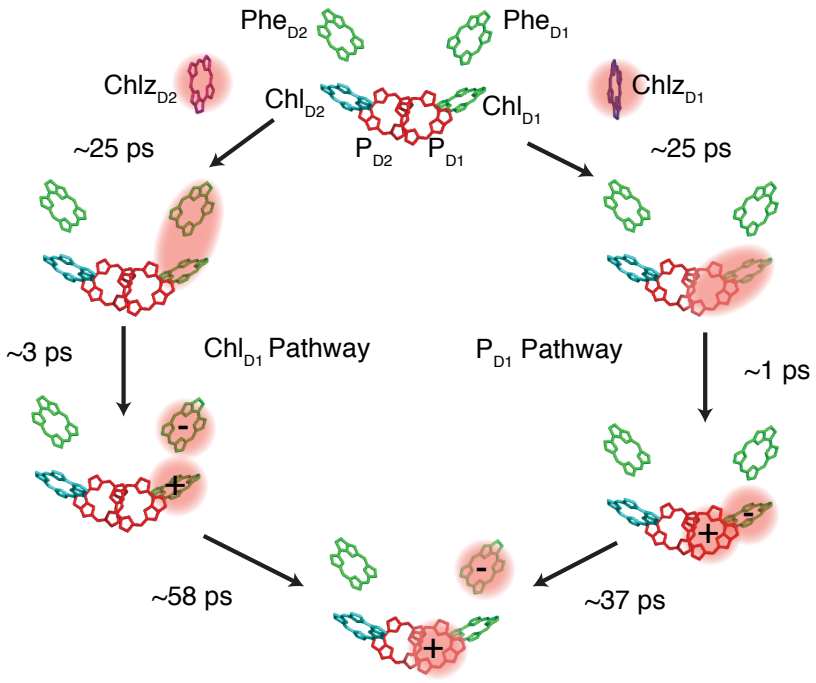

Figure 1.7: Two charge transfer pathways overlaid on the 2.9 Å crystal structure [9], as proposed by Romero et al. [39]

occurs via one pathway or two, and if it is a single pathway, which chromophore is the primary electron donor.

Table 1.1: Major experiments on charge transfer

Results	Basis	Reference
Charge transfer time ∼2 ps at low temperature	TA at Q_y, ion bands (490 and 820 nm) and Q_y(0,1) stimulated emission sideband supported by dithionite reduction (15 K)	Wasielewski et al. 1989a [21]
	Transient hole burning (4 K)	Jankowiak et al. 1989 [49]
	TA at Q_y band (77 K)	Visser et al. 1995 [67]
	TA excitation 661 / 683 nm, probing at Q_x band (7 K)	Greenfield et al. 1999 [34]
	Time-resolved fluorescence (77 K)	Konermann et al. 1997 [44]
	Two-pulse photon echo at Q_y band (1.3 K)	Prokhorenko and Holzwarth 2000 [56]
Charge transfer time ∼3 ps near room temperature	TA at Q_y and ion bands (485 and 820 nm), supported by dithionite reduction	Wasielewski et al. 1989b [20]
	Picosecond fluorescence	Roelofs et al. 1991 [43]; Holzwarth et al. 1994 [33]

Table 1.1: Major experiments on charge transfer (cont)

Results	Basis	Reference
	TA at Q_y band, ion band (820 nm) and Pheo *a* bleach supported by dithionite reduction	Wiederrecht et al. 1994 [27]
	TA of the Q_y band	Schelvis et al. 1994 [23]
	TA excitation 687 nm, probing at Q_x band	Greenfield et al. 1997 [68]
	Time-resolved fluorescence	Gatzen et al. 1996 [45]
	Time-resolved fluorescence	Donovan et al. 1997 [47]
	Time-resolved fluorescence (red excitation)	van Mourik et al. 2004 [41]
	TA at Q_y band	Holzwarth et al. 2006 [40]
	TA at mid-infrared frequencies	Pawlowicz et al. 2007 [35]
Charge transfer time ∼20 ps near room temperature	TA at Pheo *a* bleach	Hastings et al. 1992 [24]; Klug et al. 1995 [30]
	TA at $Q_y(0,1)$ stimulated emission sideband	Durrant et al. 1993 [25]; Klug

Table 1.1: Major experiments on charge transfer (cont)

Results	Basis	Reference
		et al. 1995 [30]
	TA at Q_y band, Pheo *a* bleach, and Q_y(0,1) stimulated emission sideband	Donovan et al. 1996 [31]
	TA pumping at Q_y band, probing at Q_y and Q_x	Müller et al. 1996 [29]
Charge transfer at both $\sim$ 3 and $\sim$ 21 ps near room temperature	TA at Q_y band, including sideband. Excitation at 665, 680, and 694 nm. 3 ps and 21 ps CT times found	Merry et al. 1996 [38]
	Fluorescence upconversion	Kumazaki et al. 1995 [69]
Charge transfer at 0.4-2.6 ps as a function of temperature	TA at Q_y band. Excitation 685 nm (20 K, 77 K, 110 K, 150 K, 240 K)	Groot et al. 1997 [36]

Table 1.1: Major experiments on charge transfer (cont)

Results	Basis	Reference
Initial separation from $Chlz_{D1}$ in 0.6-0.8 ps, P^+H^- after 6 and 36 ps	TA with visible pump (669nm and 681nm) with mid-IR probe	Groot et al. 2005 [37]
Charge transfer at 4.6 ps at low temp	Triplet bottleneck hole burning	Jankowiak et al. 2003 [54]
Two distinct CT pathways with times of 1 ps and 3 ps at low temperature	TA excited at the Q_y band, probed at Q_y, Pheo Q_x and Pheo anion bands (77 K)	Romero et al. 2010 [39]

1.2.2 Energy transfer

Energy transfer within the reaction center occurs on multiple time scales, from sub-picosecond to nanoseconds [70]. Similar results from different experiments have led to significantly different interpretations [40, 61] largely due to the overlapping features [40, 71] and the heterogeneous nature of the system. This implies that a more restrictive data set is needed for less ambiguous interpretation. Major experimental results are found in Table 1.2, again, adapted from the reviews of Wasielewski [66] and Sension [61] to include recent research.

Many transient absorption studies have found kinetics with a sub-picosecond component under varying excitation conditions, both at room temperature [18, 19, 26, 29, 30, 38, 72] and at low temperature [67]. This component was first interpreted to be rapid energy equilibration with a time constant of ∼100 fs in the reaction center [26]. This was supported by future transient absorption studies [30, 38] and modeling [56]. Müller et al. found a time constant of ∼300 fs necessary to fit kinetics [29], although they also suggest the fast component found by Klug et al. [30] may be caused by exciton-exciton annihilation effects [72].

Schelvis et al. disputed the equilibration interpretation based on their room temperature transient absorption work where they concluded that equilibration would take longer than 30 ps [23]. Instead, they interpret the sub-picosend kinetics to be relaxation from $S_n \rightarrow S_1$ states, as discussed in the work of McCauley et al. [18].

Transient absorption spectroscopy requires a compromise between spectral selectivity and temporal resolution. When studies try to selectively excite a portion of the Q_y band, the narrowband pulses used are inherently longer due to the Fourier relation between spectral bandwidth and temporal width. For instance, a pulse centered at 680 nm with a bandwidth of 5 nm will be unable to resolve kinetics on the ∼100 fs timescale. I show in Chapter II how two dimensional spectroscopy is able to maintain spectral selectivity and high temporal resolution.

Table 1.2: Major experiments on excitation energy transfer

Results	Basis	Reference
Excitation energy transfer in tens of picoseconds at low temperature	TA at Q_y band (15 K)	Wasielewski et al. 1989a [21]
	Persistent hole burning (4 K)	Tang et al. 1990 [48]
	Picosecond fluorescence (15-150 K)	Roelofs et al. 1993 [46]
	Picosecond fluorescence (77 K)	Freiberg et al. 1994 [42]
	TA at Q_y band comparing 670.5 and 672-nm with 681 and 688-nm excitation wavelengths (77 K)	Visser et al. 1995 [67]
	Persistent non-photochemical hole burning (NPHB) and triplet bottleneck hole burning (TBHB) (5 K)	Zazubovich et al. 2003 [53]
	TA excited at the Q_y band, probed at Q_y, Pheo Q_x and Pheo anion bands (77 K)	Romero et al. 2010 [39]

Table 1.2: Major experiments on excitation energy transfer (cont)

Results	Basis	Reference
Subpicosecond excitation energy transfer at low temperature	TA at Q_y band using 670.5 nm and 672 nm excitation (77 K)	Visser et al. 1995 [67]
	TA excitation 661 / 683 nm, probing at Q_x band (7 K)	Greenfield et al. 1999 [34]
	Time-resolved fluorescence (77 K)	Konermann et al. 1997 [44]
	Two-pulse photon echo at Q_y band (1.3 K)	Prokhorenko and Holzwarth 2000 [56]
	TA excited at the Q_y band, probed at Q_y, Pheo Q_x and Pheo anion bands (77 K)	Romero et al. 2010 [39]
Excitation energy transfer in tens of picoseconds near room temperature	Picosecond fluroescence	Roelofs et al. 1991 [43]; Holzwarth et al. 1994 [33]
	TA at Pheo *a* bleach and Q_y band comparing 665 nm and 694 nm excitation	Rech et al. 1994 [22]

Table 1.2: Major experiments on excitation energy transfer (cont)

Results	Basis	Reference
	TA at Q_y band comparing 662 and 687-nm excitation wavelengths	Schelvis et al. 1994 [23]
	TA at Pheo *a* bleach comparing 665 nm and 683 nm excitation	Greenfield et al. 1996 [32]
	TA pumping at Q_y band, probing Q_y and Q_x	Müller et al. 1996 [29]
	TA excitation 687 nm, probing at Q_x band	Greenfield et al. 1997 [68]
	Time-resolved fluorescence	Gatzen et al. 1996 [45]
	Time-resolved fluorescence	Donovan et al. 1997 [47]
	Time-resolved fluorescence (red excitation)	van Mourik et al. 2004 [41]
	TA at Q_y band	Holzwarth et al. 2006 [40]
	TA at mid-infrared frequencies	Pawlowicz et al. 2007 [35]

Table 1.2: Major experiments on excitation energy transfer (cont)

Results	Basis	Reference
Subpicosecond equilibration of excitation energy between accessory Chl *a* and P680 near room temperature	TA at Q_y band comparing 665 and 694-nm excitation wavelengths	Durrant et al. 1992 [26]
	TA pumping at Q_y band, probing Q_y and Q_x	Müller et al. 1996 [29]
	TA at Q_y band, including sideband, excitation at 665,680, and 694 nm	Merry et al. 1996 [38]
Energy transfer between 680-686 nm at ∼5 - 10 ps	Persistent non-photochemical hole burning (NPHB) and triplet bottleneck hole burning (TBHB) (5 K)	Zazubovich et al. 2003 [53]
Excitation energy transfer in the tens of ps as a function of temperature	TA at Q_y band. Excitation 685 nm (20 K, 77 K, 110 K, 150 K, 240 K	Groot et al. 1997 [36]

1.3 Modeling background

Work on photosystem II began with phenomenological models to describe the energy and charge transfer processes observed. The PSII complex had been quite difficult to crystalize for structural measurements, so the similarly-structured and well-studied bacterial reaction center was often used as a proxy to fill in missing details of the model [15, 73], even though the bacterial system exhibits significantly different spectral behavior. The electronic coupling of the "special pair" (P680 or P_{D1} and P_{D2}) of the PSII reaction center was thought to be more weakly electronically coupled than that of the BRC. When early crystal structures for PSII reported a center-center distance of 10 Å for P680 [74], this was compared to the 7.6 Å distance found in the BRC special pair [75], and suggested as a mechanism for the weaker coupling. A new crystal structure of PSII with 1.9 Å resolution gives a center-center distance of 8 Å, much more similar to that of the BRC [10]. Therefore, we must consider other possibilities for the weaker coupling observed in PSII.

In moving away from the interpretation of the photosystem II reaction center primarily as a dimer (P680), Durrant et al. created the multimer model of photosystem II, where the central 6 chromophores were considered to be iso-energetic with static diagonal disorder [73]. Since then, much of the modeling of photosystem II has been based on this multimer model, with some models retaining identical transition energies for the central 6 pigments [64, 76, 77] and others adding variations to the individual pigment electronic transistions [63, 78–80].

Ivashin and Larsson [79] have produced the only model of the electronic structure of the photosystem II reaction center to be solely based on quantum chemical calculations from a crystal structure [81]. The agreement to experimental spectra is poor, although higher-resolution structures may improve the agreement. Raszewski et al. [80] use quantum chemical calculations from a slightly higher resolution crystal structure [82] to extract couplings between the chromophores, but still allow the local

transition energies to fluctuate to fit optical spectra, giving a better agreement to experimental data than that of Ivashin and Larsson. With the publication of a 1.9 Å crystal structure [10], the pigment orientations have become more clear, and will provide a better starting start for models using quantum chemical calculations.

The models of Novoderezhkin et al. [83, 84] have been derived using a genetic algorithm approach to find site energies that, when coupled through dipole-dipole interactions as dictated by crystal structure, provide good agreement with a host of linear spectroscopies including linear absorption, linear dichroism, circular dichroism, steady-state fluorescence, triplet-minus-singlet and Stark spectroscopy. In addition to the site energies, Novoderezhkin et al. also introduce a single charge transfer state, $P_{D2}^{+}P_{D1}^{-}$, and treat it similarly to a chromophoric state in the Hamiltonian, with coupling only to its constituent pigments. The motivation for introducing the charge transfer state comes from Stark experiments that indicated at least one low lying charge transfer state [85]. Alone, the charge transfer state has no dipole strength, but it becomes weakly allowed when mixed with the excitonic states of the pigments. A representation of this model is shown in Figure 1.8 and we simulate 2D spectra using this model in Chapter V. Raszewski et al. take a different approach; while they do not include a charge transfer state, they calculate variations of a model where a state is charged, and use electrochromic shifts to calculate difference spectra [63, 80]. Both models have been successful at modeling a variety of linear spectra.

Both the above models use modified Redfield theory [86] for calculating transport rates between excitons.[2] Modified Redfield theory is used for simulating condensed-phase systems in the intermediate system-bath and Coulombic coupling regime. It bridges the gap between strong (Redfield) and weak (Förster) Coulombic coupling and approaches the results of both in the appropriate limits [87]. It is discussed further in Chapter V.

[2]The Renger model also includes modified Förster theory to calculate transfer from the peripheral chlorophylls.

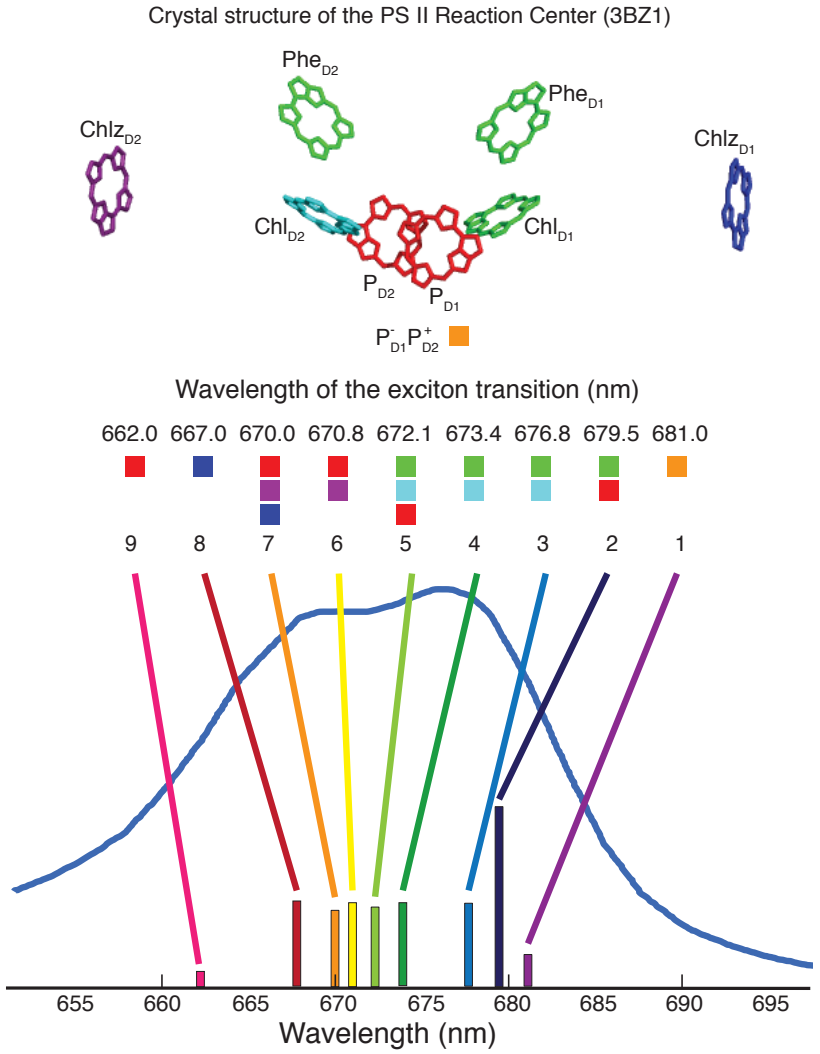

Figure 1.8: The crystal structure [9] with color-coding according to the model of Novoderezhkin et al. The colored boxes indicate which chromophores participated in which excitonic state. The linear absorption spectrum shown is extracted from Figure 6 of [84] and has bars underneath indicating exciton transitions and strengths.

Novoderezhkin et al. [65] have recently modeled the transient absorption data of Romero et al. [39], which forms the basis for the multiple charge transfer pathway model. They successfully model the 77K TA kinetics of the Pheo Q_x and $Pheo^-$ bands at 545 nm and 460 nm by incorporating additional charge transfer states in their model. Curiously, the assignment of which pathway is the faster of the two (the Chl_{D1} pathway or the P_{D1} pathway) changes between the two papers. Additionally, the authors do not state how this model compares to their previous model [84] for matching linear spectra.

More recently, Abramavicius and Mukamel have developed a new method for incorporating charge transfer states in the context of a tight-binding electron-hole model [88]. This method has great potential for elucidating the spectral signatures of various charge transfer states, yet the additional parameters available will require significant optimization to match the behavior of available data.

1.4 Unresolved questions

Despite extensive work towards understanding the structure-function relationship in the D1D2-cyt.*b559* reaction center, there is still no consensus about the primary charge separation and energy transfer pathways and the role of individual pigments in these processes. Still, recent transient absorption work has suggested two potential charge transfer pathways such that the static disorder within complex dictates which pathways is more favorable [39]. With two potential charge transfer pathways, which pathway is faster is not yet clear [39, 65], nor is whether both pathways are active at room temperature. Another open question regards a sub-picosecond decay in the 680-684 nm region, where there is disagreement about the origin of this feature. Prokhorenko et al. suggest that this decay component is due to rapid energy equilibration of the system based on 2 pulse photon echo experiments [56]. Hole burning studies, on the other hand have attributed this component to phonon relaxation

processes [53].

The models of the D1D2-cyt.*b559* reaction center are not sufficiently constrained. Multiple models are able to match linear spectroscopies despite having fundamentally different constructions and parameters. With the two dimensional electronic spectroscopy experiments in this thesis we aim to provide a more stringent test of current models.

1.5 Outline of the thesis

In the rest of this dissertation, I seek to provide new insight into our understanding of the energy and charge transfer processes within the photosystem II reaction center, through experimental data as well as numerical modeling. I discuss the formalisms and setups necessary to complete this work, and present results within the context of current literature.

Chapter II explains the fundamentals of two-dimensional electronic spectroscopy (2DES) used in this work to provide a more sensitive probe of the temporal and spectral behaviors of the D1D2-cyt.*b559* reaction center. I discuss the information content in third-order spectroscopies, and provide and discuss the methods used to understand third-order methods. I review phase matching, which allows for spatial separation of various third order signals. I give examples of the pathways contributing to each signal direction. I provide examples of 2D spectra for different cases, discussing features of 2D spectroscopy that are of particular importance for the work in this dissertation. Finally, I discuss transient absorption spectroscopy in its relation to 2DES.

In Chapter III, I detail the experimental setup. I start with the laser source and describe how to use an oscillator to create tunable visible pulses or a continuum pulse. Next, I elaborate on the manipulations applied for compressing, shaping, and characterizing these pulses. I show how each of the characterized pulses come together

to create a two-dimensional electronic spectrometer in the pump-probe geometry. In this section, I include a discussion of a scatter reduction technique we developed based on a combination of phase cycling and probe chopping. In this geometry, multiple signal pathways are collected simultaneously, and I demonstrate how to separate the rephasing and non-rephasing signals. Finally, I discuss the experimental difficulties in creating an optical cell at cryogenic temperatures and detail a method for cleaning and preparing windows that is necessary to prevent thorough cracking of the sample.

Two dimensional electronic spectra of the D1D2-cyt.*b559* reaction center are shown in Chapter IV. I give the experimental conditions used to acquire the data presented, and discuss additional data treatment beyond that given in Chapter III. The 2DES for the photosystem II reaction center are presented, and notable features of the data are described. Given the sometimes subtle differences in the 2D spectra, we developed a new method for extracting quantitative kinetic details of the system. The construction of two dimensional decay associated spectra (2D DAS) is described, and we analyze the data set by monitoring the exponential decay as a function of both the excitation and detection frequency. I conclude the chapter with a discussion of our results in the context of recent work.

Chapter V outlines the theory involved with modeling nonlinear spectroscopies. I describe two different methods for incorporating interactions between the system and the bath in a perturbative manner. I outline the method for calculating third-order responses, particularly for 2DES within the context of the doorway-window approach. This chapter also contains 2D simulations based on a recent model in the literature and provides and a revised model we created to better match the lineshapes of our 2D data. The chapter ends with suggestions for future improvements to the modeling.

The final chapter gives a final discussion of the work completed by our group and the important results from this dissertation. I briefly discuss future areas of interest to better understand photosystem II through studies employing a continuum probe,

and a novel photosystem II containing primarily chlorophyll *d*.

The appendices that follow provide supporting details for the results given in the dissertation. Appendix A discusses the preparation of the D1D2-cyt.*b559* reaction center as well as preliminary work on purifying an analogous complex from *Acaryochloris marina*. Appendix B gives expressions necessary for calculating the optical response given in Chapter V, while Appendix C gives information necessary for using the simulation software, SPECTRON. Attempts to reproduce an additional model from the literature are given in Appendix D, and preliminary work on a chemically reduced PSII sample is given in Appendix E.

References

[1] R. Blankenship. *Molecular Mechanisms of Photosynthesis*. Blackwell Sciences, Oxford, UK, 2002.

[2] K. Kalyanasundaram and M. Graetzel. Artificial photosynthesis: biomimetic approaches to solar energy conversion and storage. *Current opinion in biotechnology*, 21(3):298–310, 2010.

[3] Special issue on artificial photosynthesis and solar fuels. *Accounts of Chemical Research*, 42(12), 2009.

[4] J. H. Alstrum-Acevedo, M. K. Brennaman, and T. J. Meyer. Chemical approaches to artificial photosynthesis. 2. *Inorganic chemistry*, 44(20):6802–6827, 2005.

[5] R. E. Blankenship. Recognizing the potential for improvement comparing photosynthetic and photovoltaic efficiencies and recognizing the potential for improvement comparing photosynthetic and photovoltaic efficiencies and comparing photosynthetic and photovoltaic efficiencies and recognizing the potential for improvement. *Science*, 322(805), 2011.

[6] J. A. Myers. *Two-dimensional electronic spectroscopy of the photosystem II D1D2-cyt.*b559 *reaction center complex*. PhD thesis, University of Michigan, 2010.

[7] Public domain. Thylakoid membrane. Retrieved on 2 September 2011 from `http://en.wikipedia.org/wiki/File:Thylakoid_membrane.png`.

[8] T. J. Wydrzynski and K. Satoh, editors. *Photosystem II: The Light-Driven Water:Plastoquinone Oxidoreductase*. Springer, 2005.

[9] A. Guskov, J. Kern, A. Gabdulkhakov, and M. Broser. Cyanobacterial photosystem II at 2.9-Å resolution and the role of quinones, lipids, channels and chloride. *Nature structural & molecular biology*, Jan 2009.

[10] Y. Umena, K. Kawakami, J.-R. Shen, and N. Kamiya. Crystal structure of oxygen-evolving photosystem II at a resolution of 1.9Å. *Nature*, 473(7345):55–60, May 2011.

[11] C. Eijckelhoff and J. P. Dekker. Determination of the pigment stoichiometry of the photochemical reaction center of photosystem II. *Biochimica et Biophysica Acta-Bioenergetics*, 1231(1):21–28, 1995.

[12] M. Kobayashi, H. Maeda, T. Watanabe, H. Nakane, and K. Satoh. Chlorophyll *a* and β-carotene content in the D1/D2/cytochrome b-559 reaction center complex from spinach. *FEBS Letters*, Jan 1990.

[13] F Rappaport and B Diner. Primary photochemistry and energetics leading to the oxidation of the (Mn)4Ca cluster and to the evolution of molecular oxygen in photosystem II. *Coordination Chemistry Reviews*, Jan 2008.

[14] C. Eijckelhoff, H. van Roon, M. L. Groot, R. van Grondelle, and J. P. Dekker. Purification and spectroscopic characterization of photosystem II reaction center complexes isolated with or without Triton X-100. *Biochemistry*, 35(39):12864–12872, 1996.

[15] J. Deisenhofer, O. Epp, K. Miki, R. Huber, and H. Michel. Structure of the protein subunits in the photosynthetic reaction centre of *Rhodopseudomonas viridis* at 3Å resolution. *Nature*, Jan 1985.

[16] M. H. B. Stowell, T. M. McPhillips, D. C. Rees, S. M. Soltis, E. Abresch, and G. Feher. Light-induced structural changes in photosynthetic reaction center: Implications for mechanism of electron-proton transfer. *Science*, 276(5313):812–816, 1997.

[17] Dmitrij Frolov, May Marsh, Lucy I Crouch, Paul K Fyfe, Bruno Robert, Rienk van Grondelle, Andrea Hadfield, and Michael R Jones. Structural and spectroscopic consequences of hexacoordination of a bacteriochlorophyll cofactor in the *Rhodobacter sphaeroides* reaction center,. *Biochemistry*, 49:1882–1892, 2010.

[18] S. McCauley, A. Baronavski, and M. Rice. A search for subpicosecond absorption components in photosystem II reaction centers. *Chemical Physics Letters*, Jan 1992.

[19] J. R. Durrant, G. Hastings, Q. Hong, and J. Barber. Determination of P680 singlet state lifetimes in photosystem two reaction centres. *Chemical Physics Letters*, Jan 1992.

[20] M. R. Wasielewski and D. Johnson. Determination of the primary charge separation rate in isolated photosystem II reaction centers with 500-fs time resolution. *Proceedings of the National Academy of Sciences*, Jan 1989.

[21] M. R. Wasielewski, D. G. Johnson, C. Preston, and M. Seibert. Determination of the primary charge separation rate in photosystem II reaction centers at 15 K. *Photosynthesis Research*, 22(1):89–99, 1989.

[22] T. Rech, J. R. Durrant, D. M. Joseph, J. Barber, G. Porter, and D. R. Klug. Does slow energy-transfer limit the observed time constant for radical pair formation in photosystem-II reaction centers. *Biochemistry*, 33(49):14768–14774, Dec 13 1994.

[23] J. P. M. Schelvis, P. I. Van Noort, T. J. Aartsma, and H. J. van Gorkom. Energy transfer, charge separation and pigment arrangement in the reaction center of photosystem II. *Biochimica et Biophysica Acta*, Jan 1994.

[24] G. Hastings, J. R. Durrant, J. Barber, G. Porter, and D. R. Klug. Observation of pheophytin reduction in photosystem 2 reaction centers using femtosecond transient absorption-spectroscopy. *Biochemistry*, 31(33):7638–7647, Aug 25 1992.

[25] J. R. Durrant, G. Hastings, D. M. Joseph, J. Barber, G. Porter, and D. R. Klug. Rate of oxidation of P680 in isolated photosystem-2 reaction centers monitored by loss of chlorophyll stimulated-emission. *Biochemistry*, 32(32):8259–8267, Aug 17 1993.

[26] J. R. Durrant, G. Hastings, and D. Joseph. Subpicosecond equilibration of excitation energy in isolated photosystem II reaction centers. *Proceedings of the National Academy of Sciences*, Jan 1992.

[27] G. P. Wiederrecht, M. Seibert, Govindjee, and M. R. Wasielewski. Femtosecond photodichroism studies of isolated photosystem-II reaction centers. *Proceedings of the National Academy of Sciences*, 91(19):8999–9003, 1994.

[28] F. Vacha, D. M. Joseph, J. R. Durrant, A. Telfer, D. R. Klug, G. Porter, and J. Barber. Photochemistry and spectroscopy of a five-chlorophyll reaction-center of photosystem-II isolated by using a Cu affinity column. *Proceedings of the National Academy of Sciences*, 92(7):2929–2933, 1995.

[29] M. Müller, M. Hucke, M. Reus, and A. R Holzwarth. Primary processes and structure of the photosystem II reaction center. 4. low-intensity femtosecond transient absorption spectra of D1-D2-cyt-b559 reaction centers. *Journal of Physical Chemistry*, Jan 1996.

[30] D. R. Klug, T. Rech, D. M. Joseph, and J. Barber. Primary processes in isolated photosystem II reaction centres probed by magic angle transient absorption spectroscopy. *Chemical Physics*, Jan 1995.

[31] B. Donovan, L. A. Walker II, C. F. Yocum, and R. J Sension. Transient absorption studies of the primary charge separation in photosystem II. *Journal of Physical Chemistry*, 1996.

[32] S. R. Greenfield, M. Seibert, Govindjee, and M. R. Wasielewski. Wavelength and intensity dependent primary photochemistry of isolated photosystem II reaction centers at 5 degrees C. *Chemical Physics*, 210(1-2):279–295, 1996.

[33] A. R. Holzwarth, M. G. Müller, G. Gatzen, M. Hucke, and K. Griebenow. Ultrafast spectroscopy of the primary electron and energy-transfer processes in the reaction-center of photosystem-II. *Journal of Luminescence*, 60-1:497–502, Apr 1994.

[34] S. R. Greenfield, M. Seibert, and M. R. Wasielewski. Time-resolved absorption changes of the pheophytin Q_x band in isolated photosystem II reaction centers at 7 K: energy transfer and charge separation. *Journal of Physical Chemistry B*, 103(39):8364–8374, 1999.

[35] N. P. Pawlowicz, M. L. Groot, I. H. M. van Stokkum, J. Breton, and R. van Grondelle. Charge separation and energy transfer in the photosystem II core complex studied by femtosecond midinfrared spectroscopy. *Biophysical Journal*, 93(8):2732–2742, 2007.

[36] M. L. Groot, F. van Mourik, C. Eijckelhoff, I. H. M. van Stokkum, J. P. Dekker, and R. van Grondelle. Charge separation in the reaction center of photosystem II studied as a function of temperature. *Proceedings of the National Academy of Sciences*, Jan 1997.

[37] M. L. Groot, N. P. Pawlowicz, L. J. G. W. van Wilderen, J. Breton, I. H. M. van Stokkum, and R. van Grondelle. Initial electron donor and acceptor in isolated photosystem II reaction centers identified with femtosecond mid-IR spectroscopy. *Proceedings of the National Academy of Sciences*, Jan 2005.

[38] S. A. P. Merry, S. Kumazaki, Y. Tachibana, D. M. Joseph, G. Porter, K. Yoshihara, J. Barber, J. R. Durrant, and D. R. Klug. Sub-picosecond equilibration of excitation energy in isolated photosystem II reaction centers revisited: Time-dependent anisotropy. *Journal of Physical Chemistry*, 100(24):10469–10478, 1996.

[39] E. Romero, I. H. M. van Stokkum, V. I. Novoderezhkin, J. P. Dekker, and R. van Grondelle. Two different charge separation pathways in photosystem II. *Biochemistry*, 49(20):4300–4307, 2010.

[40] A. R. Holzwarth, M. Müller, and M. Reus. Kinetics and mechanism of electron transfer in intact photosystem II and in the isolated reaction center: pheophytin is the primary electron acceptor. *Proceedings of the National Academy of Sciences*, Jan 2006.

[41] F. van Mourik, M. L. Groot, R. van Grondelle, J. P. Dekker, and I. V. H. van Stokkum. Global and target analysis of fluorescence measurements on photosystem 2 reaction centers upon red excitation. *Physical Chemistry Chemical Physics*, 6(20):4820–4824, 2004.

[42] A. Freiberg, K. Timpmann, A. A. Moskalenko, and N. Y. Kuznetsova. Picosecond and nanosecond fluorescence kinetics of photosystem-II reaction-center and

its complex with CP47 antenna. *Biochimica et Biophysica Acta-Bioenergetics*, 1184(1):45–53, Feb 8 1994.

[43] T. A. Roelofs, M. Gilbert, V. A. Shuvalov, and A. R. Holzwarth. Picosecond fluorescence kinetics of the D1-D2-cyt-b-559 photosystem-II reaction center complex - energy-transfer and primary charge separation processes. *Biochimica et Biophysica Acta*, 1060(3):237–244, Nov 7 1991.

[44] L. Konermann, I. Yruela, and A. R. Holzwarth. Pigment assignment in the absorption spectrum of the photosystem II reaction center by site-selection fluorescence spectroscopy. *Biochemistry*, 36(24):7498–7502, Jun 1997.

[45] G. Gatzen, M. G. Müller, K. Griebenow, and A. R. Holzwarth. Primary processes and structure of the photosystem II reaction center. 3. kinetic analysis of picosecond energy transfer and charge separation processes in the D1-D2-cyt-b559 complex measured by time-resolved fluorescence. *Journal of Physical Chemistry*, 100(17):7269–7278, Apr 1996.

[46] T. A. Roelofs, S. L. S. Kwa, R. van Grondelle, J. P. Dekker, and A. R. Holzwarth. Primary processes and structure of the photosystem II reaction-center. 2. low-tempterature picosecond fluorescence kinetics of a D1-D2-cyt-b-559 reaction-center complex isolated by short triton exposure. *Biochimica et Biophysica Acta*, 1143(2):147–157, Jul 5 1993.

[47] B. Donovan, L. A. Walker, D. Kaplan, M. Bouvier, C. F. Yocum, and R. J. Sension. Structure and function in the isolated reaction center complex of photosystem II. 1. ultrafast fluorescence measurements of PSII. *Journal of Physical Chemistry B*, 101(26):5232–5238, Jun 26 1997.

[48] D. Tang, R. Jankowiak, M. Seibert, C. F. Yocum, and G. J. Small. Excited-state structure and energy-transfer dynamics of 2 different preparations of the reaction center of photosystem-II - a hole-burning study. *Journal of Physical Chemistry*, 94(17):6519–6522, Aug 1990.

[49] R. Jankowiak, D. Tang, G. J. Small, and M. Seibert. Transient and persistent hole burning of the reaction center of photosystem-II. *Journal of Physical Chemistry*, 93(4):1649–1654, Feb 23 1989.

[50] D. M. Tang, R. Jankowiak, M. Seibert, and G. J. Small. Effects of detergent on the excited-state structure and relaxation dynamics of the photosystem-II reaction center - a high-resolution hole burning study. *Photosynthesis Research*, 27(1):19–29, 1991.

[51] K. Riley, R. Jankowiak, M. Rätsep, G. J. Small, and V. Zazubovich. Evidence for highly dispersive primary charge separation kinetics and gross heterogeneity in the isolated PS II reaction center of green plants. *Journal of Physical Chemistry B*, 2004.

[52] R. Jankowiak, M. Rätsep, R. Picorel, M. Seibert, and G. J. Small. Excited states of the 5-chlorophyll photosystem II reaction center. *Journal of Physical Chemistry B*, 103(44):9759–9769, November 1999.

[53] V. Zazubovich, R. Jankowiak, K. Riley, R. Picorel, M. Seibert, and G. J. Small. How fast is excitation energy transfer in the photosystem II reaction center in the low temperature limit? hole burning vs photon echo. *Journal of Physical Chemistry B*, 107(12):2862–2866, 2003.

[54] R. Jankowiak, M. Rätsep, J. Hayes, V. Zazubovich, R. Picorel, M. Seibert, and G. J. Small. Primary charge-separation rate at 5 K in isolated photosystem II reaction centers containing five and six chlorophyll *a* molecules. *Journal of Physical Chemistry B*, 107(9):2068–2074, 2003.

[55] K. J. Vink, S. Deboer, J. J. Plijter, A. J. Hoff, and D. A. Wiersma. Optical-dynamics of the reaction center of photosystem-II - a hole-burning and photon-echo study. *Chemical Physics Letters*, 142(6):433–438, 1987.

[56] V. Prokhorenko and A. R. Holzwarth. Primary processes and structure of the photosystem II reaction center: A photon echo study. *Journal of Physical Chemistry B*, Jan 2000.

[57] R. J. W. Louwe and T. J. Aartsma. Excited state dynamics in photosynthetic antenna complexes studied with accumulated photon echoes. *Photosynthesis: From Light To Biosphere, Vol I*, pages 363–366, 1995.

[58] J. A. Myers, K. L. M. Lewis, F. Fuller, P. Tekavec, and J. P. Ogilvie. Two-dimensional electronic spectroscopy of the D1-D2-cyt b559 photosystem II reaction center complex. *Physical Chemistry Letters*, 2010.

[59] E. Krausz, J. Hughes, P. Smith, R. Pace, and S. P. Årsköld. Oxygen-evolving photosystem II core complexes: a new paradigm based on the spectral identification of the charge-separating state, the primary acceptor and assignment of low-temperature fluorescence. *Photochemical & Photobiological Sciences*, Jan 2005.

[60] E. Krausz, N. Cox, and S. Årsköld. Spectral characteristics of PS II reaction centres: as isolated preparations and when integral to PS II core complexes. *Photosynthesis Research*, Jan 2008.

[61] L. Yoder, A. Cole, and R. J. Sension. Structure and function in the isolated reaction center complex of photosystem II: energy and charge transfer dynamics and mechanism. *Photosynthesis Research*, Jan 2002.

[62] B. A. Diner, E. Schlodder, P. J. Nixon, W. J. Coleman, F. Rappaport, J. Lavergne, W. F. J. Vermaas, and D. A. Chisholm. Site-directed mutations at D1-His198 and D2-His197 of photosystem II in *Synechocystis* PCC 6803: sites of primary charge separation and cation and triplet stabilization. *Biochemistry*, Jan 2001.

[63] G. Raszewski, W. Saenger, and T. Renger. Theory of optical spectra of photosystem II reaction centers: location of the triplet state and the identity of the primary electron donor. *Biophysical Journal*, Jan 2005.

[64] L. Barter, J. R. Durrant, and D. R. Klug. A quantitative structure-function relationship for the photosystem II reaction center: Supermolecular behavior in natural photosynthesis. *Proceedings of the National Academy of Sciences*, Jan 2003.

[65] V. I. Novoderezhkin, E. Romero, J. P. Dekker, and R. Grondelle. Multiple charge-separation pathways in photosystem II: Modeling of transient absorption kinetics. *ChemPhysChem*, 12(3):681–688, Feb 2011.

[66] S. R. Greenfield and M. R. Wasielewski. Excitation energy transfer and charge separation in the isolated photosystem II reaction center. *Photosynthesis Research*, 48(1):83–97, 1996.

[67] H. M. Visser, M. L. Groot, F. van Mourik, I. H. M. van Stokkum, J. P. Dekker, and R. van Grondelle. Subpicosecond transient absorption difference spectroscopy on the reaction center of photosystem II: radical pair formation at 77 K. *The Journal of Physical Chemistry*, Jan 1995.

[68] S. R. Greenfield, M. Seibert, Govindjee, and M. R. Wasielewski. Direct measurement of the effective rate constant for primary charge separation in isolated photosystem II reaction centers. *Journal of Physical Chemistry B*, 101(13):2251–2255, March 1997.

[69] S. Kumazaki, D. M. Joseph, B. Crystall, Y. Tachibana, J. R. Durrant, J. Barber, G. Porter, K. Yoshihara, and D. R. Klug. Experimental observation of multiple trapping charge separation steps in the isolated PS2 reaction centre. *Photosynthesis: From Light To Biosphere, Vol I*, pages 883–886, 1995.

[70] J. Shiang, L. Yoder, and R. J. Sension. Structure and function in the isolated reaction-center complex of photosystem II. 2. models for energy relaxation and charge separation in a protein matrix. *Journal of Physical Chemistry B*, Jan 2003.

[71] M. Seibert and M. R. Wasielewski. The isolated photosystem II reaction center: first attempts to directly measure the kinetics of primary charge separation. *Photosynthesis Research*, 76(1):263–268, 2003.

[72] M Muller, M Hucke, M Reus, and Alfred R Holzwarth. Annihilation processes in the isolated D1-D2-cyt-b559 reaction center complex of photosystem II. an intensity-dependence study of femtosecond transient absorption. *Journal of Physical Chemistry*, Jan 1996.

[73] J. R. Durrant, D. R. Klug, S. Kwa, R. van Grondelle, G. Porter, and J. P. Dekker. A multimer model for P680, the primary electron donor of photosystem II. *Proceedings of the National Academy of Sciences*, Jan 1995.

[74] A. Zouni, H. Witt, J. Kern, P. Fromme, and N. Krauss. Crystal structure of photosystem II from *Synechococcus elongatus* at 3.8 Å resolution. *Nature*, Jan 2001.

[75] U. Ermler, G. Fritzsch, S. K. Buchanan, and H. Michel. Structure of the photosynthetic reaction centre from *Rhodobacter sphaeroides* at 2.65 Å resolution: cofactors and protein-cofactor interactions. *Structure*, 2(10):925–936, 1994.

[76] J. Leegwater, J. R. Durrant, and D. R. Klug. Exciton equilibration induced by phonons: theory and application to PS II reaction centers. *Journal of Physical Chemistry B*, Jan 1997.

[77] T. Renger and R. A. Marcus. Photophysical properties of PS-2 reaction centers and a discrepancy in exciton relaxation times. *Journal of Physical Chemistry B*, 106(7):1809–1819, Jan 2002.

[78] R. Jankowiak, J. Hayes, and G. J. Small. An excitonic pentamer model for the core Q_y states of the isolated photosystem II reaction center. *Journal of Physical Chemistry B*, Jan 2002.

[79] N Ivashin and S Larsson. Excitonic states in photosystem II reaction center. *Journal of Physical Chemistry B*, 109(48):23051–23060, 2005.

[80] G. Raszewski, B. A. Diner, E. Schlodder, and T. Renger. Spectroscopic properties of reaction center pigments in photosystem II core complexes: revision of the multimer model. *Biophysical Journal*, 95(1):105–119, 2008.

[81] K. N. Ferreira, T. M. Iverson, K. Maghlaoui, J. Barber, and S. Iwata. Architecture of the photosynthetic oxygen-evolving center. *Science*, 303(5665):1831–1838, Mar 2004.

[82] B. Loll, J. Kern, W. Saenger, A. Zouni, and J. Biesiadka. Towards complete cofactor arrangement in the 3.0 Å resolution structure of photosystem II. *Nature*, Jan 2005.

[83] V. I. Novoderezhkin, E. G. Andrizhiyevskaya, J. P. Dekker, and R. van Grondelle. Pathways and timescales of primary charge separation in the photosystem II reaction center as revealed by a simultaneous fit of time-resolved fluorescence and transient absorption. *Biophysical Journal*, 89(3):1464–1481, 2005.

[84] V. I. Novoderezhkin, J. P. Dekker, and R. van Grondelle. Mixing of exciton and charge-transfer states in photosystem II reaction centers: modeling of Stark spectra with modified Redfield theory. *Biophysical Journal*, 93(4):1293–1311, 2007.

[85] R. N. Frese, M. Germano, F. L. de Weerd, I. H. M. van Stokkum, A. Y. Shkuropatov, V. A. Shuvalov, H. J. van Gorkom, R. van Grondelle, and J. P. Dekker. Electric field effects on the chlorophylls, pheophytins, and β-carotenes in the reaction center of photosystem II. *Biochemistry*, 42, 2003.

[86] W. Zhang, T. Meier, V. Chernyak, and S. Mukamel. Exciton-migration and three-pulse femtosecond optical spectroscopies of photosynthetic antenna complexes. *Journal of Chemical Physics*, Jan 1998.

[87] M. Yang and G. R. Fleming. Influence of phonons on exciton transfer dynamics: comparison of the Redfield, Förster, and modified Redfield equations. *Chemical Physics*, 275(1-3):355–372, 2002.

[88] D. Abramavicius and S. Mukamel. Energy-transfer and charge-separation pathways in the reaction center of photosystem II revealed by coherent two-dimensional optical spectroscopy. *Journal of Chemical Physics*, Jan 2010.

CHAPTER II

Two Dimensional Electronic Spectroscopy

In this chapter I describe the fundamentals of two dimensional electronic spectroscopy (2DES). I motivate the use of 2DES with a brief discussion of the limitations of linear spectroscopy for studying complex condensed phase systems such as the photosystem II reaction center. The basics of the formalisms used in nonlinear spectroscopy are discussed, but for a full treatment, one should reference *Principles of Nonlinear Spectroscopy* by Shaul Mukamel [1].

I then turn more specifically to third-order spectroscopies, and how double-sided Feynman diagrams can be used to graphically represent the pathways that contribute to phase-matched signals detected in different third-order experiments. Finally, I look at example 2D spectra in a number of different cases to demonstrate how 2D spectroscopy can resolve inhomogeneous and homogeneous broadening, as well as provide detailed information about coupling between states. For a thorough treatment, consult these review articles [2–4] and texts [5, 6] on two dimensional optical spectroscopy.

2.1 Linear limitations

When considering a new material system, linear absorption is generally the first optical property measured. A relatively simple measurement, linear absorption reveals

how much light of any given frequency is absorbed by the system. This reveals the energy and strength of the system's optical transitions.

While linear spectroscopy is useful as a first look at the ground to excited transition, fundamentally different systems can yield similar linear spectra. For instance, a broad absorption peak could equally well indicate a system with a large homogeneous linewidth, or an inhomogenously broadened system. The homogeneous linewidth is the natural width of a single optical transition with a finite lifetime. This width is roughly given as $\delta\omega \sim 1/T_{\text{lifetime}}$ and the lineshape is Lorentzian due to the exponential decay of the dipole moment [7].

Inhomogeneous broadening, however, is caused by different physical mechanisms. In the gaseous phase, inhomogeneous broadening is often due to a distribution in the velocities of the molecules causing shifts in the absorption frequency of any given molecule (Doppler broadening) [7]. In the condensed phase, the focus of this thesis, each individual chromophore (system) faces a slightly different local environment (bath). The interaction of the system with the bath shifts the absorption of the system. In the particular case of photosystem II, the absorption can be highly affected by the configuration of the surrounding protein scaffold, and each complex will be in slightly different configurations, resulting in inhomogeneously broadened spectra.

One particularly good example of inhomogeneous broadening can be seen in the single-molecule fluorescence studies of LHII, a light harvesting antenna complex found in purple bacteria [8]. This protein consists of two concentric rings of chlorophylls, called B800 and B850. In this study, the authors show an ensemble measurement of the fluorescence excitation spectrum, revealing two broad peaks, one from each ring. When looking at the fluorescence excitation spectra of a single complexes, however, the two rings exhibit fundamentally different behavior; while the B850 band was still rather broad, the B800 band displayed many sharp, narrow peaks. In light-harvesting systems in general, the combination of disorder and electronic coupling

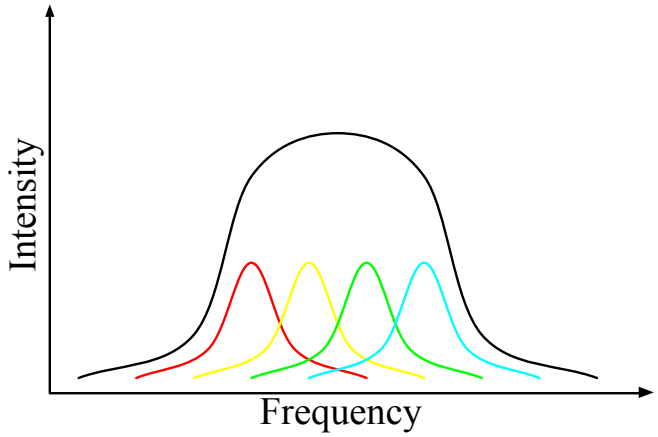

Figure 2.1: An example of four closely-spaced optical transitions with Lorentzian lineshapes, and the sum of these transitions, showing an overall inhomogeneously broadened lineshape.

between pigments makes understanding the broadening mechanisms a difficult task that requires measurements beyond linear spectra [9].

In addition, linear spectroscopy does not reveal information about many different properties of systems with chromophores. For example, a system with two uncoupled chromophores can have a similar spectrum to one with two strongly coupled chromophores. Linear spectroscopy is a static measurement, unable to follow dynamical processes such as energy and charge transfer. In order to look at the time evolution of a system and to differentiate between systems that yield similar spectra, we must move to higher-order spectroscopies.

2.2 Polarization to the response function

In this section, all equations and notation follow that of Shaul Mukamel's book, primarily chapters 3 and 5 [1]. This work will be done within the Liouville space instead of the Hilbert space. Where the Hilbert space uses wavefunctions and Hamiltonians, the Liouville space uses the density matrix and the Liouville operator, such that $\mathscr{L}A = [H, A]$, where H is the Hamiltonian.

The Liouville space is a good way to connect theory and experiment. It simultaneously keeps track of interactions with the bra and the ket in a fully time-ordered manner. These well-defined time orderings provide an intuitive picture of the experiments, where each pathway is distinct and can be visualized through the use of double-sided Feynman diagrams (to be discussed in section 2.3.1).

2.2.1 Density matrices

The density matrix of the system, $\rho(t)$, is a convenient way of describing the state of the system at any given time. If a quantum system can be solely defined by a wavefunction $|\psi(t)\rangle$, then $\rho(t) = |\psi(t)\rangle \langle\psi(t)|$. This is known as a pure state. However, ensembles of quantum systems often exist in mixed states, which are incompletely defined through a wavefunction. In this case, $\rho(t) = \sum_k P_k |\psi_k(t)\rangle \langle\psi_k(t)|$, where P_k represents the probability of being in a state k. When interpreting the meaning of the density matrix, we take the diagonal elements of the matrix to be populations, while the off-diagonal elements represent coherences between states. Figure 2.2 gives an example of the behavior of the density matrix in the context of a four-wave mixing experiment.

The density operator (matrix) can be used to calculate the expectation values for any given operator A : $\langle A\rangle = \mathrm{Tr}[A\rho(t)]$, and its time evolution follows the Liouville equation:

$$\dot{\rho} = -\frac{i}{\hbar}[H, \rho] \tag{2.1}$$

2.2.2 Polarization

When using spectroscopy to study the properties of a system, we do so by measuring the polarization generated after an interaction with one or more electric fields. To conveniently discuss the responses with differing numbers of field interactions, we

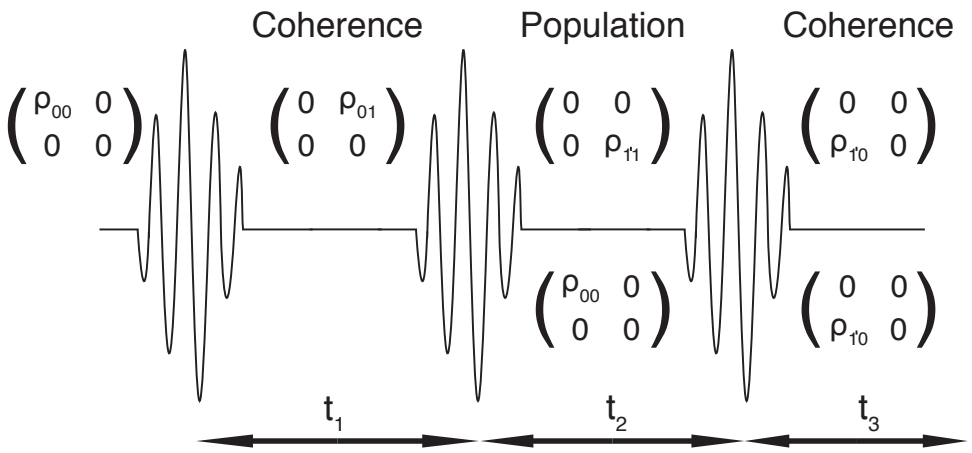

Figure 2.2: A diagram showing the density matrix within the framework of three field interactions for two rephasing pathways. Figure used with permission from [10] and adapted from [4].

expand the polarization:

$$P = P^{(1)} + P^{(2)} + P^{(3)} + \dots \tag{2.2}$$

With a single field interaction, we generate the linear response, characterized by $P^{(1)}$, and we can study eigenstate energies and strengths. Properties such as reflection and refraction are also related to $P^{(1)}$. With an increasing number of field interactions, we access a wider range of material properties, at the expense of weaker signals and more complicated experimental setups. The second-order response, $P^{(2)}$, is taken advantage of in birefringent materials for second harmonic generation. Second-order effects are also useful for studying interfaces. For isotropic media, $P^{(2)}$ and indeed, all even-order responses, are zero [11].

For a general system, then, the next-lowest order is the third-order response, $P^{(3)}$. Third-order techniques involve three field interactions, and are generally referred to as four-wave mixing techniques; higher order responses are N+1 wave mixing techniques, where N is the number of external field interactions, (the N+1$^{\text{th}}$ field comes from the

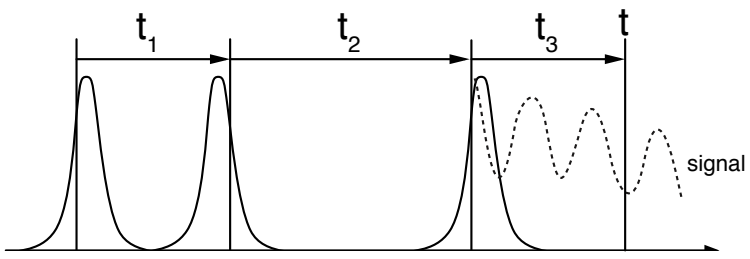

Figure 2.3: A diagram showing the timing of the field interactions. Note that the field interactions do not necessarily take place at the peak of the incident pulse.

signal emitted by the sample.)

The third-order polarization is a convolution of the system response $S^{(3)}$ with the incident electric fields, where the time variables are shown in Figure 2.3:

$$P^{(3)}(\mathbf{r},t) = \int_0^\infty dt_3 \int_0^\infty dt_2 \int_0^\infty dt_1 S^{(3)}(t_3,t_2,t_1) E(\mathbf{r},t-t_3) E(\mathbf{r},t-t_3-t_2) E(\mathbf{r},t-t_3-t_2-t_1) \tag{2.3}$$

Here the system response, $S^{(3)}(t_3,t_2,t_1)$, is the expectation value of the dipole operator, V on the state of the system after all field interactions and field-free evolution and is given by:

$$S^{(3)}(t_3,t_2,t_1) = \left(\frac{i}{\hbar}\right)^3 \langle\langle V| \mathscr{G}(t_3)\mathscr{V}\mathscr{G}(t_2)\mathscr{V}\mathscr{G}(t_1)\mathscr{V} |\rho(-\infty)\rangle\rangle \tag{2.4}$$

where $\mathscr{V}$ is the Liouville space operator representing an interaction with the electric field such that $\mathscr{V}A = [V,A]$. $\mathscr{G}(t)$ is the Green's function that describes field-free evolution of the system between field interactions. The initial (equilibrium) state of the system in Equation 2.4 is $\rho(-\infty)$. Here, we see the density operator in a slightly different form: the superoperator, denoted by $|\rho(t)\rangle\rangle$. This contains all the same information as the density matrix described above, but instead of a matrix, the superoperator is rearranged to form a vector, for ease of calculation.

2.2.3 Response functions

When we go back and look more closely at the system response, $S^{(3)}$ in Equation 2.4, we note that the three field interaction terms ($\mathscr{V}$) can be applied either to the right or the left, giving 8 possible orderings. These eight pathways can be reduced to four and their complex conjugates such that:

$$S^{(3)}(t_3,t_2,t_1) = \left(\frac{i}{\hbar}\right)^3 \theta(t_1)\theta(t_2)\theta(t_3)\sum_{\alpha=1}^{4}[R_\alpha(t_3,t_2,t_1) - R_\alpha^*(t_3,t_2,t_1)] \tag{2.5}$$

where $\theta(t)$ represents a Heaviside function, and we have the four response functions:

$$\begin{aligned}
R_1(t_3,t_2,t_1) &= \langle V(t_1)V(t_1+t_2)V(t_1+t_2+t_3)V(0)\rho(-\infty)\rangle \\
R_2(t_3,t_2,t_1) &= \langle V(0)V(t_1+t_2)V(t_1+t_2+t_3)V(t_1)\rho(-\infty)\rangle \\
R_3(t_3,t_2,t_1) &= \langle V(0)V(t_1)V(t_1+t_2+t_3)V(t_1+t_2)\rho(-\infty)\rangle \\
R_4(t_3,t_2,t_1) &= \langle V(t_1+t_2+t_3)V(t_1+t_2)V(t_1)V(0)\rho(-\infty)\rangle
\end{aligned} \tag{2.6}$$

These four (eight with the complex conjugates) functions, represent the different ways a system can interact with a field three times, by either promoting or de-exciting either the bra or ket side of the density matrix. Whether the field acts on the bra or the ket is chosen by whether the operator acted from the right or the left in the above response functions. A graphical way of representing these signals important for 2DES is presented in the following section.

2.3 Phase matching

Two dimensional optical spectroscopy has its roots in 2D-NMR. One of the key differences between 2D-NMR and 2DES is the directionality of the signal. The radio waves involved in NMR have a much longer wavelength than the sample size, meaning that $kr \ll 1$. This leads to the signal being emitted isotropically. However,

in optical frequencies, $\lambda \ll$ sample size, which leads to a highly directional signal. Two dimensional electronic spectroscopy can take advantage of this directionality to spatially separate different third order signals through phase-matching [12].

2.3.1 Double-sided Feynman diagrams

In order to gain a more intuitive understanding of the third-order response, it is helpful to have a graphical representation of the many ways the third-order signal can be generated after three field interactions. These are often described by double-sided Feynman diagrams, or ladder diagrams [2, 3]. The vertical line on the left (right) of the diagram represents an interaction with the ket (bra) of the density matrix. Moving upwards along the ladder represents increasing time; Each field interaction is designated by a rung on the ladder, and the sign of the wave-vector is given by the direction of the arrow. Right-pointing arrows have an interaction of the form $\varepsilon_j(t)\exp(i\mathbf{k}_j \cdot \mathbf{r} - i\omega_j t)$ and contribute a positive wavevector to the signal, while left-pointing arrows are of the form $\varepsilon_j(t)\exp(-i\mathbf{k}_j \cdot \mathbf{r} + i\omega_j t)$ and contribute a negative wavevector to the signal. Arrows pointing towards the center of the diagram excite the bra or ket to a higher energy level, while arrows pointing away from the center lower the energy level of the bra or the ket. Figure 2.4 shows an example double-sided Feynman diagram.

2.3.2 Types of signals

Since third-order signals are highly directional, we often use the phase-matching direction to spatially separate and categorize the signals emitted. Each phase-matching direction will have contributions from multiple signal pathways represented by different ladder diagrams, it is helpful to classify them in this way since we can choose to collect them independently in the lab. In this section, consider the system shown in Figure 2.5. The system contains two singly-excited electronic states that share a

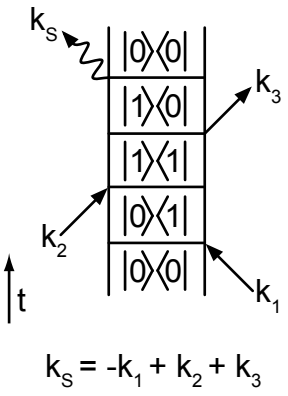

Figure 2.4: An example of a double-sided Feynman diagram, in this case for a stimulated emission process. Note that the symbols for the bra and ket are often removed, and only the state designation remains.

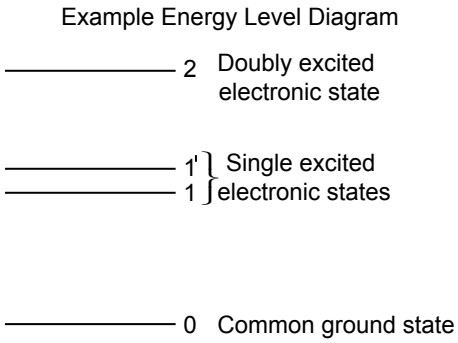

Figure 2.5: The system considered for all the Feynman diagrams shown in this section. Vibrational levels are ignored.

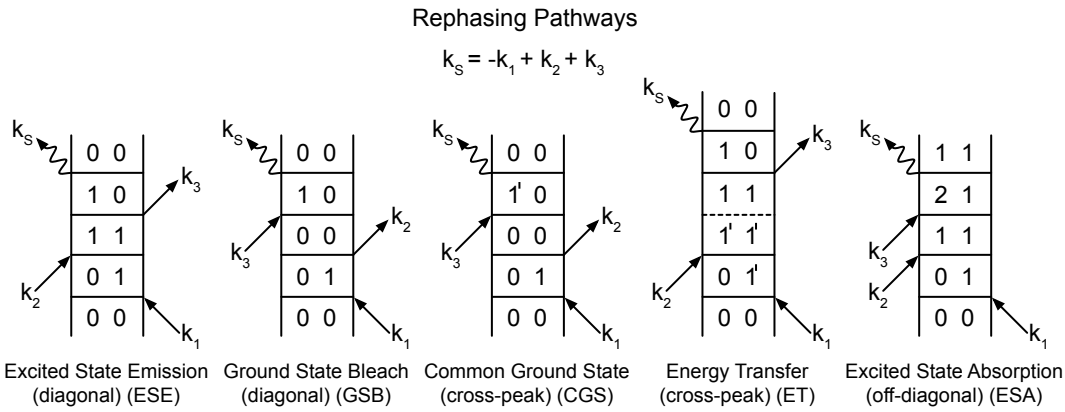

Figure 2.6: Rephasing diagrams. Note that I have dropped the bra and ket symbols.

common ground state, and a single doubly excited state. Such an electronic structure could arise from the coupling of two identical two-level systems.

Rephasing

The rephasing signal is also called the photon echo signal, and is comparable to the spin echo phenomena [3]. During t_1, the coherence created after the initial excitation dephases. During t_2, the system is in a population so there is no further dephasing, and during t_3, the coherence evolves in the opposite direction as it did during t_1, allowing the signal to "rephase" and emit a signal.

The rephasing signal is emitted in the $\mathbf{k}_S = \mathbf{k}_2 - \mathbf{k}_1 + \mathbf{k}_3$ direction. Multiple pathways (shown in Figure 2.6) contribute to this phase matching direction. I have neglected vibrational states for simplicity, but note that state 1' could also represent an excited vibrational level of the first state. If, during t_2, the system is not in a pure population, but rather a coherence between two-different states (vibrational or electronic) the peak associated with that pathway will be modulated by the difference frequency of the levels, as has been observed by our group [13] and others [14] for the vibrational case and a number of groups in the electronic case [15–17].

When using the response function formalism described in Section 2.2, the rephasing signals constitute $R_2 + R_3$.

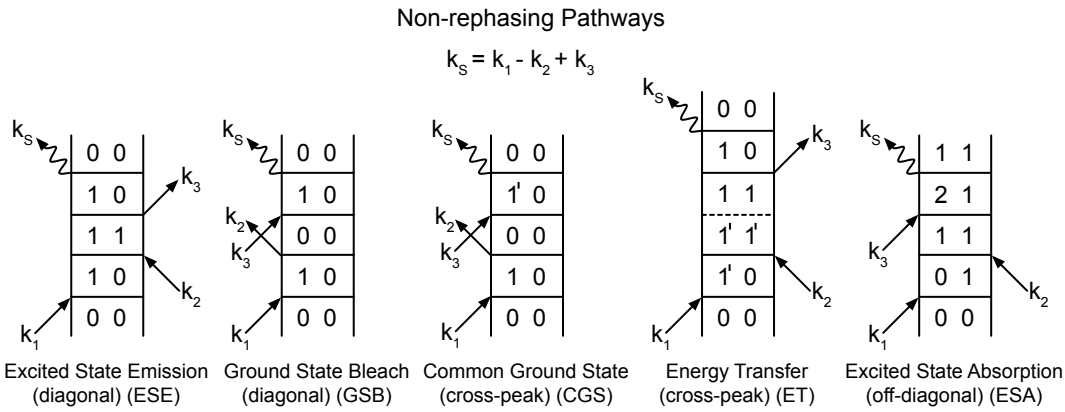

Figure 2.7: Non-rephasing diagrams.

Non-rephasing

In the non-rephasing signal (or virtual echo), the coherences during t_1 and t_3 evolve in the same direction, so the signal does not rephase. Alternately, the signal could be considered to have rephased at $t_3 = -t_1$, leading to the term virtual echo.

The non-rephasing signal is emitted in the $\mathbf{k}_S = \mathbf{k}_2 - \mathbf{k}_1 + \mathbf{k}_3$ direction. Again, multiple pathways can contribute to this phase-matching condition, and they are shown in Figure 2.7. When using the response function formalism described in Section 2.2, the rephasing signals constitute $R_1 + R_4$.

Double-quantum coherence

While not the focus of this thesis, two dimensional double-quantum coherence spectroscopy (2D-DQCS) is a related third-order technique. In 2D-DQCS, a coherence is created between a doubly excited state and the ground state during t_2 instead of a population. Therefore, the signal only lasts for values of t_2 on the order of the double-quantum coherence time. The spectra reported in 2D-DQCS are then plotted as the Fourier transform of a t_2 scan (ω_2), and the detection frequency, ω_3, to correlate these two coherences [18]. The phase matching direction for two-quantum coherences is $\mathbf{k}_S = \mathbf{k}_1 + \mathbf{k}_2 - \mathbf{k}_3$. Example pathways can be seen in Figure 2.8.

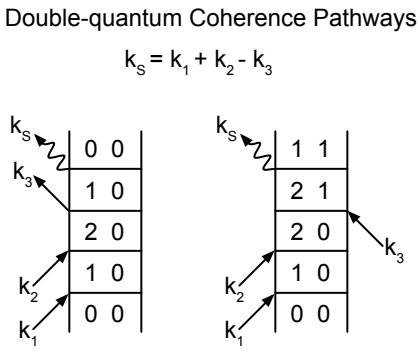

Figure 2.8: Double-quantum coherence diagrams.

2.4 Putting it all together to create 2D spectra

2.4.1 Phase twist and absorptive spectra

Now it is time to see how all of these signal pathways combine and appear in two-dimensional electronic spectroscopy. Since the rephasing and non-rephasing spectra have different phase-matching conditions, they can be measured independently with an appropriate spatial configuration of input fields. However, each of these spectra alone are plagued by phase twist, a term originally used in NMR [19] meaning that absorptive and dispersive components are mixed. Phase-twisted lineshapes are artificially broad and are distorted [20].

Therefore, in order to obtain the narrowest lineshapes, it is preferable to combine the rephasing and nonrephasing spectra. When equally weighted, the sum of the rephasing and nonrephasing signals yield a lineshape free of phase twist [20]. The real part of the spectrum is the absorptive signal, while the imaginary portion of the signal is the dispersive response. Throughout the rest of this thesis, I will primarily discuss absorptive spectra unless otherwise specified.

2.4.2 How a 2D spectrum is created

A two-dimensional spectrum is created using a sequence of three short laser pulses as depicted in Figure 2.3. The first excites a coherence between the ground state and an excited state. After a time t_1, a second field interaction creates a population, either on the ground state or the excited state.[1] The third pulse (probe) again creates a coherence after waiting for a t_2 delay, after which the system emits the detected signal a time t_3 later. The system is in a population during the t_2, called the waiting time. Since populations have much longer lifetimes than coherences, a wide variety of waiting times can be studied: from femtoseconds to hundreds of picoseconds or longer if your experimental design allows for it. It is within this time period that we monitor the processes of energy and charge transfer in the photosystem II reaction center.

The two axes in the spectrum are created through Fourier transforms of the t_1 and t_3 delays: ω_1 and ω_3, respectively. The t_1 delay is scanned experimentally, often using either a refractive delay [21–23] or a programmable delay as in a pulse shaper [24, 25]. Typically, the t_3 delay is not directly detected; instead a spectrometer performs the Fourier transform measuring the signal as a function of ω_3.

2.4.3 Double spectra: What does it mean?

A 2D spectrum can be viewed as a correlation map: if we excite the system at a frequency ω_1, at what frequency does the system emit or absorb after waiting time t_2? A cartoon of absorptive 2D spectra for three different cases is shown in Figure 2.9. This demonstrates the information content of 2DES, and reveals the power of expanding linear spectroscopy to another dimension.

Figure 2.9a shows an example of a simple system: two uncoupled chromophores.

[1] In systems with more than one excited state, the second interaction may also generate an intra-band coherence in the first excited state manifold.

There will be two peaks along the diagonal at the respective frequencies of the chromophores. For early values of t_2, the peaks will be elongated along the diagonal, and will consist of the excited state emission and ground state bleach pathways. The diagonal width shows the inhomogeneous broadening of each chromophore, and the anti-diagonal width reveals the homogeneous linewidth at $t_2 = 0$. At longer values of t_2, spectral diffusion will cause the peaks to round out, such that both the diagonal and anti-diagonal widths will approach the inhomogeneous linewidth.

Figure 2.9b shows two weakly coupled three-level chromophores that exhibit energy transfer. Again, we have the two diagonal peaks with contributions from excited state emission (ESE) and ground state bleach (GSB). This time, however, we include the excited state absorption (ESA) pathway as well. Often, the transition energy from the first excited state to the second excited state is of similar energy, but somewhat blue-shifted. Therefore, ESA peaks will be slightly below the diagonal peaks. As mentioned before, the ESA peaks will be negative compared to the ESE and GSB peaks. Therefore, lineshape analysis of these peaks can be complicated by overlapping and canceling contributions. Also in this cartoon, we demonstrate the appearance of an energy transfer cross-peak. At $t_2 = 0$, this peak will not exist because the coupling between the chromophores is weak. This peak will grow in as a function of t_2; the growth of the peak reveals the rate of energy transfer. In 2DES, this peak is usually only below the diagonal; thermal energy is small enough to prevent energy transfer uphill in electronic systems.

Figure 2.9c shows the 2D spectrum in the strong coupling case where an excitonic picture is appropriate. In this case, we see an energy splitting of the levels, and the new excitonic states will share a ground state. The 2D spectrum shows the diagonal peaks for the new, shifted levels, as well as cross-peaks both above and below the diagonal. The cross-peaks arise from the common ground state pathway, and unlike the cross-peak in panel b, will not have a t_2 dependence.

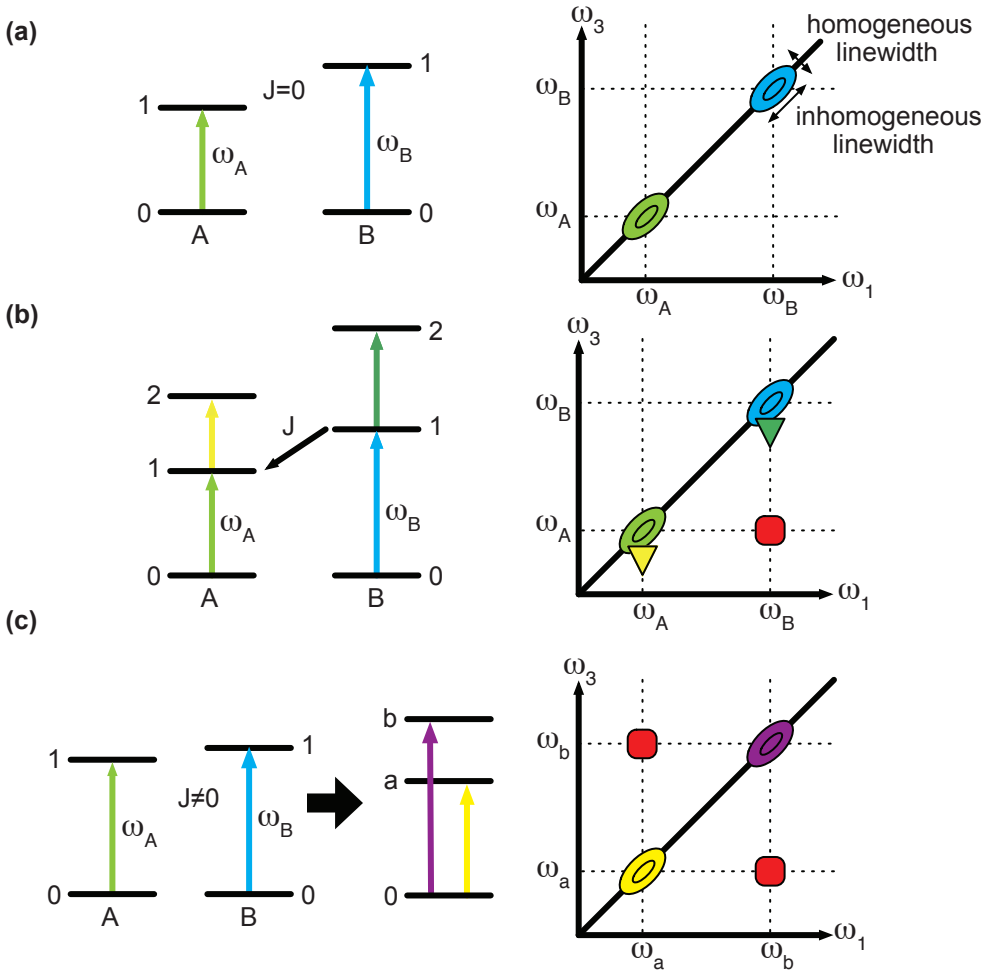

Figure 2.9: Cartoon depictions of absorptive 2D spectra for three cases. **a)** Two uncoupled two-level systems showing only diagonal peaks. **b)** Two weakly coupled three-level systems. The spectra exhibits a cross peak from energy transfer, as well as excited state absorption peaks. Note that ESA peaks are opposite in sign from the rest of the contributions. **c)** Two strongly coupled two-level systems, which can be described in an excitonic picture with a splitting of the energy levels. This spectrum exhibits common ground state peaks which appear both above and below the diagonal.

2.4.4 Transient absorption in relation to 2DES

Two-dimensional electronic spectroscopy has the ability to resolve cross-peaks, a feature that is lost in transient absorption spectroscopy. In fact, transient absorption measurements are a subset of 2D spectroscopy. The projection-slice theorem states that a transient absorption spectrum for a certain time delay τ is obtained by projecting the real part of a 2D spectrum at $t_2 = \tau$ onto the ω_3 axis [12]. With broadband pulses for ultrafast time resolution, this would involve integrating along the excitation axis, and the cross-peak would be obscured by the generally larger diagonal peak [22].

Transient absorption spectroscopy, or pump-probe spectroscopy, was one of the first nonlinear spectroscopic techniques. In this technique, a strong pump pulse interacts with the sample twice, and after a delay, a weaker probe pulse measures the change in absorption due to the presence of the pump beam. This is equivalent to combining the two pump pulses of 2DES into one pump pulse, collapsing the excitation axis. Transient absorption spectroscopy has led to many advances in the understanding of photosystem II [26–34], and is a powerful technique in its own right.

Transient absorption spectroscopy, however, is not the cure-all for revealing the all the questions left unresolved by linear spectroscopy. In ultrafast optics we must usually make a choice. The spectral bandwidth of a laser pulse is related to the minimum temporal width of that pulse through a Fourier transform; the larger the spectral bandwidth, the shorter a pulse can be. Given that you can only measure dynamics of a system longer than the pulses used in the experiment, transform-limited broadband pulses are optimal for measuring the ultrafast behavior of a system. Using broadband pulses, however, limits the spectral selectivity of the experiment. Broadband pulses can excite multiple transitions that are closely spaced (as in photosystem II), leading to difficulty in separating the energy pathways resulting from exciting one transition alone or another. In 2DES, however, we find a technique that allows for high spectral selectivity while simultaneously using temporally short, broadband pulses.

References

[1] S. Mukamel. *Principles of Nonlinear Optical Spectroscopy*. Oxford University Press, 1995.

[2] W. Zhuang, T. Hayashi, and S. Mukamel. Coherent multidimensional vibrational spectroscopy of biomolecules: concepts, simulations, and challenges. *Angewandte Chemie*, Jan 2009.

[3] M. Cho. Coherent two-dimensional optical spectroscopy. *Chemical Reviews*, Jan 2008.

[4] J. P. Ogilvie and K. Kubarych. Multidimensional electronic and vibrational spectroscopy: An ultrafast probe of molecular relaxation and reaction dynamics. *Advances In Atomic, Molecular, and Optical Physics*, 57, Jan 2009.

[5] M. Cho. *Two Dimensional Optical Spectroscopy*. CRC Press, 2009.

[6] P. Hamm and M. Zanni. *Concepts and Methods of 2D Infrared Spectroscopy*. Cambridge University Press, 2011.

[7] L. Allen and J. H. Eberly. *Optical Resonance and Two-Level Atoms*. Dover Publications, Inc., 1987.

[8] M. Ketelaars, A. M. van Oijen, M. Matsushita, J. Köhler, J. Schmidt, and T. J. Aartsma. Spectroscopy on the B850 band of individual light-harvesting 2 complexes of *Rhodopseudomonas acidophila* I. experiments and Monte Carlo simulations. *Biophysical Journal*, 80(3):1591–1603, 2001.

[9] H. van Amerongen, L. Valkunas, and R. van Grondelle. *Photosynthetic excitons*. World Scientific Publishing Co., 2000.

[10] J. A. Myers. *Two-dimensional electronic spectroscopy of the photosystem II D1D2-cyt.*b559 *reaction center complex*. PhD thesis, University of Michigan, 2010.

[11] R. W. Boyd. *Nonlinear Optics*. Academic Press, Boston, 2008.

[12] D. M. Jonas. Two-dimensional femtosecond spectroscopy. *Annual Review of Physical Chemistry*, 54(1):425–463, 2003.

[13] P. F. Tekavec, J. A. Myers, K. L. M. Lewis, and J. P. Ogilvie. Two-dimensional electronic spectroscopy with a continuum probe. *Optics Letters*, 34(9):1390–1392, 2009.

[14] A. Nemeth, F. Milota, T. Mančal, V. Lukeš, J. Hauer, H. F. Kauffmann, and J. Sperling. Vibrational wave packet induced oscillations in two-dimensional electronic spectra. I. experiments. *Journal of Chemical Physics*, 132(18):184514, Jan 2010.

[15] E. Collini and G. D. Scholes. Coherent intrachain energy migration in a conjugated polymer at room temperature. *Science*, 323(5912):369–373, Jan 2009.

[16] E. Collini, C. Y. Wong, K. E. Wilk, P. M. G. Curmi, P. Brumer, and G. D. Scholes. Coherently wired light-harvesting in photosynthetic marine algae at ambient temperature. *Nature*, 463(7281):644–647, Feb 2010.

[17] G. Engel, T. Calhoun, E. L. Read, and T. Ahn. Evidence for wavelike energy transfer through quantum coherence in photosynthetic systems. *Nature*, Jan 2007.

[18] J. Kim, S. Mukamel, and G. D. Scholes. Two-dimensional electronic double-quantum coherence spectroscopy. *Accounts of Chemical Research*, 2009.

[19] R. R. Ernst, G. Bodenhausen, and A. Wokaun. *Principles of Nuclear Magnetic Resonance in One and Two Dimensions*. Oxford University Press, Oxford, U.K., 1987.

[20] M. Khalil, N. Demirdoven, and A. Tokmakoff. Coherent 2D IR spectroscopy: molecular structure and dynamics in solution. *Journal of Physical Chemistry A*, 107(27):5258–5279, 2003.

[21] M. L. Cowan, J. P. Ogilvie, and R. J. D. Miller. Two-dimensional spectroscopy using diffractive optics based phased-locked photon echoes. *Chemical Physics Letters*, 2004.

[22] T. Brixner, T. Mančal, I. Stiopkin, and G. R. Fleming. Phase-stabilized two-dimensional electronic spectroscopy. *Journal of Chemical Physics*, Jan 2004. Brixner Phasing Paper.

[23] A. Nemeth, J. Sperling, J. Hauer, H. F. Kauffmann, and F. Milota. Compact phase-stable design for single-and double-quantum two-dimensional electronic spectroscopy. *Optics Letters*, 34(21):3301–3303, 2009.

[24] S.-H. Shim, D. B. Strasfeld, Y. Ling, and M. T. Zanni. Automated 2D IR spectroscopy using a mid-IR pulse shaper and application of this technology to the human islet amyloid polypeptide. *Proceedings of the National Academy of Sciences*, Jan 2007.

[25] J. A. Myers, K. L. M. Lewis, P. F. Tekavec, and J. P. Ogilvie. Two-color two-dimensional Fourier transform electronic spectroscopy with a pulse-shaper. *Optics Express*, 16(22):17420, Oct 2008.

[26] M. R. Wasielewski, D. G. Johnson, C. Preston, and M. Seibert. Determination of the primary charge separation rate in photosystem II reaction centers at 15 K. *Photosynthesis Research*, 22(1):89–99, 1989.

[27] M. R. Wasielewski and D. Johnson. Determination of the primary charge separation rate in isolated photosystem II reaction centers with 500-fs time resolution. *Proceedings of the National Academy of Sciences*, Jan 1989.

[28] J. P. M. Schelvis, P. I. Van Noort, T. J. Aartsma, and H. J. van Gorkom. Energy transfer, charge separation and pigment arrangement in the reaction center of photosystem II. *Biochimica et Biophysica Acta*, Jan 1994.

[29] H. Visser, M. L. Groot, F. van Mourik, I. H. M van Stokkum, J. P. Dekker, and R. van Grondelle. Subpicosecond transient absorption difference spectroscopy on the reaction center of photosystem ii: radical pair formation at 77 k: radical pair formation at 77 K. *Journal of Physical Chemistry*, Jan 1995.

[30] M. L. Groot, F. van Mourik, C. Eijckelhoff, I. H. M. van Stokkum, J. P. Dekker, and R. van Grondelle. Charge separation in the reaction center of photosystem II studied as a function of temperature. *Proceedings of the National Academy of Sciences*, Jan 1997.

[31] T. Renger and R. A. Marcus. Photophysical properties of PS-2 reaction centers and a discrepancy in exciton relaxation times. *Journal of Physical Chemistry B*, 106(7):1809–1819, Jan 2002. Pump Probe data for PSII at 77K.

[32] B. Donovan, L. A. Walker II, C. F. Yocum, and R. J Sension. Transient absorption studies of the primary charge separation in photosystem II. *Journal of Physical Chemistry*, 1996.

[33] A. R. Holzwarth, M. Müller, and M. Reus. Kinetics and mechanism of electron transfer in intact photosystem II and in the isolated reaction center: pheophytin is the primary electron acceptor. *Proceedings of the National Academy of Sciences*, Jan 2006.

[34] E. Romero, I. H. M. van Stokkum, V. I. Novoderezhkin, J. P. Dekker, and R. van Grondelle. Two different charge separation pathways in photosystem II. *Biochemistry*, 49(20):4300–4307, 2010.

CHAPTER III

Experimental Methods

This chapter details the experimental methods used to generate two-dimensional optical spectra. I first discuss the origin of the tunable laser pulses used in our experiments: from an oscillator to a regenerative amplifier, and finally to a noncollinear optical parametric amplifier (NOPA) or white light generation. Next I show how we manipulate theses pulses to compress or shape their amplitude and phase. I discuss prism compression as well as the Dazzler, an acousto-optic pulse shaper used to create a pair of pulses with a programmable time delay. To characterize our pulses, we use a technique called ZAP-SPIDER, and I briefly explain the process and demonstrate its results.

With the pulses properly compressed and characterized, I go into detail about the experimental set up for conducting 2DES in the pump-probe geometry. With highly scattering samples, scatter and unwanted signals can create large distortions within a 2D spectra, so I discuss scatter subtraction techniques, in particular using the phase-shaping capabilities of the Dazzler combined with traditional chopping schemes. While 2DES in the pump-probe geometry yields purely absorptive spectra, I show how altering the phase between the pumps enables retrieval of the rephasing and non-rephasing spectra as well.

Finally, I consider the difficulties in creating optical cells a liquid nitrogen tem-

peratures. Standard fused silica surfaces are hydophilic, which can lead to difficulties when attempting to form a uniform optical glass. I elaborate on the process we use to clean and passivate the surfaces to improve the quality of the optical glass in the sample cell at 77K.

While constructing and fine-tuning our 2D setup, we published a number of methods papers, demonstrating and improving techniques for 2DES in the pump-probe geometry, which will generally not be discussed in detail here. We were the first group to demonstrate 2DES in the visible with a pulse shaper [1], and we applied a method first conceived by De Boeij et al. for recovering both the rephasing and non-rephasing spectra [2, 3]. Next, we demonstrated 2DES using a continuum probe, to allow us observe the vibrational wavepacket motion and its oscillatory signatures in 2D spectra [4]. Finally, continuum probes can be difficult to compress, so we examined the distortions present in 2D spectra due to chirp [5], and developed a method for correcting for those distortions [6].

3.1 Pulse generation

In this section, I detail the portions of the experimental setup used to generate the pulses in our experiment, from the titanium sapphire oscillator to the creation of the broadband pulses used in the experimental setup.

3.1.1 Laser source

We begin with a commercially available (Femtosource Synergy) pumped titanium sapphire oscillator (Ti:Sapph) [7]. The mode-locked output has a repetition rate of 75 MHz and produces broadband (>100 nm, centered near 800 nm) pulses of approximately 12 fs. Output power can vary with environmental conditions, but typically ranges from 750-820 mW.

In order to obtain final pulse energies suitable for 2D spectroscopy, we use a small

fraction of the oscillator's output to seed a regenerative amplifier (Spectra Physics Spitfire Pro), which uses chirped pulse amplification [8]. Briefly, the seed is stretched with a grating pair to >2 ps to lower the instantaneous power of each pulse. Every millisecond a Pockels cell sends one of these stretched pulses into a cavity with a Ti:Sapph crystal where it is pumped with a Nd:Yag pump laser (Spectra Physics Empower). Each pass through the cavity amplifies the pulse, and when it it reaches the optimal amplification, a second Pockels cell switches out the pulse. The final amplified pulse is recompressed with a second grating pair. The final output is a 1 mJ, 800nm, ∼40 fs pulse at a 1 kHz repetition rate.

3.1.2 Non-collinear optical parametric amplifier

To generate the tunable visible pulses needed for the experiments we send the output of the regenerative amplifier into two independent home-built non-collinear optical parametric amplifiers (NOPAs) [9]. The NOPA takes the amplified pulse and uses it to generate pulses from the visible to the near-IR (∼480-700 nm), allowing us to access a wide variety of material systems.

In brief, half of the output from the regenerative amplifier enters the NOPA apparatus. Most of this beam (96%) is sent into a 0.5 mm Beta Barium Borate (BBO) crystal where it is frequency doubled. This pump beam is focused and sent into a second BBO crystal (2 mm) at a small angle, where it generates a parametric fluorescence ring. The beam is typically focused 2-3 cm before the crystal to avoid damaging the crystal. Meanwhile, a 4% reflection is focused into a sapphire window, where self-phase modulation produces chirped white light to act as a seed beam. This is focused and overlapped with the pump at the BBO. The angle between the pump and the white light (3-5°) is designed to take advantage of the spatial walk-off of the crystal to maximize spatial overlap throughout the length of the crystal.

Within the crystal, the pump undergoes a difference frequency process, where the

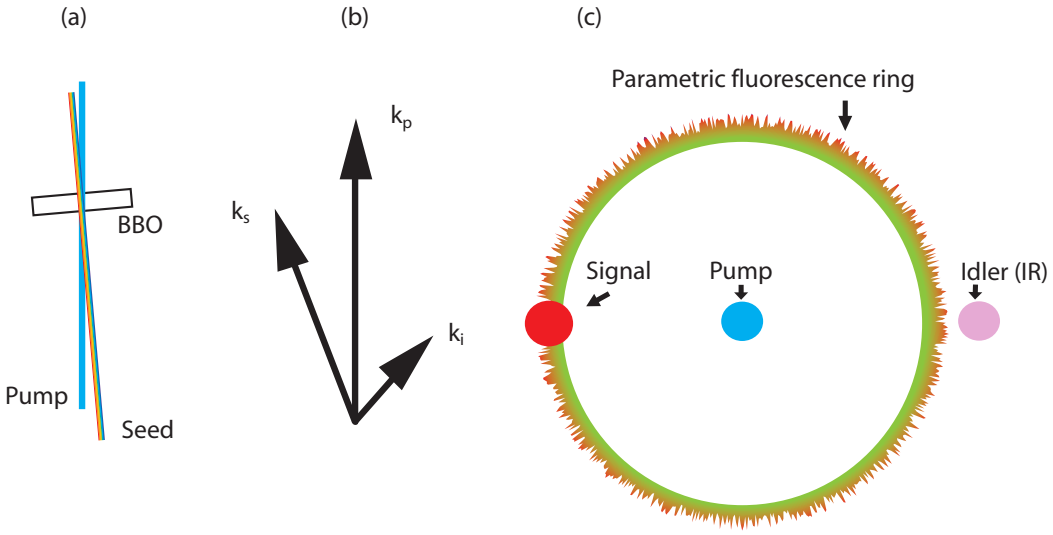

Figure 3.1: Cartoon depicting how a NOPA functions [10]. **a)** A top-down diagram showing the physical alignment of the NOPA beams. **b)** Wavevector diagram showing the relation between the signal, pump, and idler beams. **c)** Front view of the NOPA after the BBO.

seed beam preferentially defines the frequency of the signal, with $f_{\text{pump}} = f_{\text{signal}} + f_{\text{idler}}$. The tunability of the NOPA relies on the chirp of the white light. By having a time delay in the white light stage, we can temporally overlap different frequency components of the seed with the pump, changing the frequency of the amplified signal. Figure 3.1 is a cartoon showing the NOPA geometry. With this setup, we are able to produce pulses from with center wavelengths from ∼480 nm to ∼700 nm, and bandwidths up to 70 nm. The spectra of the pulses used in the experiments are shown in Figure 3.2.

3.1.3 White light generation

Light-harvesting systems are designed to absorb many different frequencies of light to utilize the broad solar spectrum [11]. In order to obtain the most information about how energy is transferred across these frequencies, a broader probe spectrum is desired, and the use of a continuum probe allows us to monitor frequencies not directly

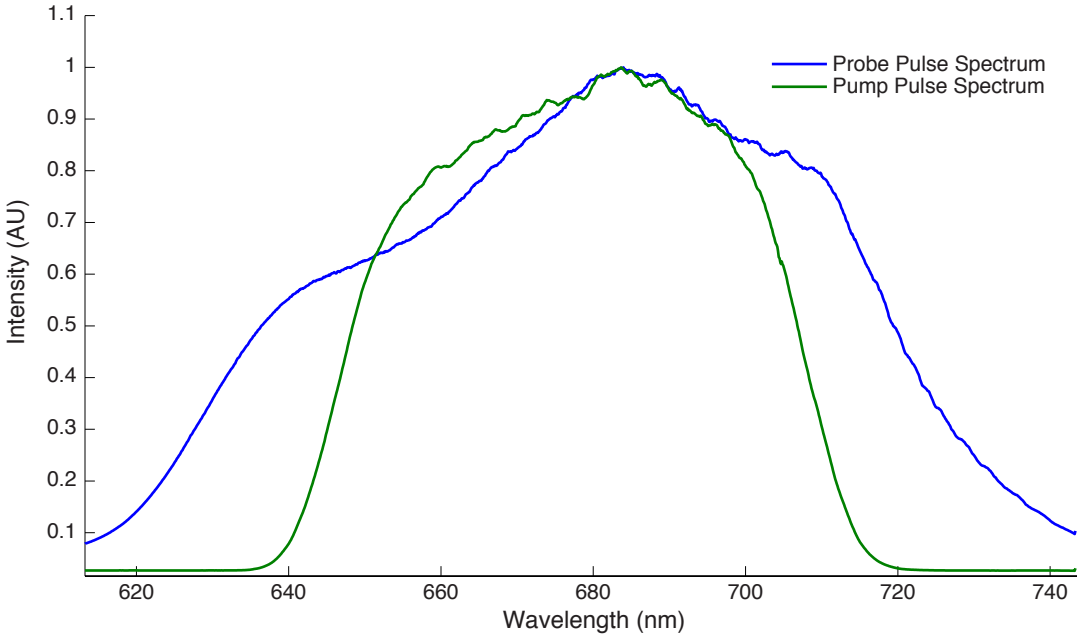

Figure 3.2: Normalized pump and probe NOPA spectra used in the experiments in Chapter IV. The pump spectrum comes after shaping via the Dazzler (Section 3.2.2) and the probe pulse is compressed with a prism compressor (Section 3.2.1).

excited [4]. In our setup, we can route the input of the second NOPA to generate a continuum probe instead. In this case, a fraction of the output of the regenerative amplifier is focused into a 2 mm sapphire window. Self-phase modulation generates the continuum beam and the output is collimated to either be compressed or used directly in our 2D setup.

This method of generating white light often creates sizeable linear chirp on the pulses. Given the large bandwidth of the beam, it can be difficult to compress with the prism compressors we normally employ for our NOPA-generated probe. Therefore, the chirp is often left uncorrected and characterized. For large t_2 delays, the chirp will have little effect on the 2D spectra. At early delays, it can cause distortions in the spectra, as different frequency components have different effective t_2 values. Our group has shown that the effects of chirp on 2D spectra can be quantified [5] and even corrected [6].

3.2 Pulse manipulation

3.2.1 Prism compressor

For ultrafast spectroscopic studies, the experimental time resolution is limited by the length of the exciting pulses in time. Therefore it is important to compress each pulse to account for all material dispersion before the pulse encounters the sample. For our probe beam, we use a standard prism compressor. Four-prism sequences have been shown to have negative dispersion [12], and to make the system compact, we double pass the beam through two prisms, as shown in our experimental setup (Figure 3.6). The probe beam enters the compressor at the tip of the first prism. The beam is dispersed and passed through a second, idential prism at a fixed prism separation, collimating the beam in the Fourier plane. A folding mirror returns the beam along its input path at a slightly different height, allowing a pick-off mirror to

collect the beam upon exiting the compressor.

The prism separation determines the amount of negative dispersion that is added and this can be calculated analytically [12, 13]. Day-to-day adjustments to the compression can be made without changing the prism separation by having the first prism mounted on a stage to effectively insert more (or less) glass into the beam as it enters the compressor, adding additional positive (negative) dispersion. The prism should be mounted such that the motion is parallel to the rear face of the prism to prevent alignment changes of the compressor. Since adding material dispersion is considerably easier than removing it, it is preferred to err on the side of too much negative dispersion in the compressor rather than too little. Note that a prism compressor can add negative dispersion to not only compensate for dispersive optics prior to the compressor, but it can also "precompress" the pulse to account for dispersive optics throughout the beam path up to the sample, where the pulse width should be shortest and ideally transform-limited.

The prism material should be chosen carefully when designing a prism compressor. Glasses that are highly dispersive will require shorter prism separations than weakly dispersive glasses. However, while the prism compressor is quite effective at removing second order dispersion, the prisms themselves add higher-order dispersion terms. Therefore, one must choose a glass material that balances effective removal of second-order dispersion without adding too much higher-order dispersion. In the photosystem II experiments, SF11 was chosen, and in other experiments, fused silica prisms were used.

3.2.2 DAZZLER

The Dazzler is a commercially available acousto-optic programmable dispersive filter (AOPDF), available in the UV, Visible, or NIR wavelength regimes. It offers amplitude control and phase control up to the fourth order, allowing for precise pulse

control when placed after a NOPA [14]. Inside the Dazzler, the beam passes through a nonlinear birefringent crystal. An RF generator creates a programmable acoustic wave that diffracts a portion of the beam at the Bragg angle, with both amplitude and phase control.

With independent control over four orders of phase and amplitude masks to set the bandwidth of the pulse, the Dazzler is quite effective at compressing the input NOPA beams to near-transform limited widths. At the wavelengths used in the photosystem II experiments, the Dazzler-shaped NOPA can be used to create ∼28 fs pulses with 40-60 nm of bandwidth. In the photosystem II experiments, pulse energies are generally attenuated to 10 nJ per pulse to avoid exciton annihilation effects and bleaching of the sample.

For generating the pulse pair, we overlay the following amplitude and phase mask to the parameters required to obtain the following shaped electric field:

$$A_{\text{mask}} = |E(\omega)| \left(1 + e^{i\omega t_1 + i\phi_{12}}\right) \tag{3.1}$$

where $|E(\omega)|$ represents the spectral amplitude of the pulse, and ϕ_{12} is the relative carrier wave phase shift between the pulses. This can be used to manipulate the signal using phase cycling schemes as detailed in Section 3.3.1.

3.2.3 Pulse characterization

To characterize the pulses used for the experiments in Chapter 4, we constructed a setup for zero-additional-phase spectral interferometry for direct electric field reconstruction (ZAP-SPIDER) as developed by Baum and Riedle [15]. In the original SPIDER setup, two copies of the test pulse are created. A time delay is generated between the two, and both pulses are frequency mixed with a chirped pulse in a nonlinear crystal such as a BBO. Due to the chirp on the auxiliary pulse and the delay

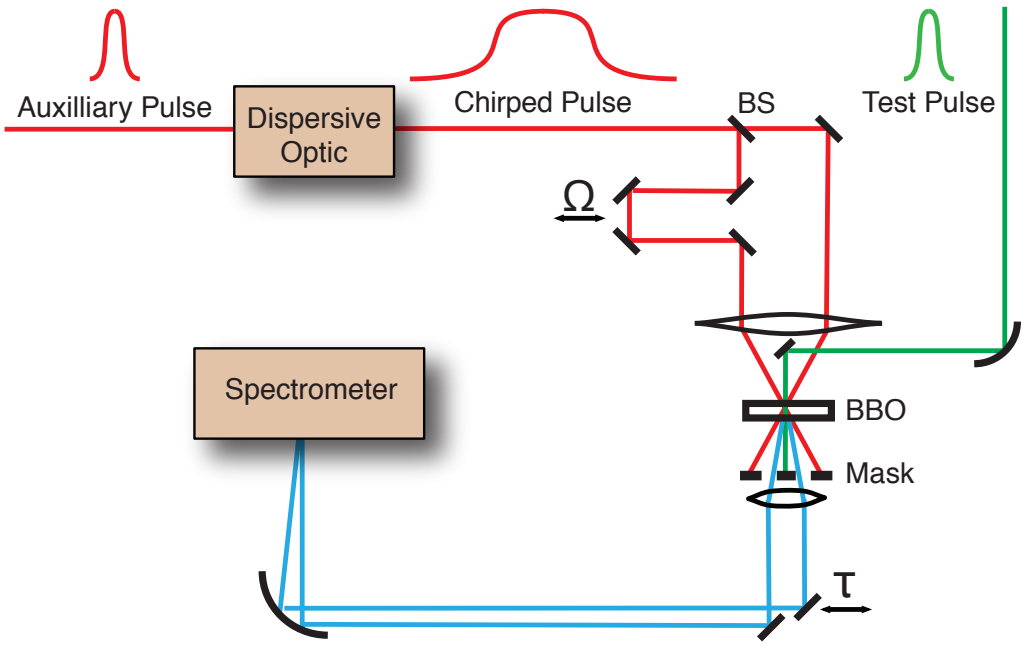

Figure 3.3: The ZAP-SPIDER setup. The test pulse is a portion of the output from regenerative amplifier, and the test pulse is the pump or probe pulse taken directly before the sample.

between the test pulses, each test pulse interacts with a different spectral region of the auxiliary pulse, resulting in spectrally sheared upconverted pulses. These can be interfered in a spectrometer; if the pulses were identical and simply time delayed, one would expect a known fringe-space in the interferogram. Since the pulses are spectrally sheared, this creates deviations from the expected fringe spacing, allowing for the full electric field of the test pulse to be reconstructed [16].

In a ZAP-SPIDER setup, two copies are made of the auxiliary pulse instead of the test pulse. This allows for the test pulse to pass through no additional dispersive optics before being analyzed, which can provide a more direct measurement of the pulse as it exists directly before the sample in the experimental setup. The setup for our ZAP-SPIDER apparatus is shown in Figure 3.3.

In brief, an auxiliary pulse (in our case taken as a portion of the 800nm pulse from the regenerative amplifier) is passed through a highly dispersive optic to create a

chirped pulse of ∼3 ps in time. Two copies of this pulse are created with an adjustable time delay, Ω. Both arms of the interferometer are sent into a large diameter lens such that they will converge at a BBO crystal at the focal point of the lens. A curved mirror is used to focus the test pulse at the BBO, and a small pick-off mirror in front of the lens is used to send it directly between the two converging auxiliary pulses. For visible test pulses, the BBO is aligned for sum-frequency generation (SFG), and two UV pulses are generated, which can be spatially selected with an appropriate mask. These pulses are collimated, and subsequently focused onto the slit of a spectrometer to interfere. One of the arms is adjustable to create and optimize the time delay between the UV pulses. Much as in a SPIDER setup, the two UV pulses are spectrally sheared with respect to one another due to the time delay on the chirped pulses, allowing for the full reconstruction of the electric field. Spectral amplitude and phase information for a retrieved pulse can be found in Figure 3.4 while the temporal profile can be found in Figure 3.5. For more detailed information on the ZAP-SPIDER algorithm used, see [10, 16].

3.3 Pump-probe geometry

Throughout this thesis, 2D spectra are collected using the pump-probe geometry, which was initially proposed by Faeder and Jonas [17], and first implemented in the IR by Shim et al. [18]. This geometry uses a programmable pulse-shaper (Fastlite Dazzler) to create the first two pulses collinearly. These two pump pulses are crossed at a small angle with an independent probe pulse at the sample. The probe beam and the signal are collinear and dispersed in a spectrometer (Horiba Jobin-Yvon iHR320). The signal is recorded and averaged for several hundred laser shots per t_1 value on a self-cooling charge coupled device (CCD) (Princeton Instruments Pixis 100B). This geometry is comparatively simple to set up; a traditional frequency-resolved transient absorption experiment is readily converted into a 2D spectrometer

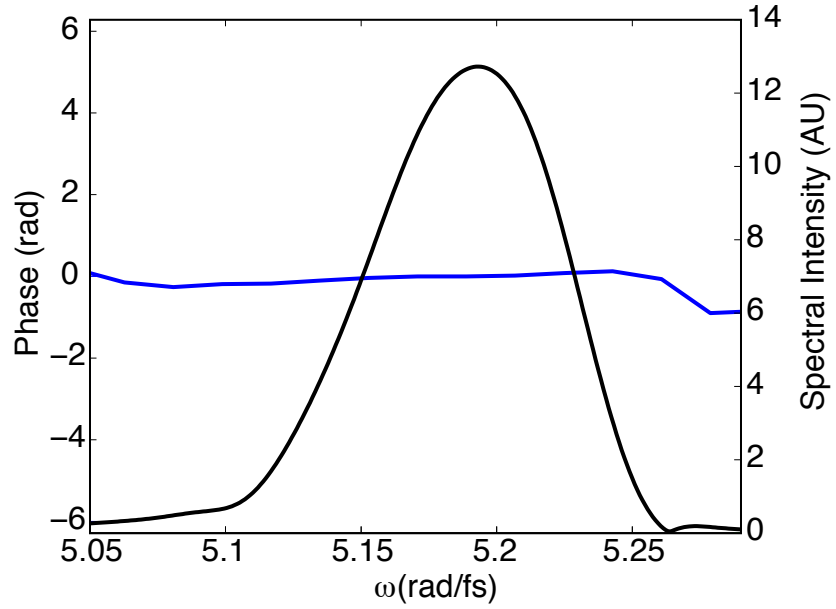

Figure 3.4: Spectral amplitude and phase for a retrieved pulse from the ZAP-SPIDER setup. This pulse is near transform-limited.

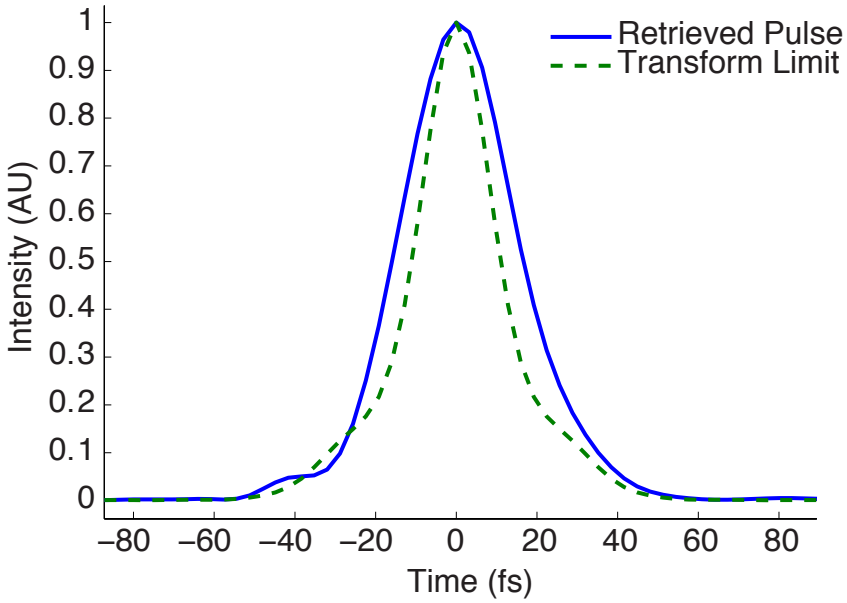

Figure 3.5: The solid line shows the temporal profile for a near transform-limited pulse retrieved from the ZAP-SPIDER algorithm, while the dashed line shows the transform-limit. The pulse has a FWHM of ∼28 fs.

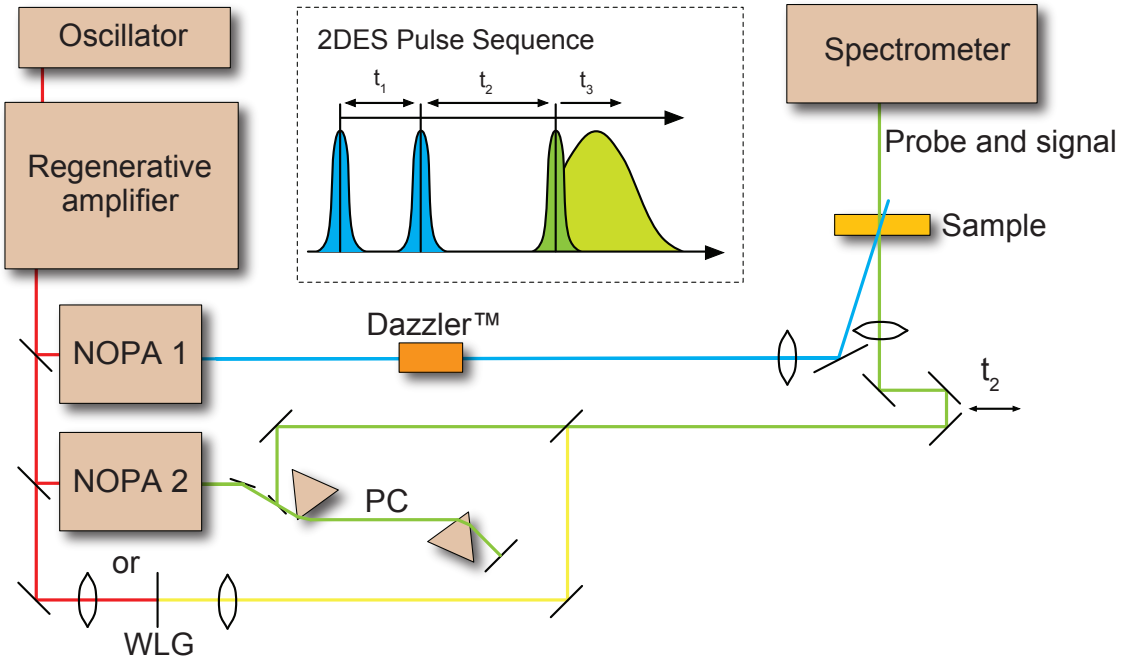

Figure 3.6: The experimental setup for 2DES in the pump-probe geometry. NOPA 1 creates the pump pulse which is split with a programmable time delay in the Dazzler. NOPA 2 creates the probe pulse which is compressed with a prism compressor (PC) and crossed with the pump pulses at the sample. The probe and signal are frequency-resolved in the spectrometer. Alternatively, a continuum pulse from white light generation (WLG) can be used as the probe pulse.

through the addition of a pulse shaper into the pump beam.

In our setup (Figure 3.6), we send one NOPA to the Dazzler to create pump pulses, while a second, independently tunable NOPA acts as the probe pulse [1]. This allows for two-color 2DES, providing access to a wider range of frequency-frequency space, and allowing us to monitor samples with large Stokes shifts, or with energy transfer between chromophores with disparate frequency responses. In addition, this setup is readily adapted to use with a continuum probe, in order to monitor multiple transitions [4].

In this geometry, $\mathbf{k}_1 = \mathbf{k}_2$, so the rephasing ($\mathbf{k}^{(R)} = -\mathbf{k}_1 + \mathbf{k}_2 + \mathbf{k}_3$) and nonrephas-

ing signals ($\mathbf{k}^{(NR)} = \mathbf{k}_1 - \mathbf{k}_2 + \mathbf{k}_3$) are both emitted along the direction of the probe pulse, which also acts a local oscillator for heterodyned detection in a spectrometer. Since both rephasing and non-rephasing signals are collected at the same time, the measured spectra readily gives an absorptive 2D spectrum, without the need for complicated phasing procedures required to add the rephasing and non-rephasing spectra in other geometries where the two are collected separately [19, 20].

The use of a pulse shaper to programmatically generate the t_1 delay between the pump pulses provides a distinct advantage compared to fully non-collinear geometries using refractive t_1 delays. When a refractive delay is used to generate t_1, spectral interferometry must be used to determine the precise location of $t_1 = 0$. Minor inaccuracies in this calibration can lead to difficulties with phasing.

The signal is collected in the (t_1, ω_3) domain for any given t_2 value. Signal is measured only for $t_1 > 0$. However, since the two pump pulses are identical, the overall signal should be symmetric with respect to $t_1 = 0$. We can enforce this without the need to take additional data for $t_1 < 0$ by using properties of the Fourier transform. A symmetric function will be purely real in Fourier space. Therefore, we first Fourier transform the signal into the (ω_1, ω_3) domain, and keep only the real portion.

In order to retrieve the full complex signal in the (ω_1, ω_3) domain, we must also enforce causality; no 2D signal should exist prior to the probe pulse's arrival. This is imposed by inverse Fourier transforming into the (ω_1, t_3) domain and applying a Heaviside function, $\Theta(t_3)$, to the data [21]. A final Fourier transform into the (ω_1, ω_3) domain yields a complex signal where the real portion corresponds to the absorptive spectrum and the imaginary component corresponds to the dispersive spectrum.

3.3.1 Scatter subtraction techniques

Sources of scatter

When taking two-dimensional spectra, it is important to consider the sources for all the light entering the detector. Without taking care to remove them, many unwanted signals and scatter signatures can enter the data, complicating later analysis. Ideally, we wish to extract only the heterodyned 2D signal. In a BOXCAR geometry, spatial filtering removes many unwanted signals. In the pump-probe geometry, however, the collinearity of the pump beams introduces addition transient absorption signals that are phase matched with the 2D signal. In a highly scattering sample, the total signal detected in the spectrometer is S_{det} and contains contributions from many sources: scatter from each of the pumps (with electric fields E_1 and E_2), the probe beam (with field E_3) and the desired signal (E_S), as well as pump-probe signals from each pump-probe pair (E_{pp_1} and E_{pp_2}):

$$S_{\mathrm{det}} = \left| E_1 + E_2 + E_3 + E_S + E_{\mathrm{pp}_1} + E_{\mathrm{pp}_2} \right|^2 \tag{3.2}$$

where $E_S \sim E_1^* E_2 E_3$, $E_{\mathrm{pp}_1} \sim E_1 E_1^* E_3$, and $E_{\mathrm{pp}_2} \sim E_2 E_2^* E_3$. In analyzing our scatter, we neglect small terms such as $|E_S|^2$ and those where a signal is heterodyned with either pump pulse, such as $E_1 E_S^*$ and $E_{\mathrm{pp}_1} E_2^*$. This leaves:

$$\begin{aligned} S_{\mathrm{det}} \approx \underbrace{|E_1|^2 + |E_2|^2 + |E_3|^2}_{\text{scatter from individual pulses}} + \underbrace{E_1 E_2^* + E_1^* E_2}_{\text{pump-pump}} + \underbrace{E_1 E_3^* + E_1^* E_3}_{\text{pump-probe}} + \underbrace{E_2 E_3^* + E_2^* E_3}_{\text{pump-probe}} \\ + \underbrace{E_S E_3^* + E_S^* E_3}_{\text{heterodyned signal}} + \underbrace{E_{\mathrm{pp}_1} E_3^* + E_{\mathrm{pp}_1}^* E_3}_{\text{transient absorption signal 1}} + \underbrace{E_{\mathrm{pp}_2} E_3^* + E_{\mathrm{pp}_2}^* E_3}_{\text{transient absorption signal 2}} \end{aligned} \tag{3.3}$$

The first three underlined contributions result from scatter from each beam interfering in the spectrometer. These contributions can be simulated and are shown in Figure 3.7, assuming transform limited gaussian pulses of 30 fs at a time delay t_2=150 fs. Note that the interference from the second pump pulse and the probe pulse will

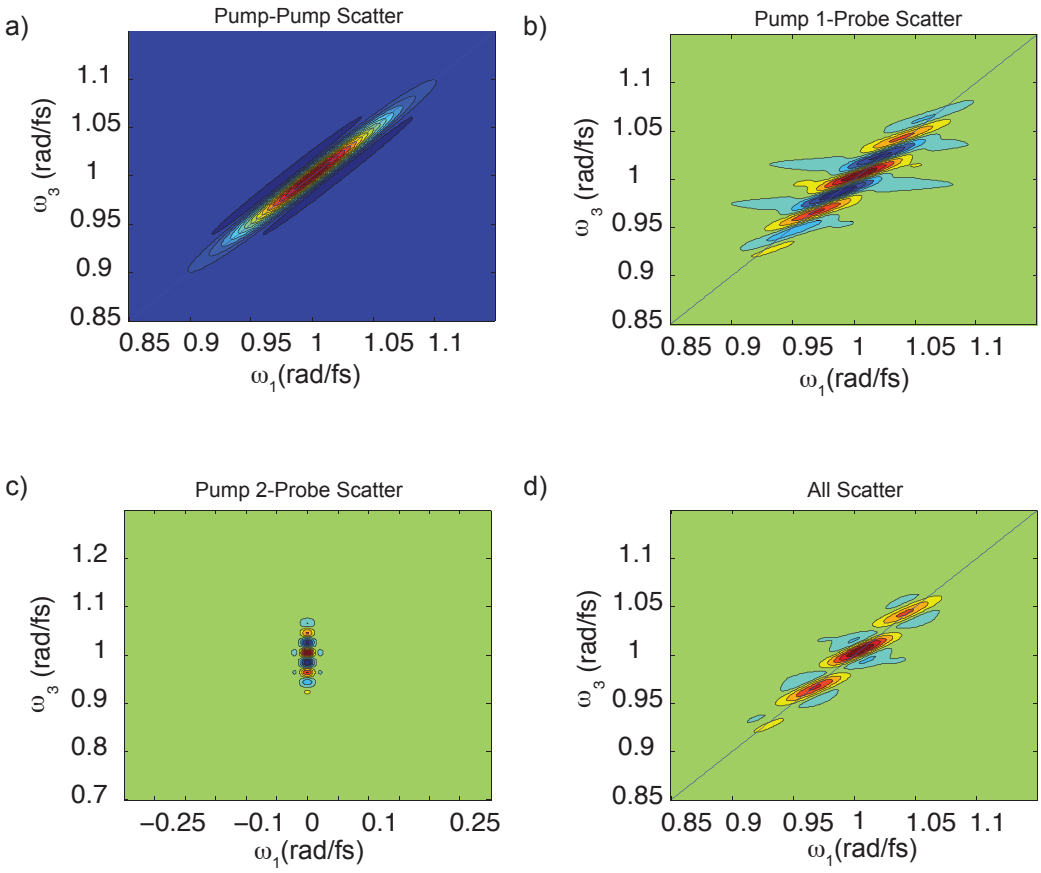

Figure 3.7: Simulated scatter images showing representative signatures of the scatter from different beam combinations for $t_2 = 150$ fs. The background color in each graph represents zero, while blue represents negative values and red indicate positive values. **a)** Scatter from the two pump beams interfering produces a strong diagonal peak. **b)** Scatter from pump 1 and the probe creates a modulation along the diagonal that is dependent on t_2. **c)** Scatter from pump 2 and the probe is not dependent on t_1, and therefore shows up at 0 frequency in ω_1. **d)** The total scatter signature when the signals from **a** and **b** are combined equally.

not be dependent on t_1, and will therefore will appear at zero frequency in ω_1. The transient absorption signals will be sample-dependent. As in the scatter contributions, the transient absorption contribution from the second pump pulse will not be t_1 dependent, and will appear at zero frequency in ω_1.

Phase-cycling

The phase of the 2D signal depends on the difference between the phases of the pump pulses and the difference in the phases of the probe and the reference pulse [20]:

$$\phi_S = \pm(\phi_1 - \phi_2) + (\phi_3 - \phi_{ref}) \tag{3.4}$$

In the pump-probe geometry, the probe beam also serves as the reference pulse, so the phase of the signal depends solely on $\phi_{12} = \phi_2 - \phi_1$. Since transient absorption signals will only depend on one of the two pump pulses, they will not be dependent on ϕ_{12}. When ϕ_{12} shifts by a factor of π, the sign of the 2D signal will flip, yet transient absorption signals will not. Subtraction schemes thus allow separation of the 2D signal. Since we have individual control of the phase of each pump pulse through the Dazzler, we simply have to apply a variety of pump phases for each t_1 delay and add the measured spectra, $I(\phi_1, \phi_2, \phi_3)$, appropriately to remove most of the unwanted signals, as originally implemented for 2D IR spectroscopy in [22]. In simplified notation, $E_j \sim A_j \exp(i\phi_j)$, and applying the appropriate phases to equation 3.3, we recover the following for a four-phase cycling scheme:

$$\begin{aligned} I(0,0,\phi_3) - I(0,\pi,\phi_3) + I(\pi,\pi,\phi_3) - I(\pi,0,\phi_3) = \\ \underbrace{4\left[A_1^* A_2 |A_3|^2 + A_1 A_2^* |A_3|^2\right]}_{3^{\text{rd}} \text{ order heterodyned signal}} + \underbrace{4\left[A_1 A_2^* + A_2^* A_1\right]}_{\text{pump-pump scatter}} \end{aligned} \tag{3.5}$$

We note that this phase-cycling scheme is successful in removing the contributions

Label	A_1	A_2	B_1	B_2	C_1	C_2	D_1	D_2	E_1	E_2
Pump 1	0	0	0	0	π	π	π	π	Off	Off
Pump 2	0	0	π	π	π	π	0	0	Off	Off
Probe	On	Off	On	Off	On	Off	On	Off	On	Off

Table 3.1: Ten different pulse combinations that can be used to recover the desired 2D signal. The numbers given indicate the phase of a given pulse.

from undesired transient absorption signals, and that this scheme does not reduce the duty cycle of the experiment, as typical chopping schemes do. Each measured spectrum contains recoverable signal. Unfortunately, this scheme fails to remove a contribution from pump-pump scatter. As seen in Figure 3.7, this can cause a substantial diagonal distortion in highly scattering samples.

Differential detection

In order to further improve the quality of the recovered 2D spectra, we turn to differential detection in order to remove the remaining pump-pump scatter.

Traditionally in a differential detection scheme, the pump is chopped and the signal is the difference of the measured spectra with and without the pump. Our goal here, however, is to measure the pump-pump scatter that enters the spectrometer, so that it can be removed. This necessitates chopping of the probe beam instead of the pumps. When the probe is blocked, the only source of light entering the spectrometer will be pump-pump scatter; all other signals and scatter depend on the existence of the probe. Since the interference between the pumps will change as ϕ_{12} varies, we measure this scatter for each phase pair. Table 3.1 shows the 8 pulse sequences required to implement the four phase cycling scheme above as well as to remove the remaining pump-pump scatter. The schemes discussed here use the following pulse

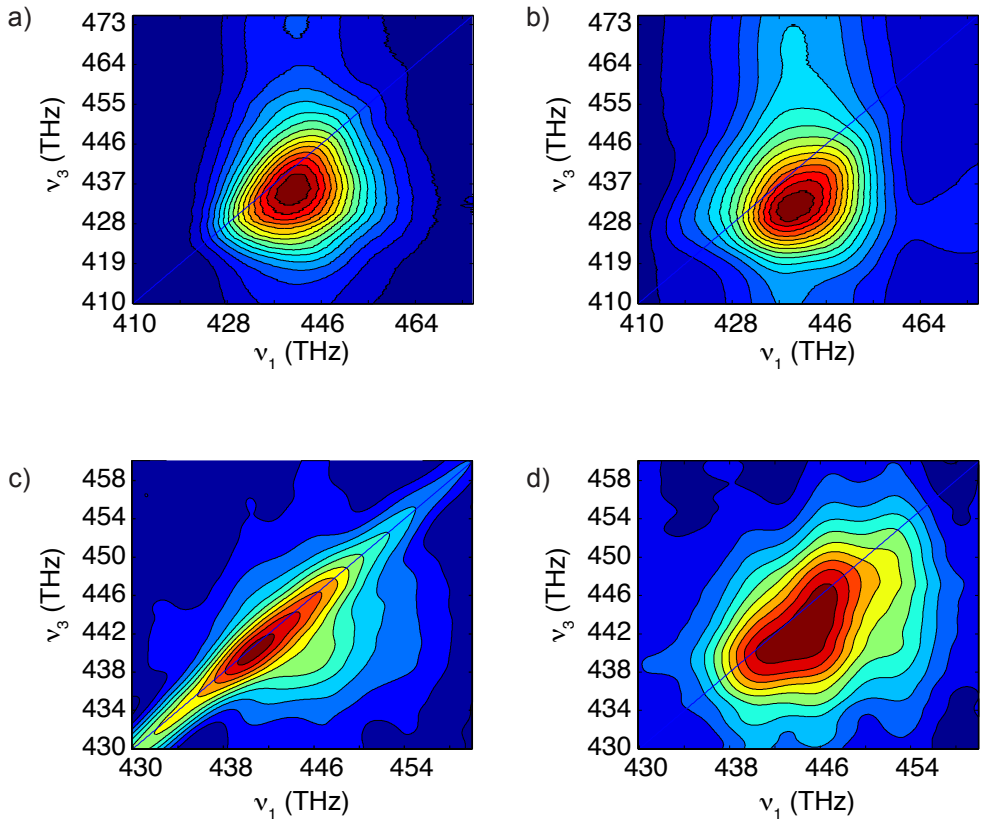

Figure 3.8: **a)** and **b)**: Absorptive spectra of rhodamine-800 in ethanol at $t_2 = 100$ fs. Spectrum **a)** uses traditional differential detection (Eq. 3.6), and uses no probe chopping or phase cycling schemes. Spectrum **b)** adds the four phase cycling scheme (Eq. 3.7) to remove pump-probe scatter. The difference between **a)** and **b)** is subtle, yet would significantly affect peak shape analysis. This sample was not highly scattering, so no significant contributions from pump-pump scatter are found. **c)** and **d)**: Absorptive spectra of room temperature D1-D2 complexes at $t_2 = 240$ fs. Spectrum **c)** uses the four phase-cycling method without probe chopping (Eq. 3.7). Spectrum **d)** uses the phase cycling method along with chopping the probe (Eq. 3.8), removing the significant pump-pump scatter and revealing the underlying peak shapes.

sequences:

Traditional Differential Detection:

$$S_{2D} = A_1 - E_1 \tag{3.6}$$

Four Phase Cycling Scheme:

$$S_{2D} = (A_1 - B_1) + (C_1 - D_1) \tag{3.7}$$

Four Phase Cycling with Probe Chopping:

$$S_{2D} = ((A_1 - A_2) - (B_1 - B_2)) + ((C_1 - C_2) - (D_1 - D_2)) \tag{3.8}$$

Typical output using these three schemes can be seen experimentally in Figure 3.8. The first row shows the difference between traditional differential detection and the four phase cycling scheme in a low-scatter sample. The difference is subtle, but the four phase cycling scheme does remove some distortions along the diagonal. The second row compares the four phase cycling scheme with and without probe chopping. This sample is highly scattering, and the pump-pump scatter is quite evident in spectrum c). The probe chopping allows for the underlying peak shape to be revealed.

3.3.2 Reconstruction of rephasing and non-rephasing spectra

While the pump-probe geometry provides a simple way to retrieve the absorptive spectrum without complicated phasing procedures, it can be helpful to recover both the rephasing and non-rephasing signals separately. De Boeij et al. proposed a method for recovering these signals from frequency-resolved pump-probe data [2, 3], and the method is readily adaptable to 2DES [1]. The signal is directly dependent on $\phi_{12} = \phi_2 - \phi_1$ and is independent of the probe phase. Specifically, the signal is proportional

to the sum of the rephasing and non-rephasing response functions:

$$S(\omega_3, t_2, t_1) \propto \mathrm{Re}\left[E_3^*(\omega_3)\left\{R^{(R)}(\omega_3, t_2, t_1)e^{-i\phi_{12}} + R^{(NR)}(\omega_3, t_2, t_1)e^{i\phi_{12}}\right\}\right] \tag{3.9}$$

For $\phi_{12} = 0$ and $\phi_{12} = \pi/2$, we recover:

$$\begin{aligned} S_0(t_3, t_2, t_1) &\propto R^{(R)}(t_3, t_2, t_1) + R^{(NR)}(t_3, t_2, t_1) \\ S_{\pi/2}(t_3, t_2, t_1) &\propto -iR^{(R)}(t_3, t_2, t_1) + iR^{(NR)}(t_3, t_2, t_1) \end{aligned} \tag{3.10}$$

These can then be combined as in equation 3.11. This separation is demonstrated for in a two-color 2D spectrum of a dye in Figure 3.9.

$$\begin{aligned} R^{(R)}(t_3, t_2, t_1) &\propto S_0(t_3, t_2, t_1) + iS_{\pi/2}(t_3, t_2, t_1) \\ R^{(NR)}(t_3, t_2, t_1) &\propto S_0(t_3, t_2, t_1) - iS_{\pi/2}(t_3, t_2, t_1) \end{aligned} \tag{3.11}$$

3.4 Low-temperature considerations

In order to better resolve overlapping electronic transitions, it is helpful to record 2D spectra at 77 K. We use a liquid nitrogen cryostat (Oxford Instruments, MicroStatN) with a custom-designed optical sample cell [10, 23]. The sample cell is designed to have a short (380 μm) pathlength with fused silica windows for good optical transmission.

3.4.1 Preparing the windows

Clean, hydrophobic windows are key for a cell to produce an optical glass with low scatter. Fused silica is an ideal choice for its optical properties, but it is by nature hydrophilic. Attempting to freeze a water-based sample results in a largely

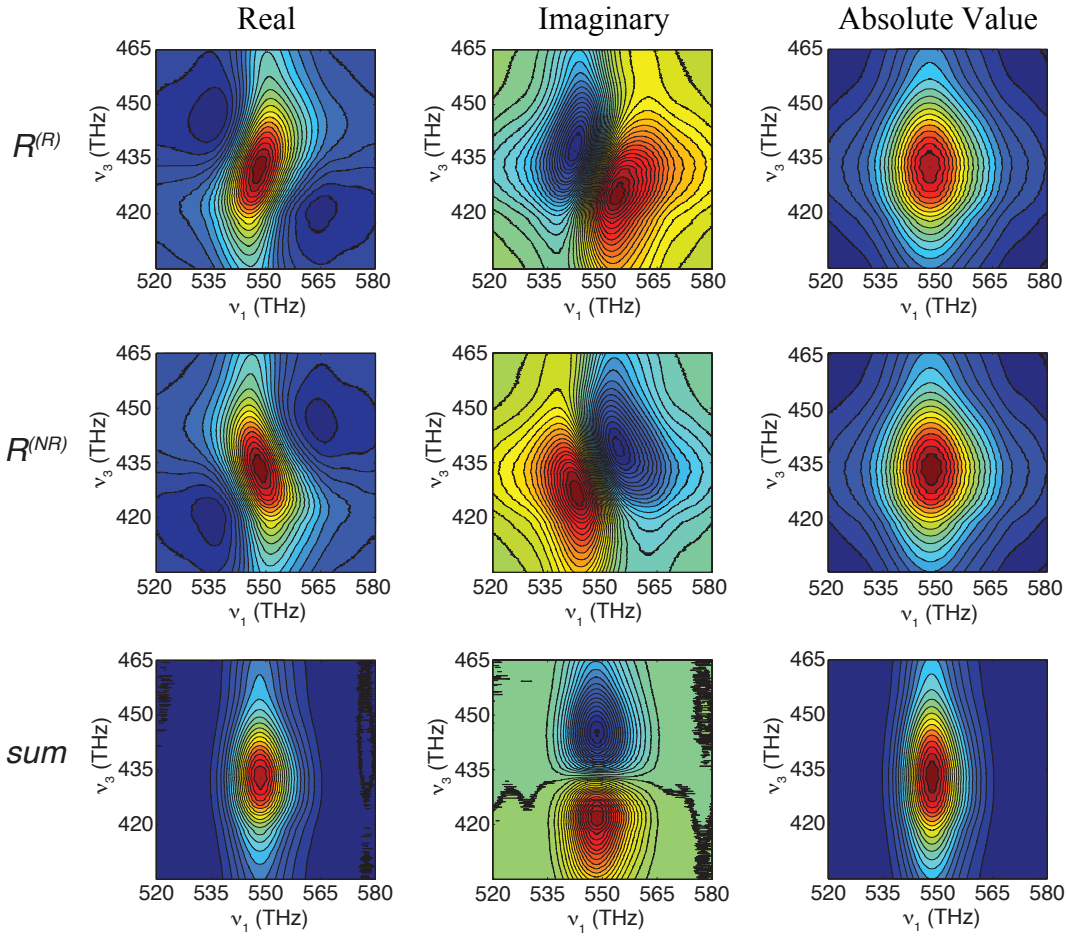

Figure 3.9: Two color 2D spectra showing the separation of the rephasing and nonrephasing spectra of LDS 750 in acetonitrile at $t_2 = 500$ fs. The top row contains the rephasing spectra, the middle row contains the nonrephasing spectra, and the bottom row shows the sum.

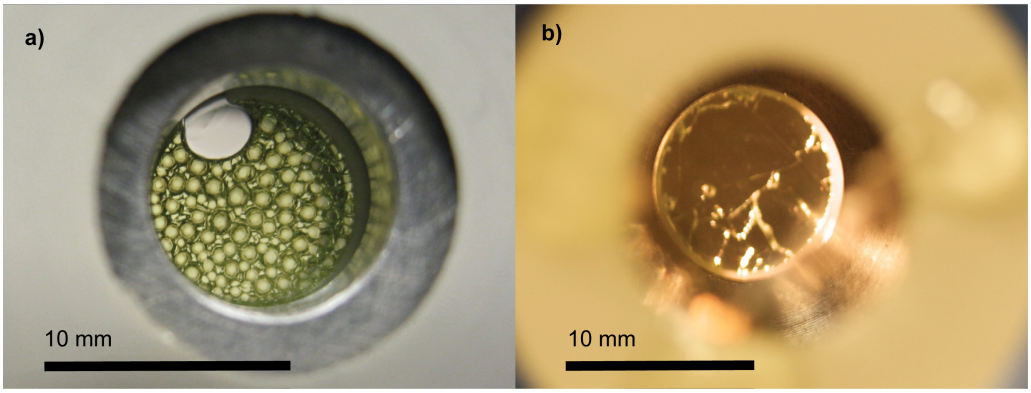

Figure 3.10: **a)** An example of the freezing pattern obtained with a 2:1 glycerol:water-based PSII sample at 77K with untreated fused silica windows. **b)** An example of another PSII sample with windows treated as in the text. While there are still cracks visible, there are large uncracked areas available for measurements.

fragmented optical glass, with varying optical densities and large scatter (see Figure 3.10). We have found that the windows must be thoroughly cleaned and the hydrophilic surface must be passivated before assembly. The cleaning process involves a number of sonication steps to ensure that the windows are thoroughly clean prior to cell assembly. Fused silica windows (0.5 mm thick) are sonicated for 5 minutes in a solution of Micro-90 and Dri-Clean detergents. The windows are removed from the soapy water and rinsed/sonicated in distilled water. The windows are then incubated in a beaker of Rain-X solution for 5 minutes. The Rain-X-coated windows are thoroughly buffed with lens paper until dry to ensure even treatment of the surface. A final sonication step in distilled water removes any residual lint from the lens paper, and the windows are blown dry with compressed nitrogen. Water should bead up on the now hydrophobic surface.

3.4.2 Assembling the cell

The sample cell should be cleaned with tissue and water between runs. O-rings are lightly coated with vacuum grease and wiped clean when first installed, but may be used for multiple runs without incident. A teflon spacer is placed on a freshly-treated window and set in the bottom of the cell. The sample should have 66% glycerol by volume, and 25 μL is pipetted into the center of the cell. Care must be taken to avoid bubbles, particularly in samples that contain detergent. It is best not to break the surface tension of the sample at this stage if possible. The top window is gently placed directly on the sample and followed quickly with top of the sample cell. The cell is screwed together carefully in a star pattern to avoid asymmetric localized pressure on the windows.

References

[1] J. A. Myers, K. L. M. Lewis, P. F. Tekavec, and J. P. Ogilvie. Two-color two-dimensional Fourier transform electronic spectroscopy with a pulse-shaper. *Optics Express*, 16(22):17420, Oct 2008.

[2] W. P. de Boeij, M. S. Pshenichnikov, and D. A. Wiersma. Ultrafast solvation dynamics explored by femtosecond photon echo spectroscopies. *Annual Review of Physical Chemistry*, 49(1):99–123, 1998.

[3] W. P. de Boeij, M. S. Pshenichnikov, and D. A. Wiersma. Heterodyne-detected stimulated photon echo: applications to optical dynamics in solution. *Chemical Physics*, Jan 1998.

[4] P. F. Tekavec, J. A. Myers, K. L. M. Lewis, and J. P. Ogilvie. Two-dimensional electronic spectroscopy with a continuum probe. *Optics Letters*, 34(9):1390–1392, 2009.

[5] P. F. Tekavec, J. A. Myers, K. L. M. Lewis, F. D. Fuller, and J. P. Ogilvie. Effects of chirp on two-dimensional Fourier transform electronic spectra. *Optics Express*, 2010.

[6] P. F. Tekavec, K. L. M. Lewis, F. D. Fuller, J. A. Myers, and J. P. Ogilvie. Toward broad bandwidth 2-D electronic spectroscopy: Correction of chirp from a continuum probe. *IEEE Journal of Selected Topics in Quantum Electronics*, PP(99):1–8, 2011.

[7] A. Stingl, M. Lenzner, C. Spielmann, F. Krausz, and R. Szipöcs. Sub-10-fs mirror-dispersion-controlled Ti:sapphire laser. *Optics Letters*, 20(6), Jan 1995.

[8] P. Maine, D. Strickland, P. Bado, M. Pessot, and G. Mourou. Generation of ultrahigh peak power pulses by chirped pulse amplification. *IEEE Journal of Quantum Electronics*, 24(2), Feb 1988.

[9] T. Wilhelm, J. Piel, and E. Riedle. Sub-20-fs pulses tunable across the visible from a blue-pumped single-pass noncollinear parametric converter. *Optics Letters*, 22(19):1494–1496, 1997.

[10] J. A. Myers. *Two-dimensional electronic spectroscopy of the photosystem II D1D2-cyt.*b559 *reaction center complex*. PhD thesis, University of Michigan, 2010.

[11] R. Blankenship. *Molecular Mechanisms of Photosynthesis*. Blackwell Sciences, Oxford, UK, 2002.

[12] R. L. Fork, O. E. Martinez, and J. P. Gordon. Negative dispersion using pairs of prisms. *Optics Letters*, May 1984.

[13] C. G. Durfee, J. A. Squier, and S. Kane. A modular approach to the analytic calculation of spectral phase for grisms and other refractive/diffractive structures. *Optics Express*, Oct 2008.

[14] A. Monmayrant, A. Arbouet, B. Girard, B. Chatel, A. Barman, B. J. Whitaker, and D. Kaplan. AOPDF-shaped optical parametric output in the visible. *Applied Physics B*, 81:177–180, 2005.

[15] P. Baum and E. Riedle. Design and calibration of zero-additional-phase SPIDER. *Journal of the Optical Society of America B*, Sep 2005.

[16] C. Iaconis and I. Walmsley. Self-referencing spectral interferometry for measuring ultrashortoptical pulses. *IEEE Journal of Quantum Electronics*, Apr 1999.

[17] S. Faeder and D. Jonas. Two-dimensional electronic correlation and relaxation spectra: Theory and model calculations. *Journal of Physical Chemistry A*, 1999.

[18] S.-H. Shim, D. B. Strasfeld, Y. Ling, and M. T. Zanni. Automated 2D IR spectroscopy using a mid-IR pulse shaper and application of this technology to the human islet amyloid polypeptide. *Proceedings of the National Academy of Sciences*, Sep 2007.

[19] T. Brixner, T. Mančal, I. V. Stiopkin, and G. R. Fleming. Phase-stabilized two-dimensional electronic spectroscopy. *Journal of Chemical Physics*, Sep 2004.

[20] M. L. Cowan, J. P. Ogilvie, and R. J. D. Miller. Two-dimensional spectroscopy using diffractive optics based phased-locked photon echoes. *Chemical Physics Letters*, 2004.

[21] M. F. Emde, W. P. de Boeij, M. S. Pshenichnikov, and D. A. Wiersma. Spectral interferometry as an alternative to time-domain heterodyning. *Optics Letters*, Sep 1997.

[22] S.-H. Shim and M. T. Zanni. How to turn your pump-probe instrument into a multidimensional spectrometer: 2D IR and Vis spectroscopies via pulse shaping. *Physical Chemistry Chemical Physics*, 11(5):748, Feb 2009.

[23] K. Matsuo, K. Sakai, Y. Matsushima, T. Fukuyama, and K. Gekko. Optical cell with a temperature-control unit for a vacuum-ultraviolet circular dichroism spectrophotometer. *Analytical Sciences*, 19(1):129–132, Jan 2003.

CHAPTER IV

Photosystem II Studies

In this chapter, I present the experimental data we obtained in our two dimensional electronic spectroscopy experiments on the D1D2-cyt.*b559* reaction center at 77K.. I give the experimental conditions used for this experiment and discuss additional data treatment beyond that covered in Chapter III. I then discuss spectra at selected t_2 values, to illustrate key features present within the data [1]. Finally, I outline a new method for understanding the rich and varied kinetics contained within such a 2D data set. Applying the method to our 2D data, I discuss the kinetic processes we observe.

4.1 2DES of the photosystem II reaction center

4.1.1 Experimental details

We begin with purified protein extracted and concentrated from spinach as detailed in Appendix A. Glycerol is added in a 2:1 (v/v) ratio with sample to form an optical glass at cryogenic temperatures, and the sample is loaded into the sample cell with freshly cleaned windows (see Section 3.4). For the data shown, the sample had an OD of $\sim$0.5 at 680 nm with a thickness of 380 μm.[1] The cryostat is vacuum-

[1]While distortions of 2D spectra do occur for samples with large OD in a fully noncollinear geometry, spectra collected in the pump-probe geometry are less susceptible [2].

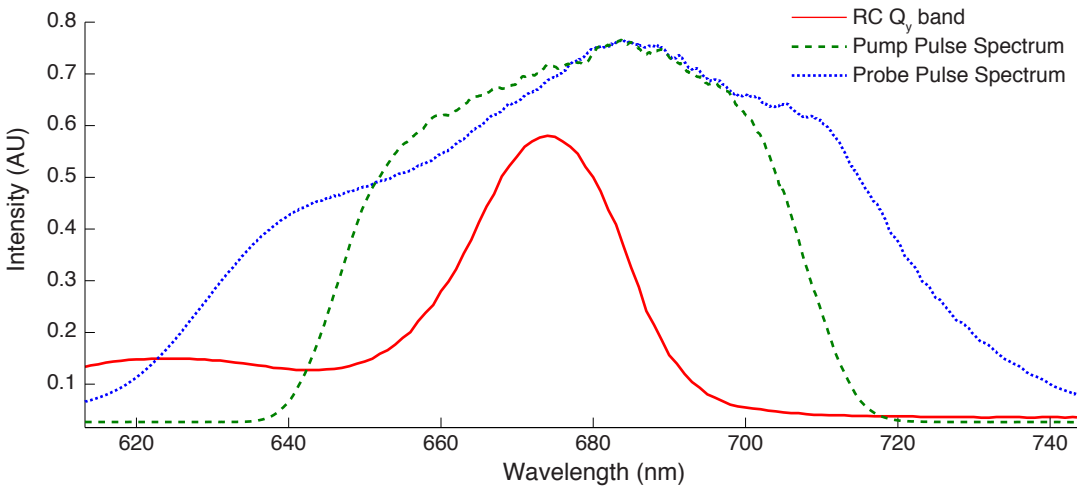

Figure 4.1: Pump and probe spectra used in this experiment overlaid on the room temperature Q_y absorption band of the photosystem II reaction center.

pumped to maintain a pressure of $< 10^{-3}$ mbar to prevent thermal conduction to the cryostat windows, which would cause condensation. Once pressure is achieved, liquid nitrogen is introduced to rapidly cool the sample to 77K. Complete details of the cryostat system may be viewed in [3].

Both the pump and probe NOPAs were tuned to a center wavelength of ∼680 nm, with bandwidths varying from day to day from 40 to 60 nm. The pump and probe pulses used for the data shown in Section 4.1.3 are shown in Figure 4.1, along with the room temperature absorption of the reaction center. Both spectra fully span the Q_y transition. To avoid photodamage of the sample and exciton annihilation effects, each pulse was attenuated to 10 nJ: the pump pulses were attenuated within the Dazzler, and the probe pulse was attenuated with a neutral density filter before the sample. This pulse energy led to a sample bleach of 3±2%, which is sufficiently low to largely avoid exciton annihilation [4]. The spot sizes for the pump and probe at the focus were 530 μm x 440 μm and 300 μm x 190 μm, respectively, and each pulse had a parallel polarization. Using ZAP-SPIDER, the pulses were optimized to ∼28 fs, approximately 1.4 times the transform limit.

We acquired 2DES from $t_2 = 0$ to $t_2 = 150$ps with a roughly logarithmic time steps to observe kinetics across multiple time scales. For each spectrum, we scanned t_1 from 0 to 450 fs in 1 fs steps, and the pump sequence was phase locked at 1500 nm to allow undersampling in the rotating frame [5]. Spectra were collected according to the four-phase cycling and probe chopping method described in Section 3.3.1 in order to reduce scatter contributions. The chopping of the probe reduced the duty cycle of the experiment to 0.5. Each of the four phase values was averaged for approximately 200 ms, resulting in ∼800 laser shots collected. Since each 2D signal requires eight shots, the result is ∼100 complete sets of data, resulting in a high signal-to-noise ratio. Under these conditions, each t_2 spectrum takes approximately 12.5 minutes for collection. After every t_2 scan, the sample would be translated to avoid selectively photodamaging the sample. Bulk absorption measurements before and after the experiment did not reveal any substantial differences. An entire scan over t_2 (from 30-70 time steps) took 20 to 30 hours.

4.1.2 Additional data treatment

In 2D spectroscopy in the pump-probe geometry, the probe beam also acts as the local oscillator (LO) for heterodyne detection. With heterodyne detection, the observed signals in the spectrometer are (ignoring scatter contributions and transient absorption signals):

$$S_{\text{det}} = |E_{\text{S}}|^2 + |E_{\text{LO}}|^2 + E_{\text{S}}E_{\text{LO}}^* e^{i\omega\tau} + c.c. \tag{4.1}$$

where E_{S} is the electric field of the signal, E_{LO} is the electric field of the local oscillator, and τ is the time delay between the heterodyned pulses. We generally neglect $|E_{\text{S}}|^2$ due to the low intensity of the signal, and $|E_{\text{LO}}|^2$ will be subtracted out in the four phase cycling scheme. Therefore, in order to fully recover the signal field, E_{S}, we must

divide out the field of the local oscillator, $|E_{\mathrm{LO}}|$ [6]. In the pump-probe geometry, the heterodyning field passes through the sample and is modified by the sample absorption. To obtain the local field, then, we average over several shots recorded at a large t_1 delay, well after the signal of interest has decayed. We then divide the square root of the recorded intensity for every value of ν_3.

Due to the long data acquisition for an entire t_2 set, we want to have a method for correcting for long term fluctuations of laser amplitude or altering focal volume that could affect the observed kinetics within the 2D set. To do this, we separately record a frequency-resolved transient absorption spectrum that covers the same range of t_2 values.[2] By invoking the projection-slice theorem [6], we can integrate each 2D spectrum along the ν_1 axis and compare the result to the corresponding spectrum of the transient absorption data set. We compare the peak amplitudes of the transient absorption and the integrated 2D spectrum, and use this ratio to apply an overall scaling factor to the 2D spectrum. This method will not affect the lineshapes of any given 2D spectra, but will ensure that peak values match the transient absorption spectrum.

4.1.3 2DES of the D1D2-cyt.*b559* reaction center

In Figure 4.2 I remind the reader of the structure of the pigments in the photosystem II reaction center and introduce the first 2D spectrum of the reaction center at $t_2 = 28$ fs, when pulse overlap effects should be minor. For context, I include the exciton assignments of a recent model by Novoderezhkin et al. [7] (denoted by colored squares that match the color of the pigment in the crystal structure), and impose a grid of the transition energies of the excitons within this model. This model will be discussed in greater detail in Chapter V. Due to the diagonal breadth of the peaks and their close spacing, it is difficult to assign features unambiguously to a single

[2] In the pump-probe geometry with a pulse shaper, the experimental setup does not need to change; we simply program the Dazzler to emit a single pulse instead of two time-delayed pulses.

exciton.

In this data set, there are two primary cross-peaks of interest, denoted as CP 1 below the diagonal, and CP 2 above the diagonal. Their presence in this earliest value of t_2 is notable. The cross-peaks are roughly mirrored along the diagonal, and the presence of an "uphill" cross peak (CP 2) indicates a contribution from a common ground state pathway; there is excitonic coupling between the excitons near 670 nm and 680 nm. The cross peak below the diagonal, CP 1, is stronger than its counterpart, likely indicating the early steps of energy equilibration in the system and downhill energy transfer.

In Figure 4.3 I show a series of 6 2D spectra for increasing values of t_2. Throughout the data set, CP 2 remains relatively constant, further confirming its origin as a common ground state peak. By $t_2 = 215$ fs, CP 1 has substantially grown in magnitude relative to the diagonal peak, and the bluest states along the diagonal have noticeably decayed compared to the 28 fs spectrum. These two observations point to a rapid energy equilibration within the system, with the bluest states quickly transferring their energy to a redder state. These trends of the decaying blue states and the relative growth of the CP 1 continue throughout the data set, until at $t_2 = 100$ ps, the spectrum is quite horizontally elongated. At this point the system has transferred nearly all of the energy into the reddest states, and the spectrum changes little out to $t_2 = 150$ ps.

One of the goals of studying this system is to gain a better understanding of the charge transfer pathway(s) involved in the system. To that end, we would like to compare our data in the context of the two charge transfer pathways proposed by Romero et al. [9] as depicted and discussed in Figure 1.7.

Given the broad features and subtle changes of the spectra even at 77K, we must consider how best to examine the data to either confirm or reject the proposed charge transfer pathways. To better resolve the kinetics within the system, we develop a

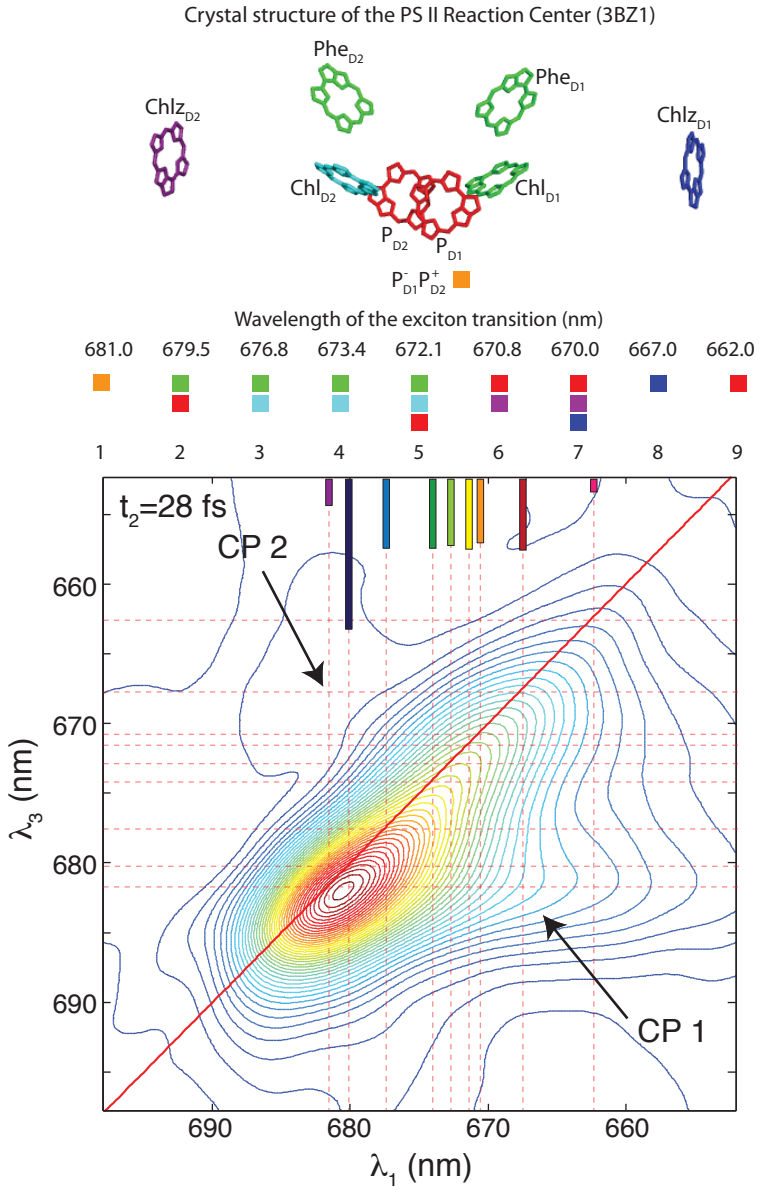

Figure 4.2: A recent crystal structure of the chromophores in the photosystem II reaction center [8] (top), color-coded to match the exciton assignments of Novoderezhkin et al. [7], denoted by boxes underneath the transition wavelength (middle). Underneath, we show 2DES at $t_2 = 28$ fs of photosystem II reaction center at 77K, overlaid with a grid of the exciton transition wavelengths from the Novoderezhkin model. I denote the location of the two primary cross peaks as CP 1 and CP 2.

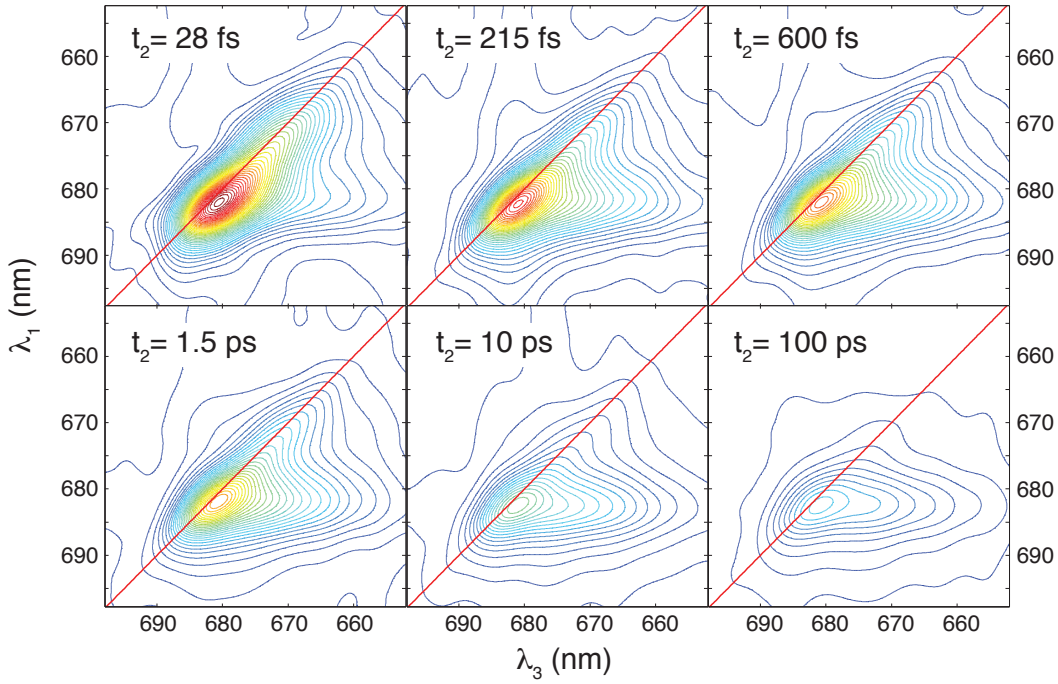

Figure 4.3: The 2DES of the Q_y band of the photosystem II reaction center at 77K for 6 different values of t_2. The spectra have a common color scaling, with the maximum value at the peak of the 28 fs spectrum, and contours every 2.5% of the peak value.

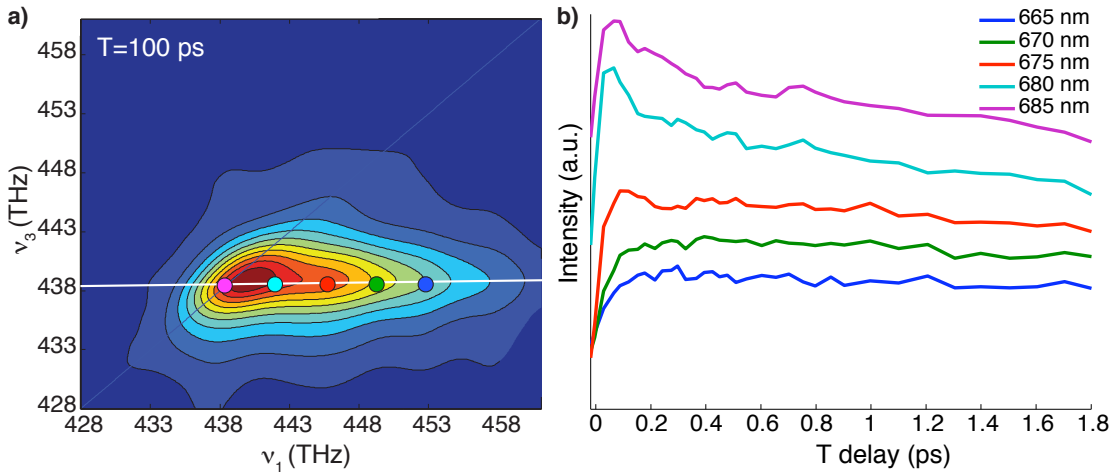

Figure 4.4: **a)** 2DES of the PSII reaction center at $t_2 = 100$ ps. The colored circles indicate the location of the points for which t_2 traces are recorded in **b)**.

method to highlight the spectral signatures of different kinetic processes.

4.2 2D DAS of the D1D2-cyt.*b559* reaction center

With such a rich and complex data set available, one of the challenges can be how to extract the most information from it. Traditionally, global fitting techniques have resulted in "decay associated spectra" to analyze transient absorption data [10]. We seek to extend this technique to two dimensions, while retaining the heterogeneity of time scales observed in the 2D spectra.

When considering the full set of 2D spectrum, we effectively have a three dimensional data set: $S(\nu_1, t_2, \nu_3)$. For any given frequency-frequency point, (ν_1, ν_3), we can recover a one dimensional kinetic trace. As we compare these traces for each frequency-frequency point, we find that the kinetic traces can vary quite strongly in their behavior. As seen in Figure 4.4, when we look at five different points along the final elongated spectrum, we see that the points closest to the diagonal have strong decay features, while the points farthest from the diagonal have initial growth, and a significantly smaller decay.

The challenge for 2D spectra becomes how to fully incorporate this spectral heterogeneity while revealing spectral areas with similar decay features to better understand the physical processes that may be responsible for generating these features. To reveal these areas with similar features, we have developed two dimensional decay associated spectra (2D DAS) [1, 3].

4.2.1 2D DAS construction

In this framework, we independently fit each frequency-frequency trace to a series of four exponential decay components using a least-squares fitting method:

$$f(t_i) = \sum_{k=1}^{4} A_k e^{(-t_i/\tau_k)} \tag{4.2}$$

Four exponentials were chosen based upon previous transient absorption studies [11, 12], and the general quality of the exponential fits. Figure 4.5 shows representative normalized logarithmic traces of five different frequency-frequency points within our data. While four exponents are to expected to have an improved fit, the three component versions generally miss the earliest kinetics. The final τ_k was fixed to be a long-lived component of two nanoseconds, consistent with earlier studies [12]. Since our final time delay was 150 ps, our data is not sufficient to fit such a long-lived component. Changing this value did not significantly affect the other retrieved time constants.

In order to ensure that the fits avoided local minima, the fits were repeated for 10 different sets of initial time constants, each pulled from a Gaussian distribution as shown in Table 4.1. These same 10 sets of initial values were repeated with a negative initial value for the first component, in order to test exponential growth rather than decay on the fastest time component. In all fits, the initial value for the amplitude of any component was chosen to be the maximum amplitude present in the set of 2D

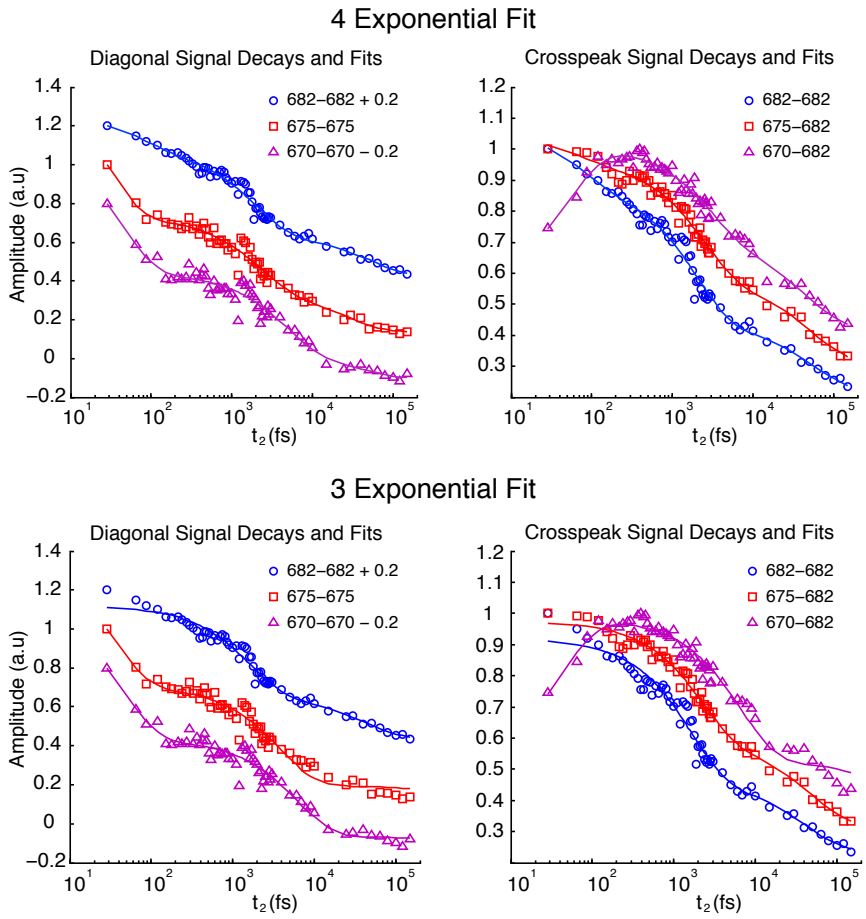

Figure 4.5: Figure showing normalized kinetic traces and retrieved fits of 3 points along the diagonal and along the cross-peak on a logarithmic t_2 scale for fits with both 4 (top row) and 3 (bottom row) exponential components. The diagonal figures (left column) are offset to visually distinguish them, while the cross peak traces (right column) are not. The three exponential fit is generally a poorer match for the earliest kinetics.

Component	Mean Value (ps)	Standard Deviation (ps)
I	0.3	0.1
II	3.5	1
III	35	10

Table 4.1: Initial values used for exponential fits to the data. Note that for the first decay component, the initial value was not allowed to go below 30 fs. The time constant for component IV was not pulled from a random distribution nor used as a fitting parameter, but was fixed at two nanoseconds.

spectra. The best fit from each random draw of initial values was kept.

To construct the 2D DAS, we excluded frequency-frequency points with R^2 values less than 0.9. Figure 4.6 shows the R^2 values retrieved for the series of fits with four exponentials, and indicate that for most spectral regions containing signal, the R^2 value of the fits was well above 0.9. All retrieved lifetimes were then sorted, weighted by their associated amplitude, and clustered into 4 lifetime regions. Care was taken when constructing the lifetime regions to ensure that the lifetime distributions within each region were well-separated and near zero at the boundaries of the region; that the 2D DAS produced were were continuous and well-defined also gives an indication on the quality of the lifetime separations. The 2D DAS consist of two maps, relating the amplitude and lifetime associated with any frequency-frequency point. We also include the amplitude-weighted histogram, showing the distribution of time constants in the component. Fitting each point independently allows 2D DAS to maintain the spectral heterogeneity that is present within our data, while the clustering method allows us to compare and contrast spectral areas with similar decays.

4.2.2 Component I: <400 fs

The first component of the 2D DAS is the sub-400 fs component. In this component, one of striking features of the 2D DAS is the large off-diagonal area (CP 1) with a negative amplitude. The negative amplitude here denotes exponential growth

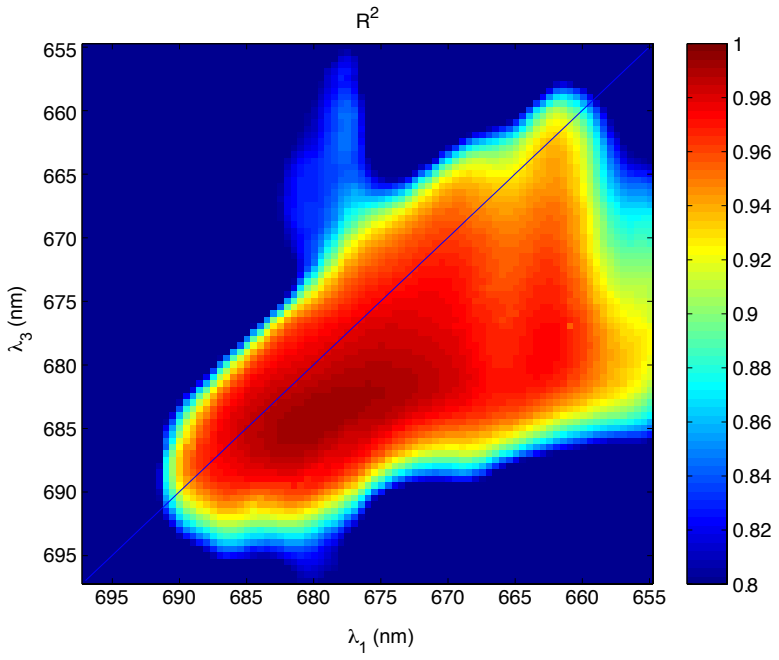

Figure 4.6: R^2 values for the retrieved four-exponential fits to the data. Values above 0.9 indicate regions used to construct 2D DAS [1].

in the cross-peak region, indicating that there is rapid energy equilibration within the D1D2-cyt.*b559* reaction center. Intermediate blue states (excitons 6-8) contribute a 50-100 fs component to the growth of the cross peak, while the bluest states (exciton 9) transfer energy to the reddest states (excitons 1-2) with a ∼200 fs lifetime. Novoderezhkin et al. suggest the rapid formation of a $P^+_{D2}P^-_{D1}$ charge transfer state through sub-400 fs energy transfer [7].

4.2.3 Component II: 1-3 ps

In this component, we examine the 1-3 ps time window. This is the timescale on which Romero et al. [9] propose initial charge separation occurs, with both a $Chl^+_{D1}Pheo^-_{D1}$ state and a $P^+_{D1}Chl^-_{D1}$ (or $(P_{D1}P_{D2})^+Chl^-_{D1}$ in [13]) being formed. In the amplitude map, we note an elongated distribution of amplitudes along the diagonal, revealing the static disorder inherent in this region. In the corresponding region of

the lifetime map, we note that there is a spectral dependence; the reddest states have a lifetime of ~ 3 ps, while the intermediate states near 670 nm have lifetimes closer to two picoseconds. There is also a strong crosspeak visible in the lifetime map with a lifetime of 3 ps. The crosspeak is not strongly observed in the amplitude map. The lifetimes observed are consistent with two charge separation pathways existing, and the spectral heterogeneity of the lifetimes indicates that each pathway has slightly different energetics. Energy disorder within the pigments due to a different protein environment can likely favor one pathway over the other. This will cause some overlap of the energies of the two pathways, leading the two picosecond region seen instead of distinct 1 and 3 ps spectral areas.

4.2.4 Component III: 5-80 ps

The third component in the 2D DAS consists of two distinct lifetime regions. The first is a relatively narrow distribution of lifetimes from 6-8 ps near the highest energy portion of the spectrum and its associated cross-peak. This is interpreted to be energy transfer from the peripheral Chlz pigments. The distance of these pigments from the rest of the reaction center cause them to be well localized and weakly coupled to the rest of the system.

The second region of lifetimes is the 40-60 ps region. These lifetimes are broadly distributed, and there is a slight spectral dependence to the lifetimes; the intermediate states near 670 nm have slightly faster lifetimes than the reddest states. These timescales are consistent with the secondary charge transfer dynamics described in Romero et al. [9], from $\mathrm{Chl}^{+}_{\mathrm{D1}}\mathrm{Pheo}^{-}_{\mathrm{D1}} \rightarrow \mathrm{P}^{+}_{\mathrm{D1}}\mathrm{Pheo}^{-}_{\mathrm{D1}}$ and $\mathrm{P}^{+}_{\mathrm{D1}}\mathrm{Chl}^{-}_{\mathrm{D1}} \rightarrow \mathrm{P}^{+}_{\mathrm{D1}}\mathrm{Pheo}^{-}_{\mathrm{D1}}$.

4.2.5 Component IV: 2 ns

The fourth and final component of the 2D DAS consists of the fixed 2 nanosecond lifetime. The amplitude map is quite similar to the final 2DES where $t_2 > 100$ ps,

and this corresponds roughly to the final charge-separated state. While the lifetime in this component was imposed upon the system, we found that the overall 2D DAS varied little when this component was two nanoseconds or greater.

4.3 Discussion

With the addition of 2DES as a tool for understanding photosystem II, we aim to improve the understanding of this complicated system, particularly in examining the ultrafast energy transfer as well as the charge separation pathways used. Tables 1.1 and 1.2 detail many of the major experiments conducted on photosystem II, and here I summarize what we can add to this body of work.

The first 2D spectrum of photosystem II reaction centers at $t_2 = 28$ fs clearly displays two cross-peaks, one above the diagonal and a second roughly mirrored below the diagonal. The existence of these cross-peaks at such early times provides the first unambiguous evidence of excitonic coupling within the photosystem II reaction center, particularly when observing the persistence of the upper cross peak throughout the t_2 scan. The ability to resolve these cross-peaks is unique to 2D spectroscopy, showing the benefits of this technique.

Within the first time component of the 2D DAS we observed rapid energy equilibration within 100 fs. There has previously been a disagreement about the origin of the rapid decay in the 680-684 nm region. Two pulse photon echo experiments (2PPE) [14] previously assigned this decay to energy equilibration, while hole burning studies [15] have attributed this component to phonon relaxation processes. Our data lends clear support to rapid energy equilibration within the reaction center through the rapid growth of CP 1.

A number of studies have proposed initial charge separation on the order of 1-3 ps [16–18], although the pathways are not yet clear. A low temperature photon echo experiment suggested that Chl_{D1} was the primary electron donor, and not the

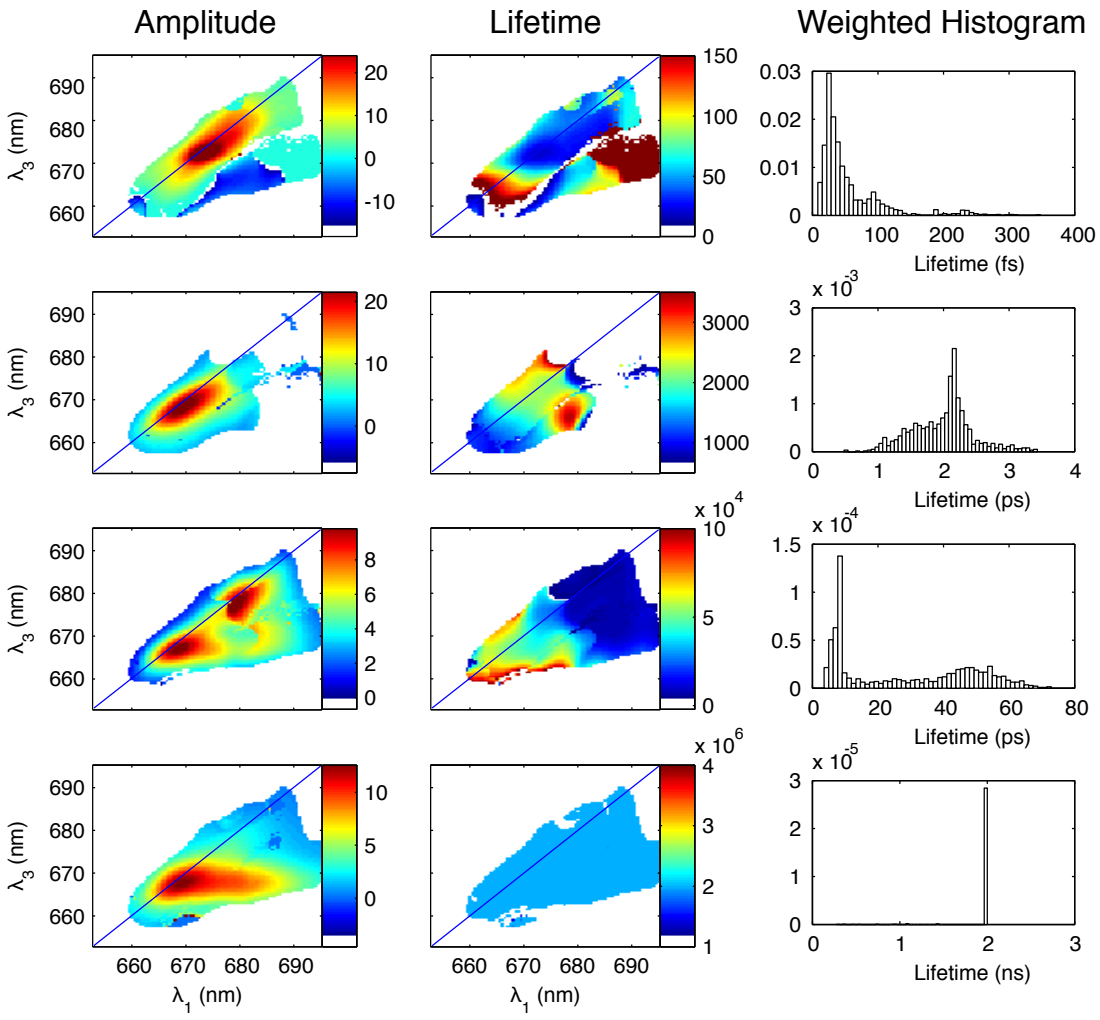

Figure 4.7: 2D DAS as constructed above for the 77 K 2DES of the photosystem II D1D2-cyt.*b559* reaction center, as collected in Section 4.1.3.

P_{D1} [14]. This claim has since been supported by room temperature measurements [19, 20], low temperature experiments [21], site-directed mutations [22], and theory [23, 24]. Romero et al., on the other hand, suggest two competing pathways for charge transfer [9], as detailed above and in Figure 1.7. As shown in Figure 4.7, this component does display spectral heterogeneity with the lifetime and may indicate the spectral signatures of the two pathways. Previous studies have shown features near 680 nm that display different spectral behavior dependent on excitation energy [9, 19].

Component III reveals blue states transferring to a cross-peak with with time scales of 6-8 ps. This is reasonably consistent with transfer from the peripheral Chlz pigments to the center of the complex, where transient absorption studies revealed $\sim$14 ps transfer [11]. The 40-60 ps region was consistent with proposed secondary charge formation [9, 14]. Low temperature transient absorption studies have also suggested the existence of a trap state that is nearly degenerate with the final charge transfer state [9, 11, 12] which could transfer energy on this time scale.

Recently, there has been a large focus on the presence and meaning of electronic coherences in photosynthesis that are resolvable with 2D spectroscopy [25–30]. In particular, a two color photon echo experiment found long-lived coherences in the bacterial reaction center [26]. We note that we cannot definitively observe coherences within our data, and we suggest that this is due to the comparatively weaker coupling in the "special pair" chlorophylls in the reaction center. It is also possible they exist below our noise floor, where we have approximately 2-3% fluctuations in our signal.

Having described the general spectral features and kinetic processes revealed in our 2DES studies of the D1D2-cyt.*b559* reaction center, in Chapter V we simulate 2D spectra based on the Novoderezhkin exciton model for comparison with our data.

References

[1] J. A. Myers, K. L. M. Lewis, F. Fuller, P. Tekavec, and J. P. Ogilvie. Two-dimensional electronic spectroscopy of the D1-D2-cyt b559 photosystem II reaction center complex. *Physical Chemistry Letters*, 2010.

[2] W. Xiong, D. B. Strasfeld, S.-H. Shim, and M. T. Zanni. Automated 2D IR spectrometer mitigates the influence of high optical densities. *Vibrational Spectroscopy*, 50(1):136–142, 2009.

[3] J. A. Myers. *Two-dimensional electronic spectroscopy of the photosystem II D1D2-cyt.*b559 *reaction center complex*. PhD thesis, University of Michigan, 2010.

[4] B. Donovan, L. A. Walker II, C. F. Yocum, and R. J Sension. Transient absorption studies of the primary charge separation in photosystem II. *Journal of Physical Chemistry*, 1996.

[5] S.-H. Shim and M. T. Zanni. How to turn your pump-probe instrument into a multidimensional spectrometer: 2D IR and Vis spectroscopies via pulse shaping. *Physical Chemistry Chemical Physics*, 11(5):748, Feb 2009.

[6] T. Brixner, T. Mančal, I. V. Stiopkin, and G. R. Fleming. Phase-stabilized two-dimensional electronic spectroscopy. *Journal of Chemical Physics*, Sep 2004.

[7] V. I. Novoderezhkin, J. P. Dekker, and R. van Grondelle. Mixing of exciton and charge-transfer states in photosystem II reaction centers: modeling of Stark spectra with modified Redfield theory. *Biophysical Journal*, 93(4):1293–1311, 2007.

[8] A. Guskov, J. Kern, A. Gabdulkhakov, and M. Broser. Cyanobacterial photosystem II at 2.9-Å resolution and the role of quinones, lipids, channels and chloride. *Nature structural & molecular biology*, Jan 2009.

[9] E. Romero, I. H. M. van Stokkum, V. I. Novoderezhkin, J. P. Dekker, and R. van Grondelle. Two different charge separation pathways in photosystem II. *Biochemistry*, 49(20):4300–4307, 2010.

[10] I. H. M. van Stokkum, D. S. Larsen, and R. van Grondelle. Global and target analysis of time-resolved spectra. *Biochimica et Biophysica Acta*, 2004.

[11] H. M. Visser, M. L. Groot, F. van Mourik, I. H. M. van Stokkum, J. P. Dekker, and R. van Grondelle. Subpicosecond transient absorption difference spectroscopy on the reaction center of photosystem II: radical pair formation at 77 K. *The Journal of Physical Chemistry*, Jan 1995.

[12] M. L. Groot, F. van Mourik, C. Eijckelhoff, I. H. M. van Stokkum, J. P. Dekker, and R. van Grondelle. Charge separation in the reaction center of photosystem II studied as a function of temperature. *Proceedings of the National Academy of Sciences*, Jan 1997.

[13] V. I. Novoderezhkin, E. Romero, J. P. Dekker, and R. Grondelle. Multiple charge-separation pathways in photosystem II: Modeling of transient absorption kinetics. *ChemPhysChem*, 12(3):681–688, Feb 2011.

[14] V. Prokhorenko and A. R. Holzwarth. Primary processes and structure of the photosystem II reaction center: A photon echo study. *Journal of Physical Chemistry B*, Jan 2000.

[15] V. Zazubovich, R. Jankowiak, K. Riley, R. Picorel, M. Seibert, and G. J. Small. How fast is excitation energy transfer in the photosystem II reaction center in the low temperature limit? hole burning vs photon echo. *Journal of Physical Chemistry B*, 107(12):2862–2866, 2003.

[16] L. Yoder, A. Cole, and R. J. Sension. Structure and function in the isolated reaction center complex of photosystem II: energy and charge transfer dynamics and mechanism. *Photosynthesis Research*, Jan 2002.

[17] J. P. Dekker and R. van Grondelle. Primary charge separation in photosystem II. *Photosynthesis Research*, 63(3):195–208, 2000.

[18] S. R. Greenfield and M. R. Wasielewski. Excitation energy transfer and charge separation in the isolated photosystem II reaction center. *Photosynthesis Research*, 48(1):83–97, 1996.

[19] A. R. Holzwarth, M. Müller, and M. Reus. Kinetics and mechanism of electron transfer in intact photosystem II and in the isolated reaction center: pheophytin is the primary electron acceptor. *Proceedings of the National Academy of Sciences*, Jan 2006.

[20] M. L. Groot, N. P. Pawlowicz, L. J. G. W. van Wilderen, J. Breton, I. H. M. van Stokkum, and R. van Grondelle. Initial electron donor and acceptor in isolated photosystem II reaction centers identified with femtosecond mid-IR spectroscopy. *Proceedings of the National Academy of Sciences*, Jan 2005.

[21] K. Riley, R. Jankowiak, M. Rätsep, G. J. Small, and V. Zazubovich. Evidence for highly dispersive primary charge separation kinetics and gross heterogeneity in the isolated PS II reaction center of green plants. *Journal of Physical Chemistry B*, 2004.

[22] B. A. Diner, E. Schlodder, P. J. Nixon, W. J. Coleman, F. Rappaport, J. Lavergne, W. F. J. Vermaas, and D. A. Chisholm. Site-directed mutations at D1-His198 and D2-His197 of photosystem II in *Synechocystis* PCC 6803: sites of primary charge separation and cation and triplet stabilization. *Biochemistry*, Jan 2001.

[23] G. Raszewski, W. Saenger, and T. Renger. Theory of optical spectra of photosystem II reaction centers: location of the triplet state and the identity of the primary electron donor. *Biophysical Journal*, Jan 2005.

[24] L. Barter, J. R. Durrant, and D. R. Klug. A quantitative structure-function relationship for the photosystem II reaction center: Supermolecular behavior in natural photosynthesis. *Proceedings of the National Academy of Sciences*, Jan 2003.

[25] R. J. Sension. Biophysics: Quantum path to photosynthesis. *Nature*, Apr 2007.

[26] H. Lee, Y.-C. Cheng, and G. R. Fleming. Coherence dynamics in photosynthesis: protein protection of excitonic coherence. *Science*, 316, Jun 2007.

[27] E. Collini and G. D. Scholes. Electronic and vibrational coherences in resonance energy transfer along MEH-PPV chains at room temperature . *Journal of Physical Chemistry A*, page 090226133546088, Feb 2009.

[28] G. S. Engel, T. Calhoun, E. L. Read, and T. Ahn. Evidence for wavelike energy transfer through quantum coherence in photosynthetic systems. *Nature*, 446, Apr 2007.

[29] G. Panitchayangkoon, D. Hayes, K. A. Fransted, J. R. Caram, E. Harel, J. Wen, R. E. Blankenship, and G. S. Engel. Long-lived quantum coherence in photosynthetic complexes at physiological temperature. *Proceedings of the National Academy of Sciences*, 107(29):12766–12770, Jul 2010.

[30] G. D. Scholes. Quantum-coherent electronic energy transfer: Did nature think of it first? *Journal of Physical Chemistry Letters*, Jan 2010.

CHAPTER V

Theory and Simulations

In this chapter, I present simulations of the 2D electronic spectra of photosystem II, calculated using the software package SPECTRON within modified Redfield theory. I motivate the use of modified Redfield theory for condensed phase systems in an intermediate system-bath coupling regime, and present the equations for calculating the third-order response for such a system in the doorway-window representation. This chapter is not intended to provide a rederivation of these equations, but to outline the formalisms used and to give the expressions needed to calculate the third-order responses. A full treatment is found in the work of Zhang et al. [1].

Next, I examine the model of the photosystem II reaction center from Novoderezhkin et al. [2]. Their model has proven successful for describing a number of different linear spectroscopies, and we compare its predictions for 2DES with the experimental data presented in Chapter IV. We find that the model does not match the lineshapes nor the kinetics of the 2D data so we present an improved version of their model, using newly available crystal structures [3] and adjusting parameters to obtain a better qualitative match to the 2D spectra while maintaining a reasonable match to the linear absorption spectrum.

We also examined the model of Raszewski et al. [4], which differs from a purely modified Redfield approach. The model was not readily adaptable to SPECTRON

and I report our attempts to recreate a similar model in Appendix D. The chapter concludes with a discussion of the simulations presented here, and suggestions about how to further improve them.

5.1 Modified Redfield theory

5.1.1 Motivation

Simulating condensed phase systems often provides computational challenges; we wish to use quantum mechanics to fully describe the system of interest while avoiding calculating costly equations of motion for each degree of freedom. One method for reducing the computational cost is to use a reduced density matrix approach, in which we average over the bath modes and propagate only the density matrix corresponding to the system of interest. This has the advantage of allowing us to treat the bath in a quantum mechanical way, in contrast to mixed quantum-classical methods that treat the bath in a wholly classical manner. In condensed phase systems, and in particular for pigments within a protein environment, the system and the bath are inherently mixed [5, 6].

As 2DES is derived from techniques originally developed for NMR, so too is the theory that we use for modeling 2D spectra. In 1965, A. G. Redfield published "The Theory of Relaxation Processes" [7], designed to model the behavior of a simple quantum system (for instance, a nuclear spin) that interacts weakly with a larger temperature bath. Since the system is assumed to be only weakly coupled to the bath, the system-bath interaction could be treated perturbatively. This approach has proven particularly useful for understanding relaxation within biological systems; here, the couplings between chromophores can be of the same order as the fluctuations of the transition energies, causing Förster theories of energy transfer or Marcus theories of electron transfer to be inappropriate. Redfield theory has previously been

applied to photosystem II [8, 9], but the assumption of strong Coulombic coupling is likely not valid for the system as a whole [2, 4, 10, 11].

In order to extend the theory to bridge the gap between Redfield theory (strong Coulombic coupling) and Förster theory (weak Coulombic coupling), Zhang et al. published a modified version of the Redfield theory to work in the intermediate coupling regime [1]. Within the appropriate limits, it reproduces the rates of both Redfield theory and Förster theory [5], and modified Redfield has since gained prevalence for simulations of photosystem II [2, 4, 10–12] and other photosynthetic systems [13, 14].

5.1.2 Lining up the pieces

As discussed in Chapter II, the third-order polarization that is probed in a third order spectroscopic experiment is a function of the response function:

$$P^{(3)}(t) = \int_0^\infty dt_3 \int_0^\infty dt_2 \int_0^\infty dt_1 S^{(3)}(t_3, t_2, t_1) E_3(t-t_3) E_2(t-t_3-t_2) E_1(t-t_3-t_2-t_1) \quad (5.1)$$

where

$$S^{(3)}(t_3, t_2, t_1) = \left(\frac{i}{\hbar}\right)^3 \theta(t_1)\theta(t_2)\theta(t_3) \sum_{\alpha=1}^{4} [R_\alpha(t_3, t_2, t_1) - R_\alpha^*(t_3, t_2, t_1)] \quad (5.2)$$

and the R_α terms represent different response pathways. It is beyond the scope of this work to fully derive the expressions necessary for calculating the system response; the reader is referred to Mukamel's text [15] for complete details. Within the rest of this section, I will follow the work of Zhang et al. in their paper describing modified Redfield theory in the context of the doorway-window representation [1]. Equations necessary to calculate the response will be given, with additional information in Appendix B, and the reader desiring additional information should refer to the original paper or Shaul Mukamel's review of simulating coherent nonlinear spectroscopies [16]. This is the theory used by the software package SPECTRON to calculate the

simulations seen in later portions of this chapter.

For an intuitive picture of the processes involved within the third-order response, we use the doorway-window representation. In this framework, the state created by the first two field interactions is treated with the "doorway" function. We then allow for field-free evolution during t_2, and finally we apply a "window" function, representing the probe pulse and the emission of the signal. Using projection operator techniques, and within the doorway-window representation of Zhang et al., we can rewrite the third order response function given by Equation 5.2 as:

$$\begin{aligned} S^{(3)}(t_3,t_2,t_1) =& R^{(c)}(t_3,t_2,t_1) + W_0(t_3)D_0(t_1) \\ &+ \sum_{\mu\nu} \int_0^{t_2} dt'' \int_0^{t''} dt' \bar{W}_\mu(t_3, t_2 - t'') G_{\mu\nu}(t'' - t') \bar{D}_\nu(t', t_1) \end{aligned} \tag{5.3}$$

The first term in this equation, $R^{(c)}(t_3,t_2,t_1)$, represents the coherent contribution to the response; this term contains the short time dynamics of the ground state. The second and third terms are expressed in the doorway-window representation. The second, a Raman-type bleaching contribution, is independent of t_2 since the system is in the ground state during t_2. The third term is the hopping term: the doorway function, $\bar{D}_\nu$, creates a population on the νth state, $G_{\mu\nu}$ is the probability for the νth exciton to hop to the μth state during the interval $(t'' - t')$, and the window function, $\bar{W}_\mu$ is the contribution of the μth exciton to the signal. The expressions for computing $R^{(c)}(t_3,t_2,t_1), W_0(t_3), D_0(t_1), \bar{W}_\mu(t_3, t_2 - t''), G_{\mu\nu}(t'' - t')$ and $\bar{D}_\nu(t', t_1)$ are derived by Zhang et al. [1] and given in Appendix B.

5.1.3 The site basis

To calculate the third-order response, we employ the commonly-used Frenkel exciton Hamiltonian. We consider the system to be an aggregate of n pigment molecules (each a two level system) that are coupled to each other and to the bath. The system

Hamiltonian is given by:

$$H = \sum_n \Omega_n \bar{B}_n^\dagger \bar{B}_n + \sum_{m,n}^{m \neq n} J_{m,n} \bar{B}_m^\dagger \bar{B}_n - \sum_{m,n} q_{m,n}^{(c)} \bar{B}_m^\dagger \bar{B}_n + H_{ph} \tag{5.4}$$

where $\bar{B}_n^\dagger$ and $\bar{B}_n$ are excitation creation and annihilation operators for the nth molecule, respectively, Ω_n is the transition energy for site n, and J_{mn} represents the electronic coupling between the m and nth state. Each pair of sites is additionally coupled through the collective bath modes:

$$q_{m,n}^{(c)} \equiv \sum_j m_j \omega_j^2 z_{j,mn} q_j \tag{5.5}$$

where $z_{j,mn}$ is the coupling of the jth phonon to the state given by the operator $\bar{B}_n^\dagger \bar{B}_m$, and q_j, m_j and ω_j represent the respective position, mass, and frequency associated with the jth mode. The bath itself is a collection of harmonic oscillators, given by:

$$H_{ph} = \sum_j \left(\frac{p_j^2}{2m_j} + \frac{m_j \omega_j^2 q_j}{2} \right) \tag{5.6}$$

Here p_j is the momentum of the jth mode.

The system-bath interaction can be best described through a matrix of spectral densities, $C_{mn,kl}(\omega)$, revealing how the fluctuations of the energy difference between sites m and n are correlated with the fluctuations of the energy difference between sites k and l:

$$C_{mn,kl}(\omega) \equiv \frac{i}{2} \int_{-\infty}^{\infty} dt \exp(i\omega t) \langle [q_{mn}^{(c)}(t), q_{kl}^{(c)}(0)] \rangle \tag{5.7}$$

When calculating the third-order response, it is most convenient to convert the

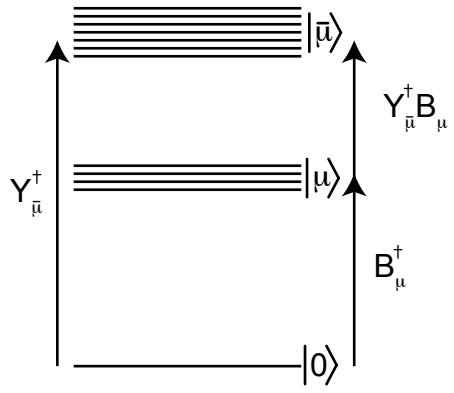

Figure 5.1: A diagram representing the excitonic energy levels used in this theory, as well as the notation used to describe them. Here, μ or ν represents a state on the first excited manifold, and $\bar{\mu}$ or $\bar{\nu}$ represent a state on the second excited manifold. Likewise, $B_\mu^\dagger$ and $Y_{\bar{\mu}}^\dagger$ are the one- and two-exciton creation operators (adapted from [1]).

spectral densities into a series of line-broadening functions, $g(t)$:

$$g_{mn,kl} \equiv \int_{-\infty}^{\infty} \frac{d\omega}{2\pi} \frac{1-\cos(\omega t)}{\omega^2} \coth\left(\frac{\hbar\omega}{2kT}\right) C_{mn,kl}(\omega) + i \int_{-\infty}^{\infty} \frac{d\omega}{2\pi} \frac{\sin(\omega t)-\omega t}{\omega^2} C_{mn,kl}(\omega) \tag{5.8}$$

5.1.4 Transforming into the exciton basis

In order to calculate the third order response for a system, it is helpful to transform the state variables from the site basis (m,n) to the exciton basis (μ,ν). After diagonalizing the site-basis electronic Hamiltonian to transform into the excitonic basis, we obtain a system with well-separated exciton manifolds with one- and two-exciton creation operators as shown in Figure 5.1. The transformation is given by:

$$\begin{aligned} B_\mu^\dagger |0\rangle &= \sum_n \varphi_\mu(n) \bar{B}_n^\dagger |0\rangle , & B_\mu^\dagger \bar{B}_m^\dagger |0\rangle &= 0 \\ Y_{\bar{\mu}}^\dagger |0\rangle &= \sum_{mn} \Psi_{\bar{\mu}}(m,n) \bar{B}_n^\dagger \bar{B}_m^\dagger |0\rangle , & Y_{\bar{\mu}}^\dagger \bar{B}_m^\dagger |0\rangle &= 0 \end{aligned} \tag{5.9}$$

where $B_\mu^\dagger$ ($Y_{\bar{\mu}}^\dagger$) is the one (two) exciton creation operator and $\varphi_\mu(n)$ and $\Psi_{\bar{\mu}}(m,n)$ represent the expansion coefficients.

After transforming the Hamiltonians from the site basis to the excitonic basis, we split the Hamiltonian: $H = H_0 + H_1$. Both Redfield and modified Redfield theories are perturbative in nature. Due to the assumption of weak system-bath coupling, traditional Redfield theory treats the entire system-bath Hamiltonian as the perturbation, H_1. Modified Redfield theory, on the other hand, treats only the off-diagonal elements of the system-bath Hamiltonian as the perturbation, making it more appropriate for the intermediate system-bath coupling regime. H_0 consists of the one- and two-exciton energies as well as the diagonal elements of the system-bath coupling to both the one- and two-exciton states. H_1, the perturbative term, contains the off-diagonal elements:

$$\begin{aligned} H_0 &\equiv \sum_\mu \epsilon_\mu B_\mu^\dagger B_\mu + \sum_{\bar{\mu}} \epsilon_{\bar{\mu}} Y_{\bar{\mu}}^\dagger Y_{\bar{\mu}} + \sum_\mu q_\mu^{(c)} B_\mu^\dagger B_\mu \\ H_1 &\equiv \sum_{\mu\nu}^{\mu\neq\nu} q_{\mu\nu}^{(c)} B_\mu^\dagger B_\nu + \sum_{\bar{\mu}\bar{\nu}}^{\bar{\mu}\neq\bar{\nu}} q_{\bar{\mu}\bar{\nu}}^{(c)} Y_{\bar{\mu}}^\dagger Y_{\bar{\nu}} \end{aligned} \tag{5.10}$$

In the exciton basis, the field interacts with the system through the polarization operator:

$$P = \sum_\mu d_\mu (B_\mu + B_\mu^\dagger) + \sum_{\mu\bar{\mu}} d_{\mu,\bar{\mu}} (Y_{\bar{\mu}}^\dagger B_\mu + B_\mu^\dagger Y_{\bar{\mu}}) \tag{5.11}$$

where d_μ and $d_{\mu,\bar{\mu}}$ represent the appropriate dipole transition strengths. The dipole elements are transformed from the site basis in the same manner as the creation and annihilation operators. Likewise, we transform the spectral density:

$$C_{\bar{m},\bar{n}}(\omega) \equiv \frac{i}{2} \int_{-\infty}^{\infty} dt \exp(i\omega t) \langle [q_{\bar{m}}^{(c)}(t), q_{\bar{n}}^{(c)}(0)] \rangle \tag{5.12}$$

where $\bar{m}$ and $\bar{n}$ can take on any of these state values: $\mu, \bar{\mu}, \mu\nu$, or $\bar{\mu}\bar{\nu}$. In the exciton

basis, and calculating to the lowest order in H_1, the expression for the response function becomes:

$$S^{(3)}(t_3, t_2, t_1) = R^{(c)}(t_3, t_2, t_1) + W_0(t_3)D_0(t_1) + \sum_{\mu\nu} W_\mu(t_3)G_{\mu\nu}(t_2)D_\nu(t_1) \tag{5.13}$$

When taken to the zeroth order in H_1, the doorway and window functions can be computed using the correlation functions, while the correlation functions themselves are evaluated under the second-order cumulant expansion. The Green function ($G_{\mu\nu}(t_2)$) describing exciton-hopping obeys the ordinary master equation under a Markovian approximation (short bath memory):

$$\frac{d}{dt}G_{\mu\nu}(t) = \sum_{\alpha\neq\mu}[K_{\mu\alpha}G_{\alpha\nu}(t) - K_{\alpha\mu}G_{\mu\nu}(t)] \tag{5.14}$$

where $K_{\mu\nu}$ represents the Redfield tensor, and we impose the initial condition that $G_{\mu\nu}(0) = \delta_{\mu\nu}$. The expressions needed to fully calculate Equations 5.13 and 5.14 can be found in Appendix B.

5.2 Novoderezhkin model

In this section, we examine the recent model laid out by Novoderezhkin, et al. [2]. This model is an extension to the original multimer model of photosystem II [17], and their previous work [10] and has been used to simulate a number of different linear spectroscopies (absorption, linear dichroism, circular dichroism, steady-state fluorescence, triplet-minus-singlet, and Stark spectra). This model is an excitonic model; it begins with estimated local site energies and calculates couplings between chromophores using the dipole-dipole approximation using coordinates derived from the crystal structure. In this model, a single charge transfer state is also included as a local state, and is treated in the same manner as any other chromophore, although

with different disorder and coupling to the bath. The Hamiltonian is diagonalized, creating a new, delocalized, exciton basis. Modified Redfield theory dictates the relaxation of these states through their interaction with a bath characterized by a resonant overdamped brownian oscillator spectral density.

5.2.1 System Hamiltonian

The system consists of 9 states: 8 belong to the individual chromophores, and an additional charge transfer state involving the "special pair" chlorophylls: $P^{+}_{D2}P^{-}_{D1}$. This state is treated in a similar manner to chromophoric sites, although with different couplings to the bath and larger disorder. In the original multimer model, all of the chromophores had the same site energy; these energies have been refined through evolutionary algorithms to improve the fit to linear spectroscopy data. With the publication of ever-improving crystal structures for photosystem II [3, 18–20], we are increasingly able to use them as starting points for dipole orientations. In this model, the authors calculated the site couplings using the dipole-dipole approximation:

$$V_{dip-dip} = \frac{\kappa|\mu_1||\mu_2|}{4\pi\epsilon_0\epsilon_r|\mathbf{r}_{12}|^3} \tag{5.15}$$

where $\kappa = \mu_1 \cdot \mu_2 - 3(\mu_1 \cdot \mathbf{r}_{12})(\mu_2 \cdot \mathbf{r}_{12})$. For the dipole orientations, Novoderezhkin et al. use the crystal structure 1IZL [18] as a basis for the site transition dipoles. The authors assumed a Q_y dipole strength of 4.0 Debye for chlorophylls and 3.0 Debye for pheophytins. While the authors are unclear about the exact orientation used, they state, "In our modeling the value of this angle necessary to obtain a good fit is no more than 5-6°." Note that this is rotated from the $N_B - N_D$ orientation in the direction of the N_C atom. For the coordinates from the crystal structure, we used the geometric center of the four central nitrogen atoms for the chlorophylls and pheophytins. Using an angle of 5.5° for each chromophore results in the one-exciton

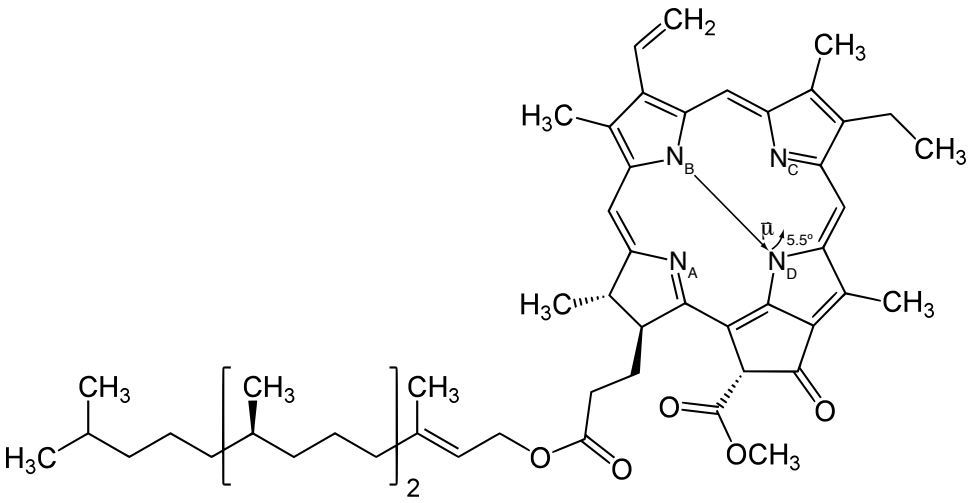

Figure 5.2: A diagram showing the rotation of the chlorophyll *a* transition dipole moment used in the Novoderezhkin model. The central magnesium atom is omitted for clarity. Figure based on [21].

Hamiltonian in Table 5.1.

In this model, we also incorporate independent diagonal disorder. Each term along the diagonal varies independently according to a Gaussian distribution. The chromophoric states each have a FWHM variation of 80 cm^{-1}, while the charge transfer state has a FWHM of 183 cm^{-1}. After diagonalization, this Hamiltonian results in the exciton participation ratios and dipole strengths in Figure 5.3, similar to Figure 6 in [2], indicating that our input Hamiltonians are quite similar. If the diagonalization is given by $|k\rangle = \sum_i c_i^k |i\rangle$, then the participation ratio is given by $\sum_i |c_i^k|^4$. The smaller the participation ratio, the more delocalized the exciton. A participation ratio of 1 would indicate an entirely localized state.

5.2.2 Two-exciton manifold

In calculating the two-exciton manifold, the authors assign the $S_1 \rightarrow S_2$ transition dipole as $0.5\mu_{S_0 \rightarrow S_1}$. Mixed exciton states are simply treated as the sum of the two individual states. However, it is important to note that certain two-exciton states

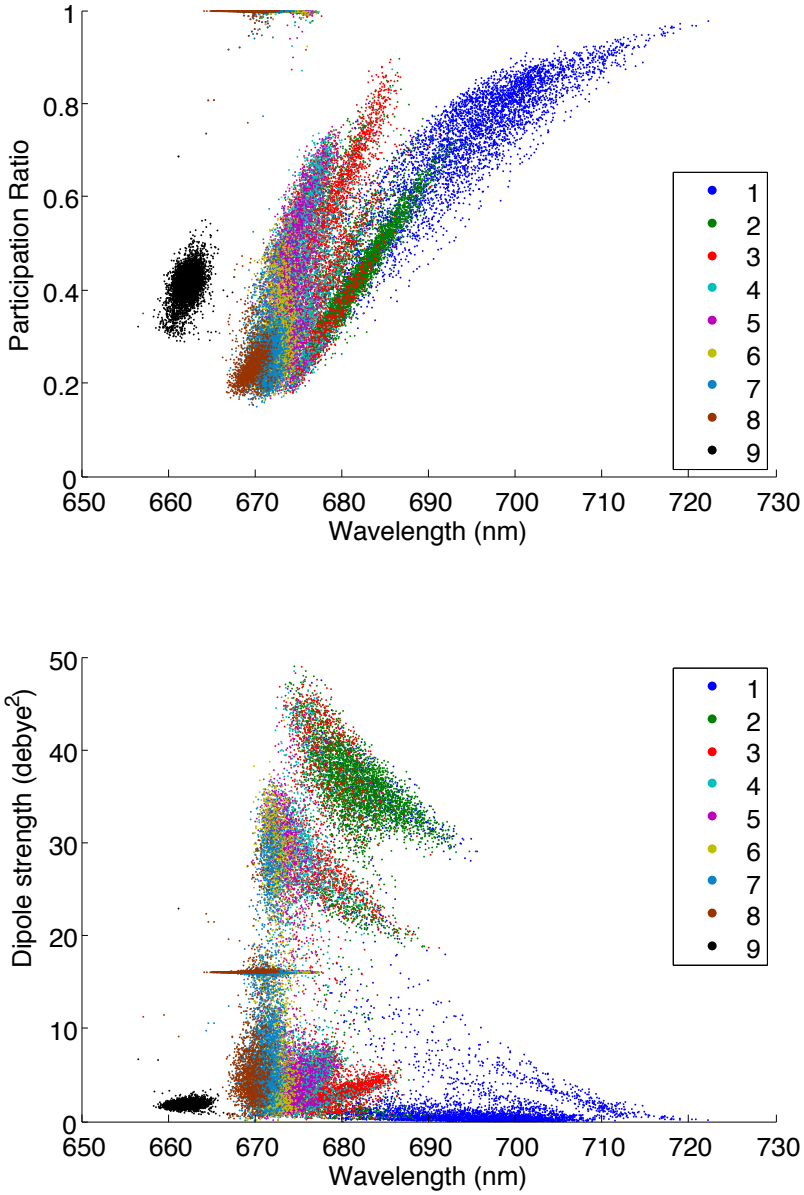

Figure 5.3: The participation ratios and dipole strengths for 5000 instances of disorder of the Novoderezhkin exciton states.

	P_{D1}	P_{D2}	Chl_{D1}	Chl_{D2}	$Pheo_{D1}$	$Pheo_{D2}$	$Chlz_{D1}$	$Chlz_{D2}$	$P^+_{D2}P^-_{D1}$
P_{D1}	15190								
P_{D2}	147.55	15180							
Chl_{D1}	-12.53	-61.88	15000						
Chl_{D2}	-53.42	-5.25	12.23	15130					
$Pheo_{D1}$	-0.03	13.98	55.85	-5.07	15050				
$Pheo_{D2}$	14.67	-4.50	-5.43	51.00	3.47	15060			
$Chlz_{D1}$	-3.18	0.76	-0.69	-0.85	0.93	0.53	15555		
$Chlz_{D2}$	1.25	-3.78	-1.14	0.59	0.66	1.50	-0.08	15485	
$P^+_{D2}P^-_{D1}$	35	35	0	0	0	0	0	0	15120

Table 5.1: The one-exciton Hamiltonian used in the Novoderezhkin model, assuming a dipole rotation of 5.5° from the $N_B - N_D$ axis.

involving the charge transfer state are disallowed; if $P^+_{D2}P^-_{D1}$ is excited, then neither P_{D1} nor P_{D2} can be excited.

5.2.3 System-bath interactions

As described in Equation 5.7, system-bath interactions are characterized through a spectral density, describing the correlation of fluctuations of the energy difference between two pairs of states (mn and kl). In principle, a different spectral density can be used for each m, n, k, l pair; in practice, a single spectral density is often used and applied to all pairs. The Novoderezhkin model uses a unique spectral density: a resonant overdamped brownian oscillator (OBO) incorporating 48 high frequency modes, found in Table 5.2. The modes were determined from low temperature fluorescence line narrowing experiments [22] and are identified by their Huang-Rhys factors, S_j, and their frequency, ω_j. The form of the spectral density they use is given by:

$$C''(\omega) = 2\lambda_0 \frac{\omega\gamma_0}{\omega^2 + \gamma_0^2} + \sum_{j=1,2...} 2\lambda_j \omega_j^2 \frac{\omega\gamma_j}{\left(\omega_j^2 - \omega^2\right)^2 + \omega^2\gamma_j^2} \tag{5.16}$$

where $\lambda_j = S_j\omega_j$ and γ_j is a factor describing the sharpness of the resonance peaks, set at 3 cm^{-1}.

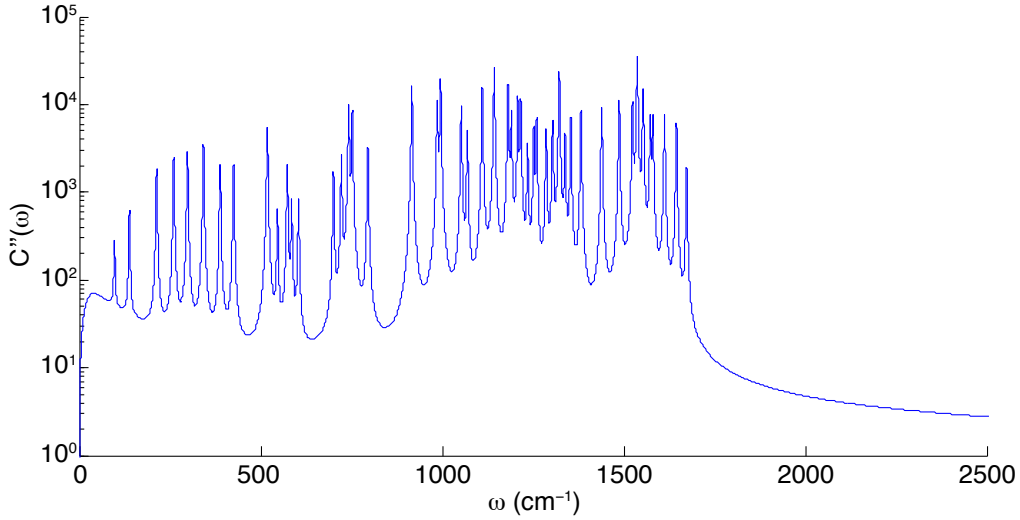

Figure 5.4: The resonant OBO spectral density used in the Novoderezhkin model, viewed on a log scale.

ω_j	S_j	ω_j	S_j	ω_j	S_j	ω_j	S_j
97	0.0371	604	0.0034	1143	0.0303	1354	0.0057
138	0.0455	700	0.0050	1181	0.0179	1382	0.0067
213	0.0606	722	0.0074	1190	0.0084	1439	0.0067
260	0.0539	742	0.0269	1208	0.0121	1487	0.0074
298	0.0488	752	0.0219	1216	0.0111	1524	0.0067
342	0.0438	795	0.0077	1235	0.0034	1537	0.0222
388	0.0202	916	0.0286	1252	0.0051	1553	0.0091
425	0.0168	986	0.0162	1260	0.0064	1573	0.0044
518	0.0303	995	0.0293	1286	0.0047	1580	0.0044
546	0.0030	1052	0.0131	1304	0.0057	1612	0.0044
573	0.0094	1069	0.0064	1322	0.0202	1645	0.0034
585	0.0034	1110	0.0192	1338	0.0037	1673	0.0010

Table 5.2: The 48 high-frequency modes incorporated into the resonant overdamped brownian oscillator as determined by fluorescence line narrowing

	Exc. 1	Exc. 2	Exc. 3	Exc. 4	Exc. 5	Exc. 6	Exc. 7	Exc. 8	Exc. 9
P_{D1}	0.029	0.041	0.040	0.058	0.080	**0.106**	**0.134**	0.050	**0.461**
P_{D2}	0.040	0.094	0.051	0.057	0.067	0.091	**0.123**	0.050	**0.427**
Chl_{D1}	0.088	**0.418**	**0.144**	0.085	0.078	0.067	0.063	0.035	0.021
Chl_{D2}	0.031	0.067	**0.201**	**0.262**	**0.197**	**0.108**	0.070	0.029	0.036
$Pheo_{D1}$	0.047	**0.222**	**0.274**	**0.122**	**0.112**	**0.100**	0.086	0.038	0.000
$Pheo_{D2}$	0.038	0.099	**0.165**	**0.196**	**0.163**	**0.146**	**0.139**	0.053	0.000
$Chlz_{D1}$	0.000	0.000	0.001	0.010	0.029	0.073	**0.193**	**0.694**	0.000
$Chlz_{D2}$	0.000	0.010	0.085	**0.179**	**0.241**	**0.279**	**0.167**	0.038	0.001
$P^+_{D2}P^-_{D1}$	**0.726**	0.048	0.039	0.031	0.033	0.031	0.026	0.013	0.054
λ_{ZPL}	693.7	680.9	677.3	674.9	673.5	672.2	671.1	669.3	662.2
IPR	1.45	2.18	1.87	1.86	1.85	1.83	1.88	1.25	2.41
$\|\boldsymbol{\mu}\|^2$	5.3	28.2	13.4	13.2	13.1	13.3	12.1	13.5	1.9
FWHM	22.9	20.0	21.1	21.8	20.1	19.3	18.4	18.9	22.5

Table 5.3: Squares of the eigenvector elements (any component greater than 10% is in boldface), average participation ratios, dipole strengths, wavelength and FWHM of each individual exciton component.

5.2.4 Results

Linear and 2D absorptive spectra were calculated at 77 K with the SPECTRON software package using the cumulant expansion for Gaussian fluctuations and modified Redfield theory [1, 16, 23, 24]. In order to compare the calculated spectra (which are calculated in evenly-spaced frequency bins) to the experimental data (which are collected in a spectrometer with evenly-spaced wavelength bins), we must multiply the linear spectrum by a factor of $1/\lambda^2$ to compensate. Similarly, we must correct the calculated 2D spectrum by $1/\lambda_3^2$.

The linear spectrum is shown in figure 5.5. We show which chromophores participate with $> 10\%$ probability in which exciton state, along with the average zero-phonon-line wavelength for 5000 different instances of disorder. The contributions from each exciton is shown underneath the overall spectrum. Note that the excitons for each instance of disorder are sorted by the exciton energy after reorganization,

and that on average, this causes mixing of the identities of the states. For instance, as shown in Figure 5.3, there are definitely localized states (from the peripheral chlorophylls), yet it may be anywhere from the 6th through the 8th exciton, causing apparent mixing of the chromophores/excitons upon averaging. The square of the average eigenvectors and other indicators of the excitons are shown in Table 5.3, again with any site contributing more than 10% indicated by boldface type.

In Figure 5.5, we include the original simulation from Novoderezhkin et. al behind ours. They are not perfectly matched. While these should be small effects, the original paper fails to include the exact angle of the dipole used for each chromophore, and does not state whether it considers the magnesium atom or the geometric average of the nitrogens as the chromophore's position for calculating the dipole-dipole coupling. Nor do they specify whether they apply a $1/\lambda^2$ correction as we do. In addition, we also found that the resulting lineshape was highly dependent on disorder, such that we needed to perform twice as many averages as they report in order to obtain convergence. Slight variations in the implementation of the theory may also contribute to the mismatch. Despite the mismatch in the linear spectra, our model does match well the observed exciton transitions, participation ratios and dipole strengths as reported in their paper [2].

The simulated 2D spectra for this model are shown in the center column of Figure 5.6, to compare to the experimental data in the left column. Each column is scaled to the maximum and minimum values throughout the $(\lambda_1, t_2, \lambda_3)$ space, found in all cases within the 28 fs spectrum. In comparing the simulations and the experiment we notice several differences. First we compare the lineshapes in the 2D spectra. In the experimental data, the features are entirely positive, and shows a small, persistent cross-peak above the diagonal indicating excitonic coupling. In the simulations, the cross-peak above the diagonal, while present, is largely obscured by a negative feature. Additionally, in the simulations the cross-peak below the diagonal is more resolved and

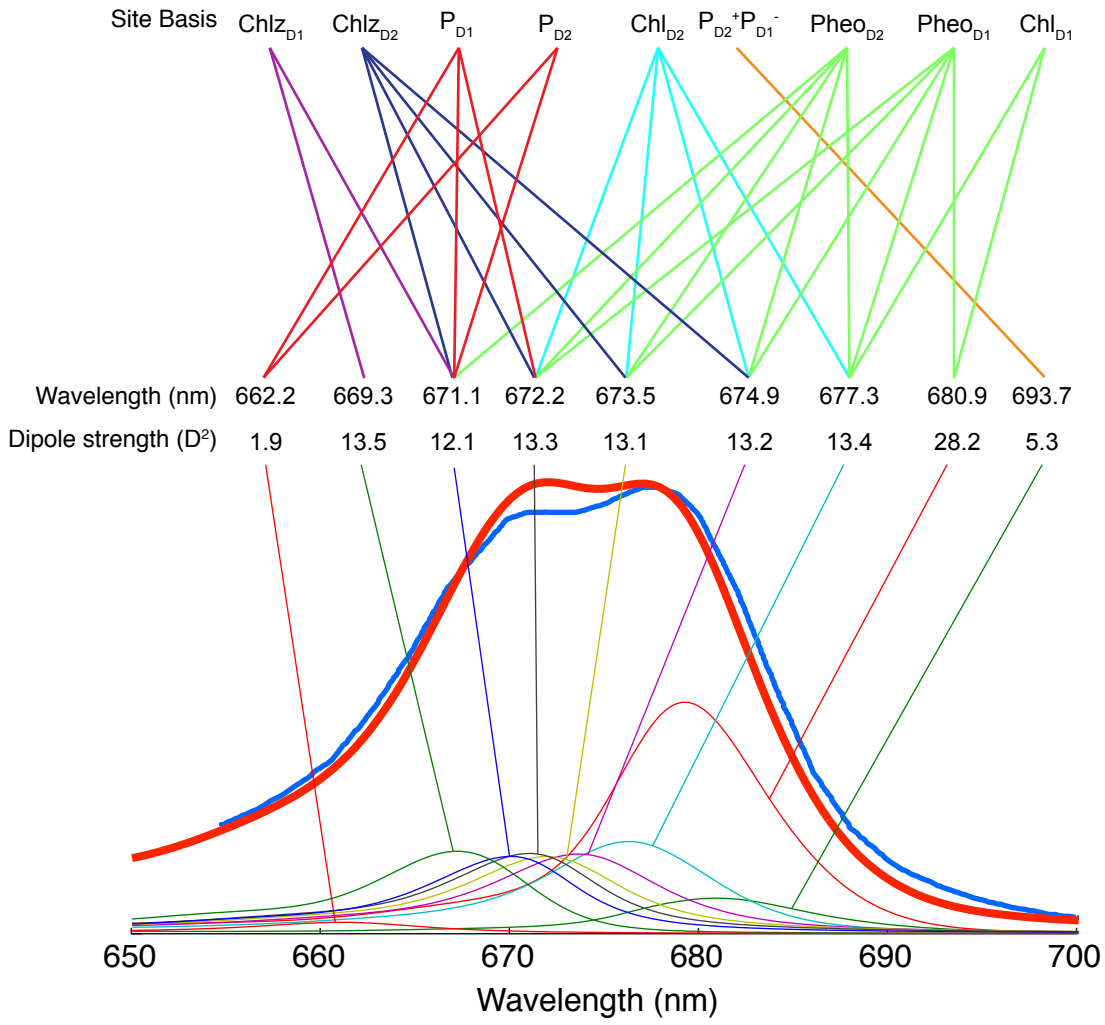

Figure 5.5: Simulated linear absorption spectrum of the PSII reaction center at 77 K (bold red), using the parameters of the original Novoderezhkin model and averaged over 5000 instances of disorder. The linear spectrum of Novoderezhkin et al. [2] was extracted from Figure 6 and is in bold blue behind our simulated spectra. Each chromophore with greater than 10% probability of being involved in a particular exciton has a line connecting it to the exciton. The spectra of individual excitons are shown underneath the sum.

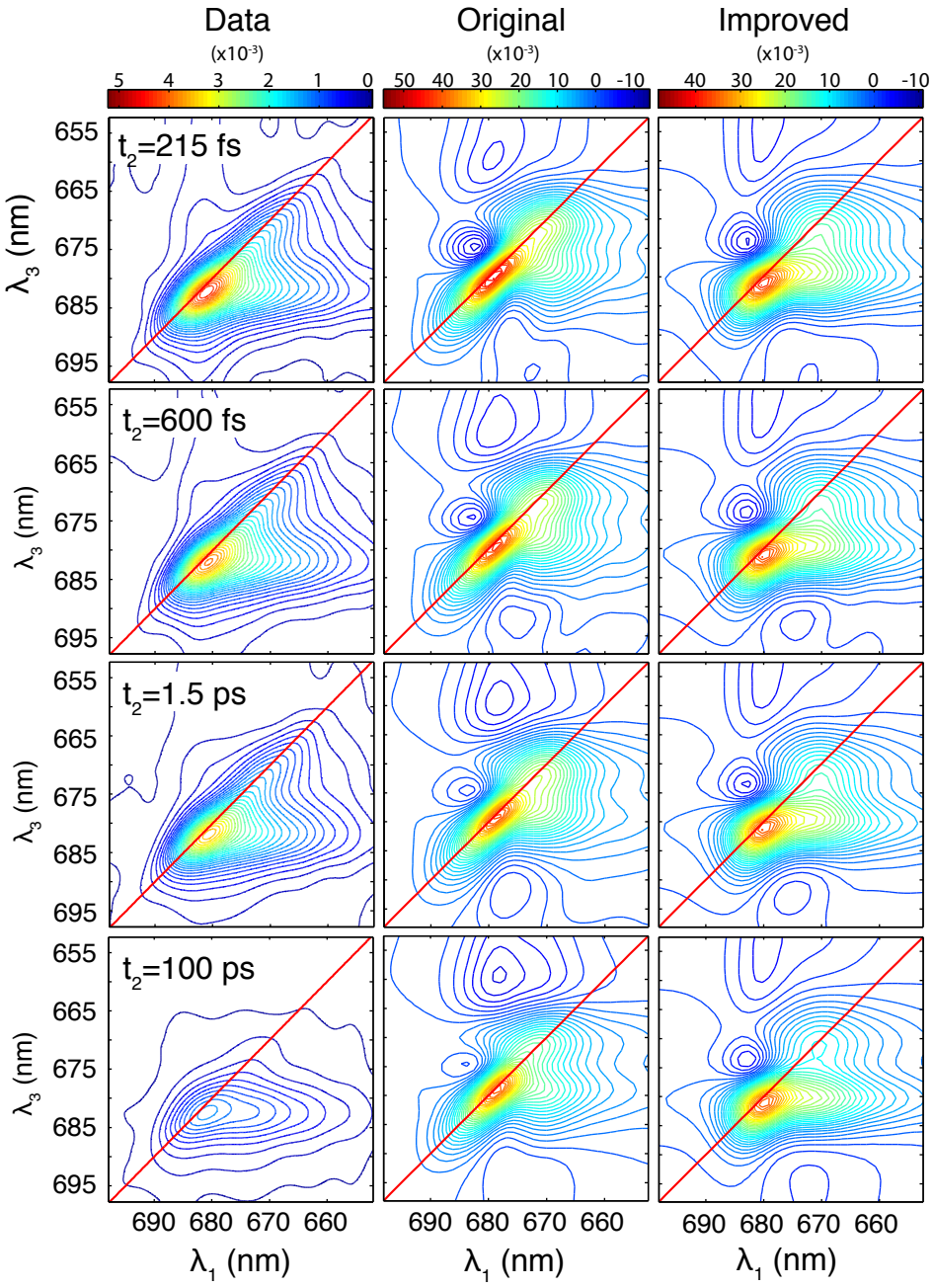

Figure 5.6: Contour plots showing the experimental data (left-most column), the simulations from the original Novoderezhkin model (center column) and the simulations from our improved Novoderezhkin model (right-most column), each averaged over 1500 instances of disorder. Contours are spaced every 2.5% of the maximum value of the 28 fs spectrum. Note that the absolute scale of the data cannot be compared with the absolute scale of the simulations, although the two sets of simulations may be compared to each other.

at a slightly higher energy than is seen in the data. Finally, we note that the overall decay of the spectra is much more significant in the experimental data, both in the overall signal level, and specifically for the highest energy states, which have almost entirely disappeared in the 100 ps data. The lineshapes at the longest decay values are substantially different; the data indicates near-complete relaxation to the lowest energy state and is horizontally elongated, while the simulation maintains diagonal elongation and a significant contribution from the higher energy states remains.

To look at this decay more thoroughly, we compare kinetic traces for different points on the 2D spectra in Figures 5.7 and 5.8. The experimental data have open symbols and solid lines of the 4-exponential fits from previous work [25], while the model here is represented by filled black symbols. The traces for points along the diagonal are offset for clarity. Each point is normalized to the maximum value of the trace. The $\lambda_1 = \lambda_3 = 670$ nm and 675 nm points show that the simulations are missing an initial fast decay component, although the 28 fs data may still contain small pulse-overlap effects and 28 fs simulations may be approaching the regime where the assumptions of well-separated pulses no longer holds. The slopes of the decay in the simulations in the 215 fs to 1.5 ps region are more similar, but the simulations are again missing a long decay component as well. This is not entirely surprising, since the simulations require an optical pulse for an interband transition (i.e., spontaneous emission is excluded). This means that excited state populations will not decay to the ground state at long t_2, and signals will persist. In addition, this model has no mechanism for charge recombination effects. Both of these processes likely occur on the nanosecond timescale. If we assume that there exists a 2 ns second decay component that is "missing" in the simulations, that would add an additional 5% decay in signal at 100 ps. While this would improve the overall match in the kinetic traces, it is clear that the simulations do not accurately match the long-time kinetics of the data.

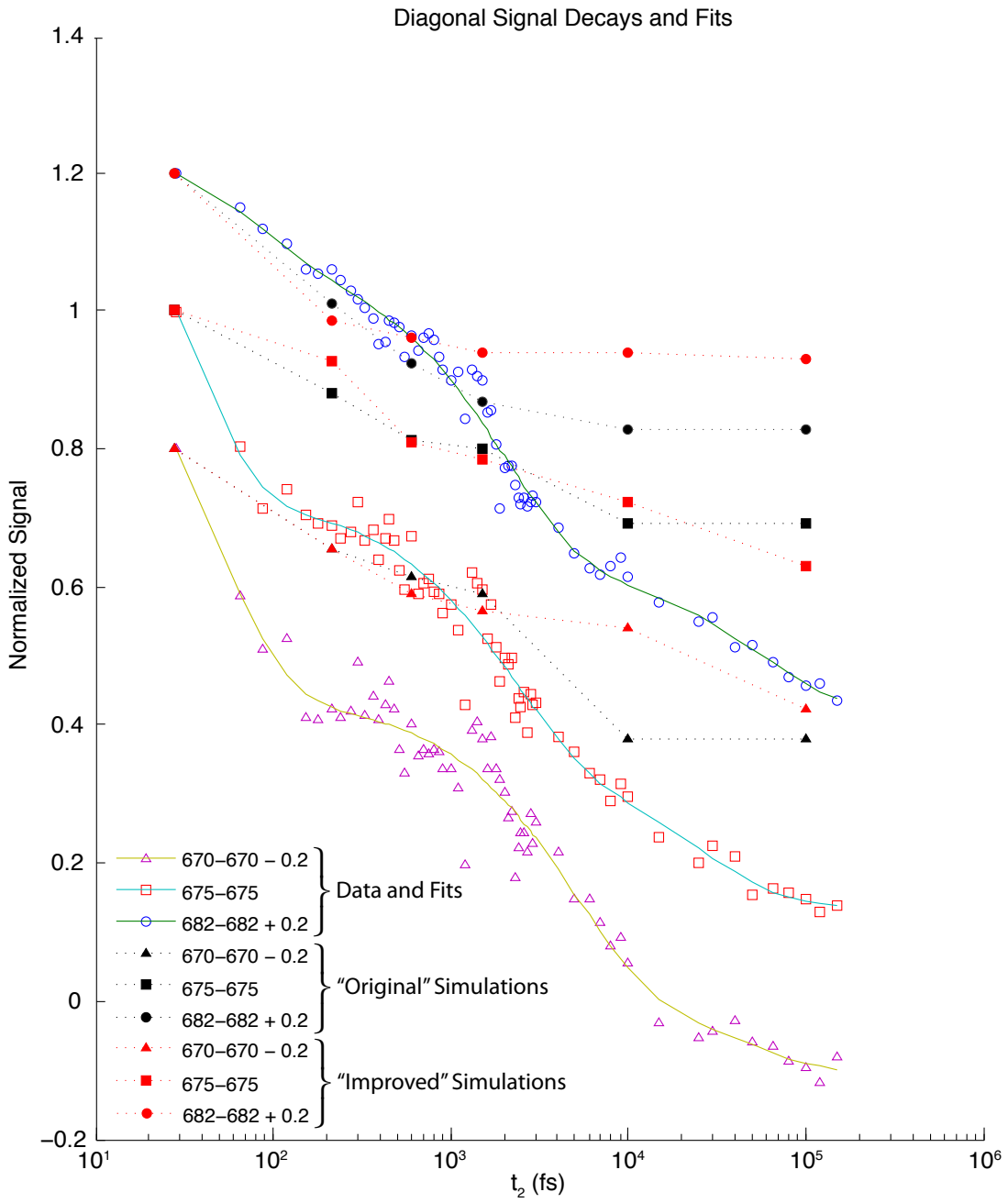

Figure 5.7: Figure showing the amplitude of the absorptive spectrum at 3 different (λ_1, λ_3) points along the diagonal. Each plot is normalized to the value of the spectrum at 28 fs. The different (λ_1, λ_3) values are offset for clarity.

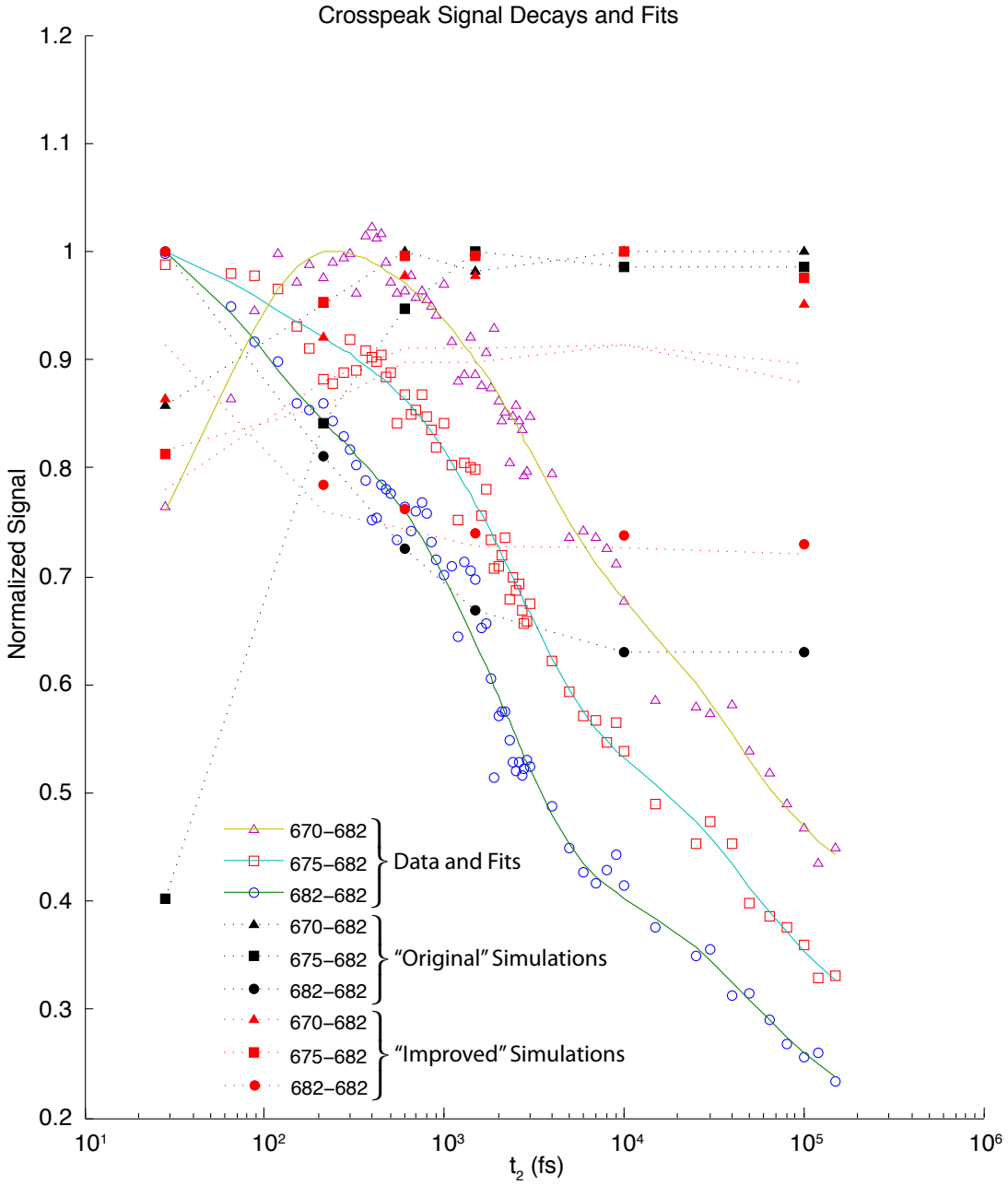

Figure 5.8: Figure showing the amplitude of the absorptive spectrum at 3 different (λ_1, λ_3) points, progressing along the primary cross-peak. Each plot is normalized to the peak value to show the growth of the cross-peak.

5.2.5 Improvements to the original model

Given the general poor match of the original Novoderezhkin model to the 2D data, we would like to find a way to improve the qualitative and quantitative fit of the 2D simulations while retaining the fit of the linear spectra. First, we update the atomic coordinates to take advantage of the recent improvements in the crystal structure [3]. In the newer crystal structures, the P_{D1} and P_{D2} chromophores are closer than in the crystal structures initially used, leading to a substantially higher coupling. This strongly affects the linear spectra. Given that the protein environment is unlikely to have a dielectric constant of 1, and to lower this coupling, we raise the dielectric constant to 1.2, effectively lowering all dipole-dipole couplings between the chromophores.[1] Even with the increased dielectric constant, the P_{D1} and P_{D2} coupling is still larger than in the original model, although the rest of the couplings are still of the same order. We keep the same site energies as the original model.

To optimize the linear and 2D spectra, we also adjust the identity of the CT state to be $(P_{D1}P_{D2})^{+}Chl_{D1}{}^{-}$. Recent experimental data suggests two charge separation pathways, one of which begins with an excitation on three chromophores, P_{D1}, P_{D2}, and Chl_{D1}, which then transitions to a $P^{+}_{D1}Chl^{-}_{D1}$ [28]. To that end, we coupled the CT state to all three of those chromophores with a strength of 35 cm^{-1}. Linear spectra where the CT state is coupled to alternate states are shown alongside the linear spectrum in Figure 5.9. Note that we did not change the construction of the two-exciton manifold.

In order to accomodate faster transfer from the more energetic states, we increase

[1] There has been much discussion about the effect of the protein environment on the couplings of chromophores. Adjusting the dielectric constant is one method, and Scholes and Fleming state that the refractive index n is often taken to be 1.5 within a protein (leading to a dielectric constant of 2.25) [26]. For the Fenna-Matthews-Olson protein (FMO), Renger found that point-dipole approximation worked well with a screening factor of 0.8 [27]. If we consider the screening factor to simply be $1/\epsilon_r$, then this corresponds to a dielectric constant of 1.25, similar to the value we use in the improved model. More complicated procedures that move beyond the point-dipole approximation can also be used to incorporate the effect of the protein [27].

	P_{D1}	P_{D2}	Chl_{D1}	Chl_{D2}	$Pheo_{D1}$	$Pheo_{D2}$	$Chlz_{D1}$	$Chlz_{D2}$	CT
P_{D1}	15190								
P_{D2}	162.2	15180							
Chl_{D1}	-8.66	-56.20	15000						
Chl_{D2}	-59.97	-3.13	11.17	15130					
$Pheo_{D1}$	-1.56	10.99	56.36	-3.38	15050				
$Pheo_{D2}$	9.84	-2.31	-3.29	47.84	1.40	15060			
$Chlz_{D1}$	0.23	0.98	2.20	-0.18	-1.97	-0.11	15555		
$Chlz_{D2}$	0.95	0.51	-0.09	1.88	-0.14	-2.12	0.12	15485	
CT	35	35	35	0	0	0	0	0	15120

Table 5.4: The one-exciton Hamiltonian used in the improved Novoderezhkin model, assuming a dipole rotation of 5.5° from the $N_B - N_D$ axis, and a dielectric constant of 1.2.

the system bath coupling, λ_0, from 70 cm^{-1} to 100 cm^{-1}. Increasing the system-bath coupling broadens the overall spectra, so in order to keep the spectrum width down, we decrease the amount of disorder allowed in each state. The chromophoric states now have a FWHM of 47 cm^{-1} and the CT state has a FWHM of 66 cm^{-1}. As in the original model, the CT state is more strongly coupled to the bath, but by a factor of $\sqrt{2}$ instead of 1.6.

The linear spectrum is shown in Figure 5.9, matching well the linear absorption from the 2007 Novoderezhkin model [2]. The 2D simulations are in the far right column of 5.6, and kinetic traces are shown with filled red symbols in Figures 5.7 and 5.8. The overall lineshapes in the 2D spectra are much more qualitatively similar to the experimental data in the improved model. In particular, we recover the horizontal elongation at long times, and the smaller disorder removes some of the diagonal elongation seen in the original model. However, some of the problems of the original model still exist, primarily seen in the persistent negative feature above the diagonal and the lack of signal decay (both as a whole and particularly in the highest energy states) at large t_2 values.

Looking more closely at the kinetic traces, we notice that our improved model

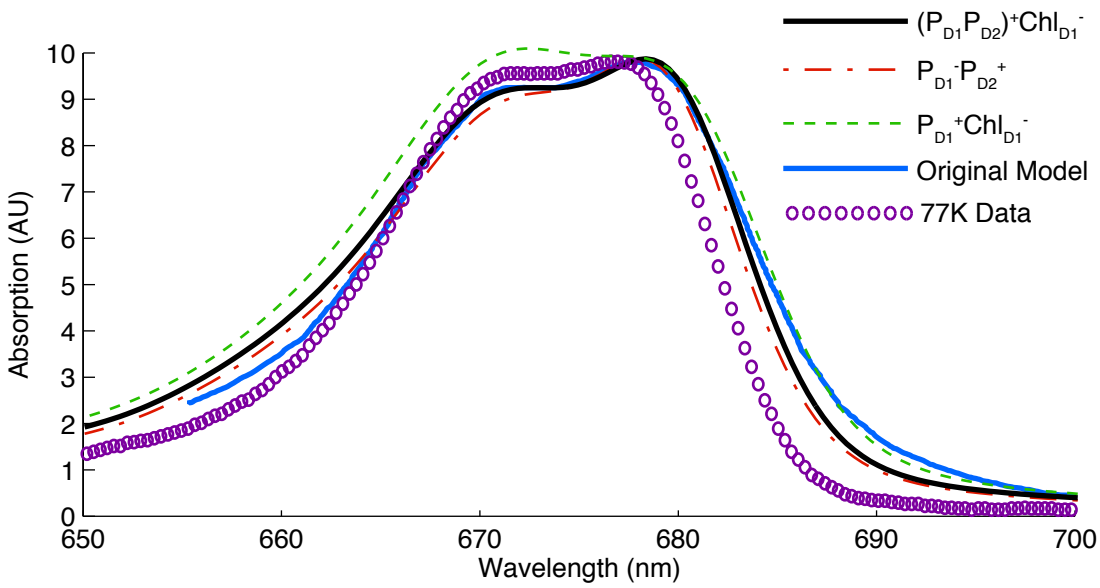

Figure 5.9: Simulated linear absorption spectrum of the PSII reaction center at 77 K, using the parameters of the improved Novoderezhkin model (bold black line) and averaged over 2500 instances of disorder. The dashed lines include the same improved parameters, but differ in which chromophores couple to the CT state, while the bold blue line is the linear spectrum extracted from Figure 6 of [2]. The open symbols represent the experimental absorption spectrum at 77K.

does not provide a better match to the kinetics for all points on the 2D spectrum. The improvements in the 675-675 trace seem to be offset by a poorer match in the 682-682 trace. In the cross-peaks, we see a slight improvement in the 675-682 trace, as this region did not have large signal in the original model.

5.3 Discussion

A variety of models have been used to effectively simulate linear spectroscopies [2, 4, 10, 11] of the PSII reaction center. The models that describe the broadest range of spectroscopic measurements are those of Novoderezhkin and Renger [2, 4]. Our simulations based on the Novoderezhkin model were a poor fit to our observed 2D spectra of the D1D2-cyt.*b559* reaction center. We found that the Novoderezhkin model parameters could be adjusted to maintain good matches to the linear absorption spectra while drastically improving the 2D lineshape.

One of the changes we made in improving the Novoderezhkin model was to use an updated crystal structure to calculate the dipole-dipole couplings. In the newest crystal structure, P_{D1} and P_{D2} are substantially closer than in the crystal structures used in their models. This drastically increases the coupling between these two chromophores, having a large impact on the lineshape of the linear absorption. We chose to reduce the value of this coupling to levels more consistent with other models by adjusting the effective dielectric constant of the protein environment. However, we must consider the possibility that the chromophores are indeed more strongly coupled than previously thought. This could require a large adjustment to the models, requiring new interpretations.

Despite the improvements to the lineshape, kinetic traces of diagonal and cross-peak features are poorly matched to the data. In an earlier paper by the Novoderezhkin group [10], the authors test multiple models of site energies, and while each matched the linear spectra, only one (Model B) was able to adequately describe transient ab-

sorption dynamics in the 0-500 fs range. Their updated model [2], used here as the basis of our 2D simulations, incorporated fits to additional linear spectra but was not tested against transient absorption data. In a new modeling paper that examines transient absorption kinetics [29], Novoderezhkin et al. include some degree of compartmentalization, where transfer to certain states is modeled with Förster theory instead of modified Redfield. This may be needed to obtain a better match to the kinetics. They do not show how well their new model matches linear spectra.

5.4 Future modeling

5.4.1 Incorporating charge transfer states

A key question that remains is how to treat charge transfer states in an intuitive and effective manner. To date the models for the PSII reaction center have included a variety of different charge transfer states in a phenomenological way as required to match the particular set of spectroscopic data being examined (cite Renger, VG, others). A more intuitive approach was recently introduced by Abramavicius et al. [12]. They seek to use a tight-binding model to treat charge transfer in a more intuitive manner. In this model, a molecular excitation involves promoting an electron from the HOMO level to the LUMO level of the molecule, leaving a hole in the HOMO. In this framework, the electron or hole can "hop" to nearby molecules creating a charge transfer state, as seen in Figure 5.10.

This is a promising and powerful avenue for incorporating CT states and exploring the spectral signatures of different charge transfer pathways on 2D data. However, it is a more complicated model, with a number of parameters that will need optimization (see Appendix C.3 for a detailed description of each parameter). While we made some initial efforts towards using this approach to model our data, problems with its implementation in SPECTRON prevented us from exploring it further. A recent

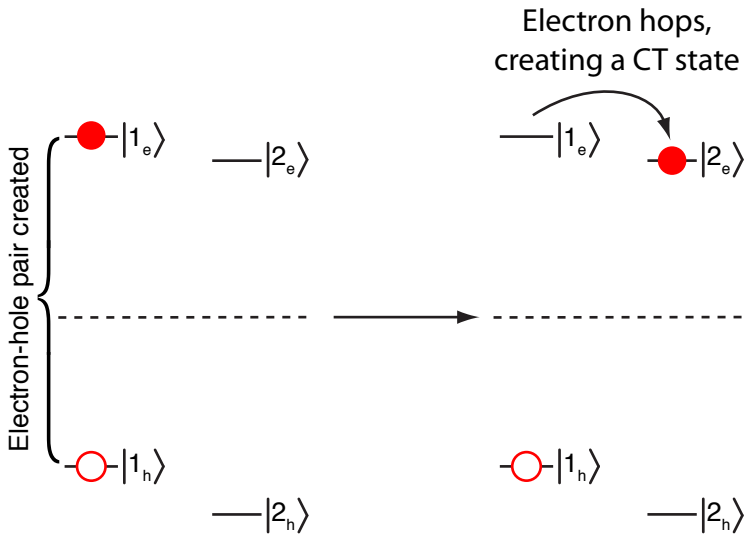

Figure 5.10: Cartoon depicting the creation of a charge transfer state within the CT framework.

update to the SPECTRON code addresses these problems.

5.4.2 Compartmentalization

Another path to improving the match between 2D simulations and data is to compartmentalize the chromophores [4, 11, 29]. This allows for different theories of energy transfer for different parts of the complex. For instance, the peripheral chlorophylls in the reaction center are quite localized compared to the central six chromophores. In this case, generalized Förster theory is likely more appropriate than modified Redfield to describe the transfer of energy from the periphery to the center of the complex. This compartmentalization was first introduced within the context of the Renger model [4, 11].

With compartmentalization, we can maintain the excitonic and delocalized nature of the central pigments, while having more freedom in choosing how energy reaches those pigments, and how it proceeds into charge transfer states. This is likely an important step in creating a better match to the kinetics of the system. While early

changes (femtoseconds to few picoseconds) to the 2D spectra are likely dominated by the steps within the central pigments, on a longer timescale (∼tens of picoseconds) the transfer of energy from the periphery and secondary charge transfer steps will play an important role. In the most recent Novoderezhkin model, they neglect the peripheral chlorophylls, but treat the intermediate charge transfer states using generalized Förster theory, and transfer to the final charge transfer state with standard Förster/Marcus theory [29].

Using different theories to describe the transfer of different components of the complex is not currently implemented in the SPECTRON package. However, it is possible to input rates directly into SPECTRON, so one can use SPECTRON to calculate the modified Redfield rates for the entire complex, and then manually adjust the rates for different compartments using the generalized or standard Förster theory.

References

[1] W. Zhang, T. Meier, V. Chernyak, and S. Mukamel. Exciton-migration and three-pulse femtosecond optical spectroscopies of photosynthetic antenna complexes. *Journal of Chemical Physics*, Jan 1998.

[2] V. I. Novoderezhkin, J. P. Dekker, and R. van Grondelle. Mixing of exciton and charge-transfer states in photosystem II reaction centers: modeling of Stark spectra with modified Redfield theory. *Biophysical Journal*, 93(4):1293–1311, 2007.

[3] Y. Umena, K. Kawakami, J.-R. Shen, and N. Kamiya. Crystal structure of oxygen-evolving photosystem II at a resolution of 1.9Å. *Nature*, 473(7345):55–60, May 2011.

[4] G. Raszewski, B. A. Diner, E. Schlodder, and T. Renger. Spectroscopic properties of reaction center pigments in photosystem II core complexes: revision of the multimer model. *Biophysical Journal*, 95(1):105–119, 2008.

[5] M. Yang and G. R. Fleming. Influence of phonons on exciton transfer dynamics: comparison of the Redfield, Förster, and modified Redfield equations. *Chemical Physics*, 275(1-3):355–372, 2002.

[6] X. Sun and W. H. Miller. Mixed semiclassical-classical approaches to the dynamics of complex molecular systems. *Journal of Chemical Physics*, 106, 1997.

[7] A. G. Redfield. The theory of relaxation processes. *Advances in Magnetic and Optical Resonance*, 1:1–32, Dec 1965.

[8] J. Leegwater, J. R. Durrant, and D. R. Klug. Exciton equilibration induced by phonons: theory and application to PS II reaction centers. *Journal of Physical Chemistry B*, Jan 1997.

[9] T. Renger, J. Voigt, V. May, and O. Kühn. Dissipative exciton motion in a chlorophyll a/b dimer of the light harvesting complex of photosystem II: Simulation of pump-probe spectra. *The Journal of Physical Chemistry*, 100(39):15654–15662, 1996.

[10] V. I. Novoderezhkin, E. G. Andrizhiyevskaya, J. P. Dekker, and R. van Grondelle. Pathways and timescales of primary charge separation in the photosystem II

reaction center as revealed by a simultaneous fit of time-resolved fluorescence and transient absorption. *Biophysical Journal*, 89(3):1464–1481, 2005.

[11] G. Raszewski, W. Saenger, and T. Renger. Theory of optical spectra of photosystem II reaction centers: location of the triplet state and the identity of the primary electron donor. *Biophysical Journal*, Jan 2005.

[12] D. Abramavicius and S. Mukamel. Energy-transfer and charge-separation pathways in the reaction center of photosystem II revealed by coherent two-dimensional optical spectroscopy. *Journal of Chemical Physics*, Jan 2010.

[13] T. Brixner, J. Stenger, H. M. Vaswani, M. Cho, R. E. Blankenship, and G. R. Fleming. Two-dimensional spectroscopy of electronic couplings in photosynthesis. *Nature*, 434(7033):625–628, Mar 2005.

[14] E. L. Read, G. S. Schlau-Cohen, G. S. Engel, T. Georgiou, M. Z. Papiz, and G. R. Fleming. Pigment organization and energy level structure in light-harvesting complex 4: Insights from two-dimensional electronic spectroscopy. *Journal of Physical Chemistry B*, 113(18):6495–6504, Apr 2009.

[15] S. Mukamel. *Principles of Nonlinear Optical Spectroscopy*. Oxford University Press, 1995.

[16] S. Mukamel and D. Abramavicius. Many-body approaches for simulating coherent nonlinear spectroscopies of electronic and vibrational excitons. *Chemical Reviews*, Jan 2004.

[17] J. R. Durrant, D. R. Klug, S. Kwa, R. van Grondelle, G. Porter, and J. P. Dekker. A multimer model for P680, the primary electron donor of photosystem II. *Proceedings of the National Academy of Sciences*, Jan 1995.

[18] N. Kamiya and J. Shen. Crystal structure of oxygen-evolving photosystem II from *thermosynechococcus vulcanus* at 3.7-Å resolution. *Proceedings of the National Academy of Sciences*, Jan 2003.

[19] B. Loll, J. Kern, W. Saenger, A. Zouni, and J. Biesiadka. Towards complete cofactor arrangement in the 3.0 Å resolution structure of photosystem II. *Nature*, Jan 2005.

[20] A. Guskov, J. Kern, A. Gabdulkhakov, and M. Broser. Cyanobacterial photosystem II at 2.9-Å resolution and the role of quinones, lipids, channels and chloride. *Nature structural & molecular biology*, Jan 2009.

[21] Public domain. Chlorophyll *a* structure. Retrieved on 5 September 2011 from `http://en.wikipedia.org/wiki/File:Chlorophyll_a_structure.svg`.

[22] E. Peterman and H. van Amerongen. The nature of the excited state of the reaction center of photosystem II of green plants: a high-resolution fluorescence spectroscopy study. *Proceedings of the National Academy of Sciences*, 95, May 1998.

[23] D. Abramavicius, L. Valkunas, and S. Mukamel. Transport and correlated fluctuations in the nonlinear optical response of excitons. *Europhysics Letters*, Jan 2007.

[24] W. Zhuang, D. Abramavicius, T. Hayashi, and S. Mukamel. Simulation protocols for coherent femtosecond vibrational spectra of peptides. *Journal of Physical Chemistry B*, Jan 2006.

[25] J. A. Myers, K. L. M. Lewis, F. Fuller, P. Tekavec, and J. P. Ogilvie. Two-dimensional electronic spectroscopy of the D1-D2-cyt b559 photosystem II reaction center complex. *Physical Chemistry Letters*, 2010.

[26] G. D. Scholes and G. R. Fleming. On the mechanism of light harvesting in photosynthetic purple bacteria: B800 to B850 energy transfer. *Journal of Physical Chemistry B*, Feb 2000.

[27] T. Renger. Theory of excitation energy transfer: from structure to function. *Photosynthesis Research*, 102(2):471–485, 2009.

[28] E. Romero, I. H. M. van Stokkum, V. I. Novoderezhkin, J. P. Dekker, and R. van Grondelle. Two different charge separation pathways in photosystem II. *Biochemistry*, 49(20):4300–4307, 2010.

[29] V. I. Novoderezhkin, E. Romero, J. P. Dekker, and R. Grondelle. Multiple charge-separation pathways in photosystem II: Modeling of transient absorption kinetics. *ChemPhysChem*, 12(3):681–688, Feb 2011.

CHAPTER VI

Conclusions

6.1 Summary

As the first group to perform two dimensional electronic spectroscopy with visible light in the pump-probe geometry [1], we developed a number of technical innovations for this technique. We demonstrated the separation of rephasing and non-rephasing spectra [1], the use of a continuum probe for broadband detection and observation of vibrational wavepacket dynamics [2], quantified the effects of pulse chirp on 2D spectra [3] as well as how to correct them [4]. We developed a strategy for scatter removal using a combination of phase cycling and pulse chopping [5]. In an alternate geometry, we demonstrated two color 2DES to observe energy transfer with dyes attached to a DNA construct [6].

We performed the first 2DES of the photosystem II reaction center at 77K and created a new technique for extracting information from such a rich data set [7]. The data has provided a number of insights into this complicated system. By observing cross-peaks in the early t_2 2D spectra of the isolated reaction center we have unambiguously observed excitonic coupling. We observed the rapid ($\sim$50-150 fs) growth of a cross peak in the 2D spectrum, indicating rapid energy equilibration in this excitonic system. In the 1-3 ps window where primary charge separation events are thought to occur, we observe a spectral heterogeneity of lifetimes: a faster component

from 1-2 ps, and a slower 3 ps component, lending support to the work of Romero et. al [8] that suggests two charge separation pathways. The 40-60 ps components also support this time scale for secondary charge separation.

We have tested the excitonic model of Novoderezhkin against our 2D spectroscopic data. While the Novoderezhkin model has fared well in a variety of linear spectroscopies [9], it poorly matched both the lineshapes and kinetics found in our data. With the 2D data as a guide, we created an improved model that more closely matched the 2D lineshapes while maintaining the shape of the linear absorption. The kinetics found in our data have proven difficult to simulate, and compartmentalization of the rates may provide a better path forward here. The tight-binding model of Abramavicius et al. [10] gives a more intuitive description of charge transfer, but the additional parameters in the model require optimization. Additional experimental measurements that can better distinguish energy and charge separation processes are also needed and will be enabled by the methods developed in this thesis.

6.2 Future directions

6.2.1 Continuum studies

With 2DES in the pump-probe geometry, it is straightforward to use alternate probe beams, allowing access different regions of the 2D spectra. With a NOPA probe, one can tune the NOPA to probe the region along the diagonal, as in our original 2D studies of PSII. Alternatively, one can tune the NOPA to regions far from the diagonal, to probe specific cross peaks or to observe energy transfer spanning a wide range of wavelength, as in FRET [6]. One can also choose not to use a NOPA beam at all, but to use a continuum pulse, allowing access to the widest range of wavelengths in a single experiment [2].

When we consider the PSII reaction center specifically, we note that there are

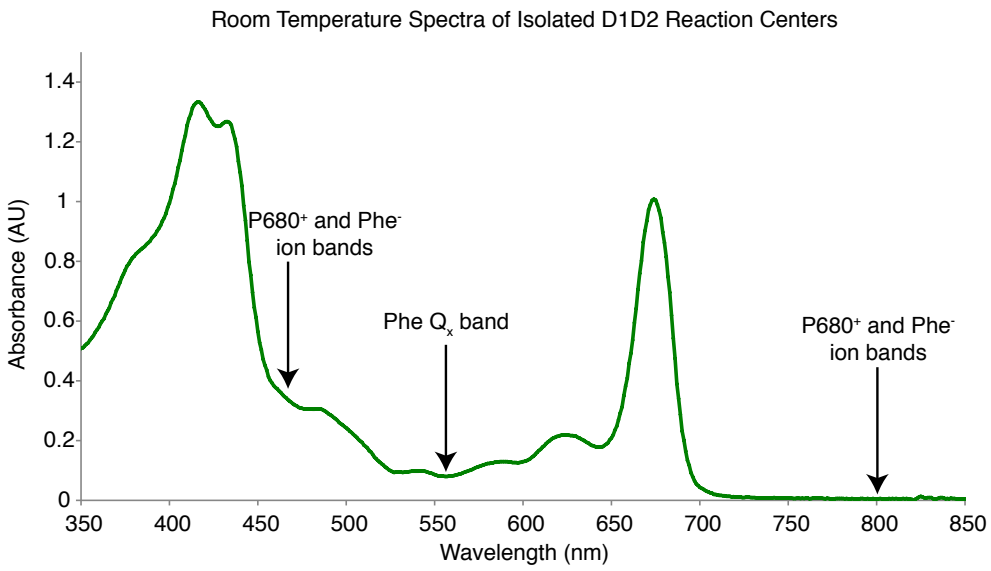

Figure 6.1: Room temperature spectra of the complexes used in the experiments in Section 4.3. Locations of the ion bands and the pheophytin Q_x band are shown for reference.

areas of the absorption spectra that would have clearer signatures of charge transfer events. In Figure 6.1, we see the locations of the P680 and pheophytin ion bands. While they are not present in the room temperature spectra, upon a charge transfer event with $P680^+$ or Phe^-, we should see the growth of cross-peaks in these regions.

6.2.2 Additional future directions

There are many future directions available for obtaining a better understanding of the energy and charge transfer processes involved in the photosystem II reaction center. Experimentally, we can chemically alter the D1D2 reaction center by pre-reducing the pheophytin, effectively blocking some charge transfer pathways. Modeling the reduced data will provide yet more constraints on the models. For preliminary work on the reduced system, see Appendix E.

Beyond studying photosystem II from higher plants, the cyanobacterium *Acaryochloris marina* has been discovered to have chlorophyll *d* as the primary pigment

[11]. Despite the predominance of chlorophyll *d*, each photosystem appears to have one (or more) chlorophyll *a* molecules [12], although it has not yet been determined if chlorophyll *a* plays a critical role in the photochemistry. Performing 2DES on a purifed D1D2 reaction center from *A. marina* may give additional insight on the roles of the different chlorophylls within the system, and deeper understanding on system requirements for generating redox potentials capable of splitting water. An equivalent D1D2 preparation has not yet been purified from *A. marina*, although PSII complexes and smaller PSII particles containing ∼20 chlorophylls have been reported [13, 14]. We report on our attempts to purify PSII from *A. marina* in Appendix A.

There are many paths forward for improving the modeling as well. In order to improve the match of the models to the kinetics, it may also be necessary to compartmentalize the system; modified Redfield theory may not be appropriate for all energy transfer pathways within the reaction center. Finally, we desire a more intuitive model for incorporating charge transfer states in the model which may involve a tight-binding electron-hole model recently developed.

In this dissertation I have given a detailed description of my work with the reaction center of photosystem II, both through experiments and modeling. I am proud to have worked on this experiment from the ground up, and to have participated in every aspect of its development: building the experimental apparatus, purifying the protein sample, taking and analyzing the 2D data, and finally attempting to model the data to better understand how system parameters affect the 2D spectra. I hope the work presented here has made the complicated system of the photosystem II reaction center a little clearer, and will provide the groundwork for future experiments and modeling.

References

[1] J. A. Myers, K. L. M. Lewis, P. F. Tekavec, and J. P. Ogilvie. Two-color two-dimensional Fourier transform electronic spectroscopy with a pulse-shaper. *Optics Express*, 16(22):17420, Oct 2008.

[2] P. F. Tekavec, J. A. Myers, K. L. M. Lewis, and J. P. Ogilvie. Two-dimensional electronic spectroscopy with a continuum probe. *Optics Letters*, 34(9):1390–1392, 2009.

[3] P. F. Tekavec, J. A. Myers, K. L. M. Lewis, F. D. Fuller, and J. P. Ogilvie. Effects of chirp on two-dimensional Fourier transform electronic spectra. *Optics Express*, 2010.

[4] P. F. Tekavec, K. L. M. Lewis, F. D. Fuller, J. A. Myers, and J. P. Ogilvie. Toward broad bandwidth 2-D electronic spectroscopy: Correction of chirp from a continuum probe. *IEEE Journal of Selected Topics in Quantum Electronics*, PP(99):1–8, 2011.

[5] K. L. M. Lewis, J. A. Myers, F. Fuller, P. F. Tekavec, and J. P. Ogilvie. Strategies for scatter removal in two-dimensional electronic spectroscopy in the pump-probe geometry. In A. Wobst, editor, *Ultrafast Phenomena XVII*, 2011.

[6] K. L. M. Lewis, J. A. Myers, P. F. Tekavec, and J. P. Ogilvie. Two-color two-dimensional Fourier transform spectroscopy of energy transfer. In P. Corkum, S. De Silvestri, K. A. Nelson, E. Riedle, and R. W. Schoenlein, editors, *Ultrafast Phenomena XVI*, 2009.

[7] J. A. Myers, K. L. M. Lewis, F. Fuller, P. Tekavec, and J. P. Ogilvie. Two-dimensional electronic spectroscopy of the D1-D2-cyt b559 photosystem II reaction center complex. *Physical Chemistry Letters*, 2010.

[8] E. Romero, I. H. M. van Stokkum, V. I. Novoderezhkin, J. P. Dekker, and R. van Grondelle. Two different charge separation pathways in photosystem II. *Biochemistry*, 49(20):4300–4307, 2010.

[9] V. I. Novoderezhkin, J. P. Dekker, and R. van Grondelle. Mixing of exciton and charge-transfer states in photosystem II reaction centers: modeling of Stark spectra with modified Redfield theory. *Biophysical Journal*, 93(4):1293–1311, 2007.

[10] D. Abramavicius and S. Mukamel. Energy-transfer and charge-separation pathways in the reaction center of photosystem II revealed by coherent two-dimensional optical spectroscopy. *Journal of Chemical Physics*, Jan 2010.

[11] H. Miyashita, H. Ikemoto, N. Kurano, K. Adachi, M. Chihara, and S. Miyachi. Chlorophyll *d* as a major pigment. *Nature*, 383, Oct 1996.

[12] S. Ohashi, H. Miyashita, N. Okada, T. Iemura, T. Watanabe, and M. Kobayashi. Unique photosystems in *Acaryochloris marina*. *Photosynthesis Research*, 98(1):141–149, 2008.

[13] T. Tomo, T. Okubo, S. Akimoto, M. Yokono, H. Miyashita, T. Tsuchiya, T. Noguchi, and M. Mimuro. Identification of the special pair of photosystem ii in a chlorophyll *d*-dominated cyanobacterium. *Proceedings of the National Academy of Sciences*, 104, Apr 2007.

[14] M. Chen, A. Telfer, S. Lin, A. Pascal, A. W. D. Larkum, J. Barber, and R. E. Blankenship. The nature of the photosystem II reaction centre in the chlorophyll *d*-containing prokaryote, *Acaryochloris marina*. *Photochemical & Photobiological Sciences*, 4(12):1060–1064, Nov 2005.

APPENDICES

APPENDIX A

Photosystem II Purification

This appendix details the preparation of the samples used in this dissertation. This work was performed in the lab of Professor Charles Yocum, with his help and guidance. The D1-D2 preparation from spinach is well-characterized and most closely follows the procedure from van Leeuwen et al. [12]. A protocol to recover an analogous complex from *Acaryochloris marina* is still in progress; the techniques described here record our purification attempts and plan, following protocols similar to [13] and [3]. Note that both of these protocols will be refined in future dissertations from our group.

Packing the column

Both purification methods require the use of an anion exchange column. When properly cared for and stored, these columns can be used repeatedly, so these steps usually only need to be done when switching the desired bead medium. We begin with an empty 10 mL glass column from Pharmacia Biotech, and a bottle of bead medium in aqueous ethanol (Q-Sepharose for the spinach preparation and DEAE-Toyopearl for *A. marina*). Soak the column filters well in doubly-distilled water (ddH_2O) prior to assembling the column. At the same time, thoroughly mix the beads in their

container and measure out 15 mL of the resulting bead mixture. Let the beads settle to ensure that you have a sufficient volume (∼10 mL) of beads. Place a wet filter on the bottom assembly, and screw this onto the column. Dilute your beads with distilled water and thoroughly mix.

Remove the cap from the bottom assembly, and pour the dilute medium into the column. As the beads settle, water will flow out the bottom. (When the beads settle, water near the top of the column will become clear; this may also be siphoned off with a pipette.) Refill the column with additional dilute beads until the settled area nears the top of the column. When the beads have fully settled, place the second wet filter on the bed of beads and tamp down with the filter tool. Replacing the cap on the bottom assembly, and with the cap removed from the top assembly, attach the top assembly to the column. Once firmly attached, screw the plunger down until it meets the top filter. Water may be forced through the top assembly during this process.

With the column fully assembled, attach the column to your pump of choice and slowly (2-4 mL/min) flow distilled water through the column to ensure that any residual ethanol is removed and that the beads are fully settled. Be quite careful that no air bubbles are forced through the column. At larger flow rates, the beads may compress slightly; if this happens, simply screw the plunger on the top assembly down to again meet the filter. Before loading a sample on to the column, be sure to equilibrate the column with a loading buffer appropriate for the sample's environment prior to loading.

A.1 Purification from spinach

In order to obtain pure D1D2-cyt.*b559* reaction center samples, we perform multiple purification steps on commercially available spinach. We first follow the protocol for extracting BBY particles from spinach using the detergent Triton X-100 and sev-

Chemical	Total Volume	Molarity	Molecular Weight	Mass needed (g)
NaCl	0.5 L	4 M	58.44	116.88
HEPES (pH 7.5)	0.5 L	500 mM	238.31	59.58
EDTA	50 mL	100 mM	372.2	1.86
$MgCl_2$*$6H_2O$	50 mL	1 M	203.31	10.17
MES (pH 6.0)	0.5 L	500 mM	195.2	48.8
$CaCl_2$*$6H_2O$	250 mL	200 mM	219.08	10.95
Bis-Tris (pH 6.5)	0.5 L	200 mM	209.2	20.92
$MgSO_4$	0.5 L	100 mM	120.37	6.02
Tris (pH 8.0)	200 mL	1.6 M	121.6	38.91

Table A.1: A list of stock solutions useful in the D1D2-cyt.*b559* sample preparation. Note that those with pH values listed must be titrated to the appropriate values using NaOH pellets or HCl.

eral centrifugation steps [1]. BBY particles are the smallest complex isolated from spinach that is still capable of evolving oxygen, and they have been well-studied. To obtain pure D1D2-cyt.*b559* reaction center samples from there, we must use column chromatography to remove the surrounding light harvesting complexes and finally the bound CP43 and CP47 proteins, following a variation on the protocol by van Leeuwen et. al [12].

A.1.1 BBY Preparation

A.1.1.1 Preparation

We begin with ∼30 oz of grocery store spinach. Mature spinach with large, dark leaves is preferred to baby spinach for increased yields, as mature spinach has fewer proteases. Remove the stem and any large veins from the spinach and rinse with ddH_2O. In a large plastic container, create layers of ice, paper towel, de-veined spinach and additional paper towels. Allow this to chill in a refrigerator overnight to crisp the leaves for efficient blending. Chill the glass portion of the blender overnight as well. Prepare the stock solutions (table A.1) and buffers (Table A.2) and store at 4°C.

Buffer (Total Volume)	Volume	Ingredient	Stock Molarity	Final Molarity
Homogenization Buffer	200 mL	HEPES	0.5 M	50 mM
(2 L)	200 mL	NaCl	4.0 M	400 mM
	4 mL	$MgCl_2$	1.0 M	2 mM
	20 mL	EDTA	0.1 M	1 mM
Wash Buffer	30 mL	HEPES	0.5 M	50 mM
(300 mL)	1.125 mL	NaCl	4.0 M	15 mM
	1.2 mL	$MgCl_2$	1.0 M	4 mM
Triton Buffer	30 mL	MES	0.5 M	50 mM
(300 mL)	1.125 mL	NaCl	4.0 M	15 mM
	1.5 mL	$MgCl_2$	1.0 M	5 mM
Triton Solution	25g	Triton X-100		25% w/v
(100 mL)	75 mL	Triton Buffer		
SMN	41g	Sucrose		400 mM
(300 mL)	30 mL	MES	0.5 M	50 mM
	0.833 mL	NaCl	4.0 M	10 mM
BTS-400	136.92 g	Sucrose		400 mM
(1 L)	100 mL	Bis-Tris	0.2 M	20 mM
	20 mL	$MgCl_2$	1.0 M	20 mM
	25 mL	$CaCl_2$	0.2 M	5 mM
	100 mL	$MgSO_4$	0.1 M	10 mM

Table A.2: A list of buffers necessary for preparation of Tris-washed BBY particles.

A.1.1.2 Homogenization

Fill the chilled blender with ∼250 mL of homogenization buffer and ensure that the blades are covered. By hand, rip a few spinach leaves into the blender and pulse to shred. Add more spinach in this manner until the blender is half-full of shredded spinach and then blend for 15 seconds. Using a funnel, strain the mixture through 4 layers of cheesecloth into a 2L flask and squeeze to recover as much sample as possible without forcing larger material through the pores of the cheesecloth. Repeat this process until the spinach is entirely homogenized, replacing the cheesecloth and discarding as necessary when it becomes clogged. Chill six 250 mL centrifuge bottles on ice during this process. There should be approximately one liter of sample after this step.

A.1.1.3 Thylakoid preparation

Evenly distribute the homogenate into the chilled centrifuge bottles and spin at 4°C for 10 minutes at 6500 rpm in a Sorvall GSA rotor. Use a balance to ensure that opposite bottles are matched, and be careful not to overfill the bottles as they sit at an angle in the centrifuge. During this spin, take out and chill a 55 mL homogenizer tube, a homogenizer, a rubber policeman, a 500 mL flask, the wash buffer, and eight SS-34 centrifuge tubes.

After the spin, carefully discard the supernatant and add small amounts of wash buffer to each bottle. Using the rubber policeman, scrape each pellet to dissolve it and pour the mixture into the homogenizer tube until full. Homogenize the mixture and add to the 500 mL flask. Recover as much of the pellet as possible with only small amounts of wash buffer. After the initial resuspension, the buffer can be conserved by adding a small amount to one bottle, scraping off as much of the pellet as possible, and pouring this same liquid into another bottle until all the sample has been recovered and homogenized.

Distribute the homogenized sample amongst the eight centrifuge tubes, again being careful to balance them in pairs. Spin at 4°C for 10 minutes at 10,000 rpm in a SS-34 rotor. (Each additional step in the BBY preparation uses this rotor as well.) After this step, the pellet will consist of intact thylakoid membranes containing both photosystems. Discard the supernatant and use a small amount of Triton buffer (<50 mL) to resuspend and homogenize the pellets to create a concentrated solution. Note the distinction between Triton buffer, which does not yet contain Triton X-100, and Triton solution, which does. Next, we will determine how much chlorophyll we have in order to use an appropriate amount of Triton solution to properly solubilize the membranes.

Calculation of chlorophyll content

Dilute 10 μL of the homogenized sample in 5 mL of 80% acetone in a glass conical centrifuge tube and cover with parafilm to thoroughly mix in a vortex mixer. Spin with the tabletop centrifuge at a slow speed (∼1500 rpm) for 90 seconds to separate any undissolved material. With a visible spectrometer in transmittance mode with an 80% acetone cuvette as a reference for zero, record the optical density of the sample at 663 nm and 645 nm. Calculate the concentration of chlorophyll (μg/mL) in the acetone mixture [6]:

$$C_{chl} = 8.02 \cdot A_{663} + 20.2 \cdot A_{645}. \tag{A.1}$$

Measure the total volume of the homogenized sample V_s, and using the concentration determined above, calculate the total mass of chlorophyll in your sample:

$$M_{chl}(\text{mg}) = \frac{C_{chl}(\mu\text{g/mL})}{R_{dil}(\mu\text{L/mL})} V_s(\text{mL}) \tag{A.2}$$

where R_{dil} is the dilution ratio used to calculate the chlorophyll concentration. With 10 μL of sample in 5 mL of acetone, $R_{dil} = 2\mu\text{L/mL}$.

A.1.1.4 Triton incubation

We want to add detergent in a 25:1 weight ratio of detergent to chlorophyll; the Triton solution has 250 mg of detergent per mL, so we calculate the volume of Triton solution we need:

$$V_{sol}(\text{mL}) = \frac{M_{\text{Triton}}}{C_{\text{Triton}}} = \frac{25 \cdot M_{chl}(\text{mg})}{250(\text{mg/mL})} = 0.1 \cdot M_{chl}(\text{mg}) \tag{A.3}$$

resulting in needing 1 mL of Triton solution for every 10 mg of chlorophyll in the sample. **Dilute the sample with Triton buffer such that addition of this volume of Triton solution will result in a 2 mg/mL solution of chlorophyll.** Pour the homogenized sample into a flask with a stir bar on ice. Every step from this point on should be done on ice with room lights off and minimal ambient light; once detergent is added, the system is more susceptible to damage, and excess light or heat may degrade the sample. Dropwise, add the amount of Triton solution calculated above while stirring at a medium speed. Adding the drops into the vortex created by the stir bar helps disperse the Triton quickly, avoiding excessively large local concentrations of detergent. Start a timer with the addition of the first drop of detergent for 25 minutes. During the incubation, clean and chill the homogenization materials and 12 SS-34 centrifuge tubes. This detergent step preferentially solubilizes the stromal lamellae while the grana remain relatively intact. Since photosystem I is primarily located in the stromal lamellae and photosystem II is primarily in the grana, this step provides a means for separating the two photosystems. Diluting the sample to 2 mg/mL helps to ensure the detergent has appropriate access to the membranes.

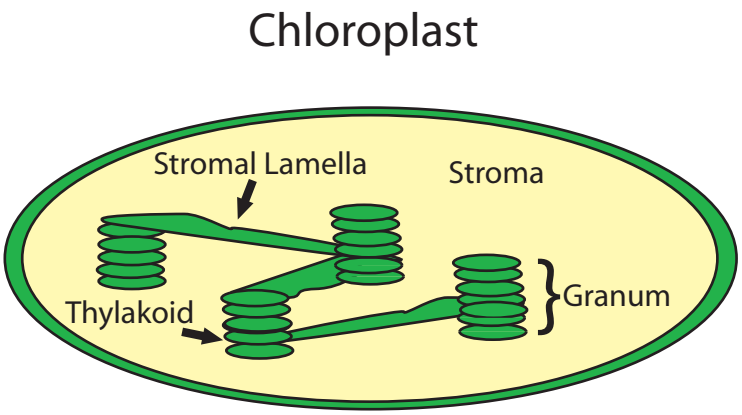

Figure A.1: Cartoon showing the inner structure of a chloroplast [7]. The stacked structure of the grana helps protect them from solubilization in this initial Triton incubation.

A.1.1.5 Final centrifugations

Immediately after the 25 minute Triton incubation, evenly distribute the sample and perform a short, slow spin: five minutes at 4°C at 3,000 rpm. This step is to remove any starch, which will pellet out at this speed, so unlike the previous centrifugation steps, here we keep the supernatant which contains solubilized membranes. Pour the supernatant into new centrifuge tubes and spin at 4°C for 30 minutes at 20,000 rpm. The solubilized photosystem I will remain in the supernatant, while the intact grana will form the pellet. Discard the supernatant and resuspend the pellets in SMN to roughly the same volume the sample had prior to Triton incubation. Note that roughly half the chlorophyll will be discarded with the photosystem I in the supernatant. Repeat the 4°C, 30 minute, 20,000 rpm spin. This step washes out excess Triton to prevent further solubilization. At this point the pellet will contain oxygen-evolving BBY particles. Keeping the total volume low, resuspend the pellets in BTS-400 with 0.05% w/v (50 mg/100 mL) dodecyl maltoside (n-Dodecyl-β-D-Maltopyranoside, Affymetrix). (Note: Dodecyl maltoside (DM) is typically stored with a dessicant in the freezer. Warm the DM to room temperature prior to weighing

it.) The small amount of detergent helps prevent aggregation in the sample. It is important to note, however, that while BTS -400 can be prepared ahead of time, DM addition must be done within hours of use. Again calculate the chlorophyll concentration, and dilute using BTS400 with 0.05% DM to 3 mg/mL, where BBY particles are most stable when stored. These samples can be stored in a -70°C freezer.

A.1.1.6 Tris washing

Removing the oxygen evolving complex (OEC) makes subsequent purification easier. This can be done at any point between purification steps; the sample may be stored at -70°C before or after Tris washing. In this step, mix equal volumes of sample (at 3 mg/mL) with 1.6 M Tris buffer (for a final Tris concentration of 0.8 M). Incubate on ice under room lights for 20 minutes. This is the only step since adding detergent in which the samples may be exposed to room light. The light encourages more rapid turnover of the OEC, aiding in its removal from the complex. Spin the sample at 4°C (again in an SS-34 rotor) for 30 minutes at 20,000 rpm. Discard the supernatant and resuspend in BTS-400 with 0.03% DM (30 mg/100 mL). Again, only add the DM to the BTS-400 shortly before use. Resuspend to 1.5 times the initial volume to decrease the chlorophyll concentration to 2 mg/mL, and store in a -70°C freezer.

A.1.2 D1-D2 purification

In this section, we will begin with thawed Tris-washed BBY particles. The goal in this section is to remove LHCII using a treatment of dodecyl-maltoside (DM) and then to use Triton X-100 to remove the bound CP43 and CP47 proteins using an anion exchange column.

Buffer (Total Volume)	Volume	Ingredient	Stock Molarity	Final Molarity
BTS-400	136.92 g	Sucrose		400 mM
(1 L)	100 mL	Bis-Tris	0.2 M	20 mM
	20 mL	$MgCl_2$	1.0 M	20 mM
	25 mL	$CaCl_2$	0.2 M	5 mM
	100 mL	$MgSO_4$	0.1 M	10 mM
BTS-200	68.46 g	Sucrose		200 mM
(1 L)	100 mL	Bis-Tris	0.2 M	20 mM
	20 mL	$MgCl_2$	1.0 M	20 mM
	25 mL	$CaCl_2$	0.2 M	5 mM
	100 mL	$MgSO_4$	0.1 M	10 mM
BTS-200 w/Triton	6.85 g	Sucrose		200 mM
(100 mL)	10 mL	Bis-Tris	0.2 M	20 mM
	2 mL	$MgCl_2$	1.0 M	20 mM
	2.5 mL	$CaCl_2$	0.2 M	5 mM
	10 mL	$MgSO_4$	0.1 M	10 mM
	10 g	Triton X-100		10% w/v
BTS-200 (High Salt)	6.85 g	Sucrose		200 mM
(100 mL)	10 mL	Bis-Tris	0.2 M	20 mM
	2 mL	$MgCl_2$	1.0 M	20 mM
	2.5 mL	$CaCl_2$	0.2 M	5 mM
	0.903 g	$MgSO_4$		75 mM

Table A.3: A list of buffers necessary for column chromatography of Tris-washed BBY particles to make D1D2-cyt.*b559* reaction centers.

A.1.2.1 Dodecyl maltoside treatment

While the sample vial is thawing in a water bath (if using previously-stored Tris-washed BBY particles), or while the sample is kept in an ice bath, prepare 1/7 of the sample volume of 10% DM in BTS-400. For 12 mL of sample at 2 mg/mL Chl, this is 171.4 mg of DM and 1.714 mL of BTS-400. Also prepare a centrifuge with an SE-12 rotor for a 4°C spin at 19,500 rpm, and chill two centrifuge tubes on ice.

In the dark, while spinning the sample in an ice bath, slowly add the detergent mixture. Start a timer with the first drop of detergent and incubate while stirring for 10 minutes. During this incubation, the DM is solubilizing the BBY particles; LHCII and photosystem II will be separately solubilized in this step. Immediately distribute the sample evenly between centrifuge tubes, and spin for 20 minutes at 4°C at 19,500 rpm. Any unsolubilized material will form a small pellet in the centrifuge tubes. Pour the supernatant into a conical tube for ease of loading on to the column.

A.1.2.2 Removing LHCII

During the above centrifugation step, prepare the previously packed Q-sepharose column and turn on the UV-monitoring system (280 nm). With the column and the buffer both in ice baths, ensure the column is equilibrated with cold BTS-400 with 0.03% DM, and note the baseline reading on the UV monitor (typically zero). While an FPLC system can be used with the column, we use a peristaltic pump for all chromatography steps. (Note, that in our particular FPLC system (Pharmacia Biotech), the pumps must be running in order to use the UV monitor. These can be run at 0.01 mL/min, sourced from 20 μm filtered ddH_2O and sent directly to a waste jar.) The output from the UV monitor should initially go to a waste jar. Slowly ($\sim$1-2 mL/min) load the solubilized sample on to the column. Once loaded on the column, the negatively charged photosystem II will be attracted to the positively charged beads and remain on the column which should now be dark green.

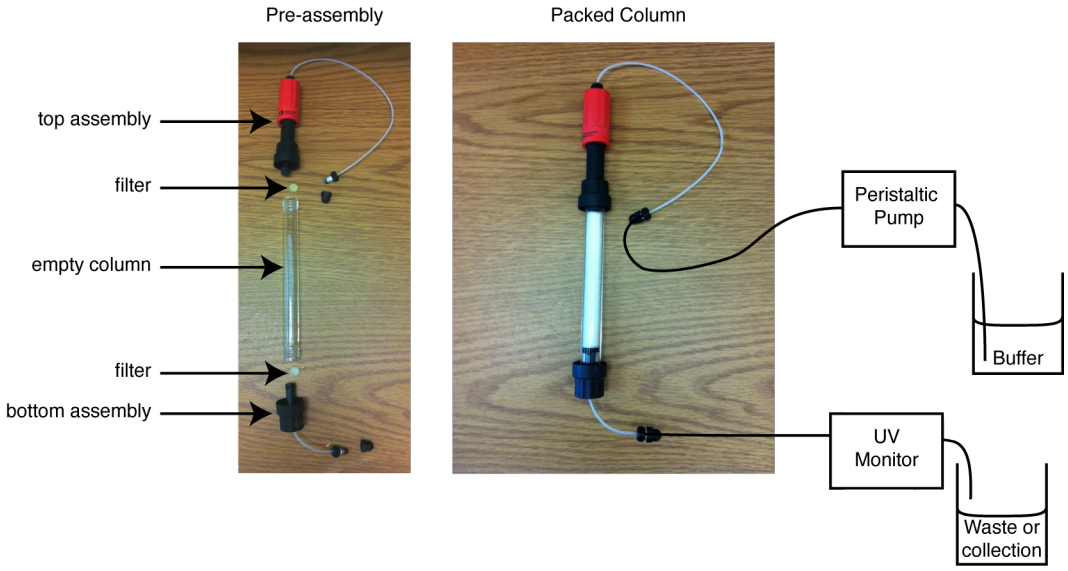

Figure A.2: Left: Empty column assembly. Right: Packed column, and a diagram detailing the setup for running the column. Note that everything should be on ice while the column is running.

(Q-Sepharose is a strong anion exchanger with a quarternary amine group.) Begin washing the column with BTS-400 with 0.03% DM. The now-free LHCII particles and any unbound chlorophyll will come off the column at this stage and cause a large change the UV absorption; continue washing until the UV monitor nears the baseline reading and plateaus. At this point, the column contains photosystem II consisting of the D1D2-cyt.*b559* reaction center and tightly-bound CP43 and CP47 proteins; for intact reaction center cores instead of the D1D2-cyt.*b559* reaction center, you can skip the Triton incubation steps below and elute the sample from the column here.

A.1.2.3 Triton incubation

In order to dissociate CP43 and CP47 from the D1D2-cyt.*b559* reaction center we will use two incubations of a 10% solution of the detergent Triton X-100 in BTS-200. After the column is thoroughly washed of LHCII and free chlorophyll, slowly load the Triton/BTS-200 solution on the column. Carefully watch the UV monitor; Triton strongly absorbs in the UV, and once the UV absorption begins rising, you

can be sure the Triton solution has fully covered the column. Turn off the peristaltic pump and let the sample incubate for 20 minutes. Thoroughly wash the Triton off the column with BTS-200 with 0.03% DM until the UV absorption again returns to its baseline value. The material flowing off the column will be green as free CP43 and CP47 come off the column. Repeat this Triton incubation and wash a second time to ensure that what remains on the column is free of CP43 and CP47.

A.1.2.4 D1D2-cyt.*b559* elution

Most of the chlorophylls in photosystem II are bound in the CP43 and CP47 proteins instead of the D1D2-cyt.*b559* reaction center, so the column will likely be pale green at this point and should contain only the highly-charged D1D2-cyt.*b559* reaction center. After the second Triton incubation and wash, the UV absorption should drop to the baseline value; this final wash should be quite thorough. When this happens, we can begin using a high-salt (75 mM $MgSO_4$) version of the BTS-200 with 0.03% DM buffer to elute the D1D2-cyt.*b559* reaction center. Carefully collect fractions once you begin running the high salt solution; the eluant should be visibly green. Take care to isolate the most concentrated eluant; running the elution buffer at a slow speed will allow for the greatest resolution.

A.1.2.5 Verifying the purity

At this point, we need to verify that the eluant is actually the D1D2-cyt.*b559* reaction center. This can be done spectroscopically. Using an appropriate dilution of the fractions, record an absorption spectrum from 300 nm to 800 nm. We can use a ratio of the peaks in the Soret absorption band as a proxy for determining the purity of the samples, since chlorophyll *a* and pheophytin *a* have slightly different peak shapes in this region. In pure D1D2-cyt.*b559* samples, the ratio of A_{416}/A_{435} will be 1.2. If the sample is contaminated, this ratio will be lower; free CP47 has a ratio of 0.75 and

CP47 bound to the D1D2-cyt.*b559* reaction centerwill have a ratio of 0.9 [4]. Should the sample be contaminated with CP43 or CP47, it can be diluted with BTS 200 (preferably without any $MgSO_4$) with 0.03% DM to lower the $MgSO_4$ concentration, reloaded on the column and treated with an extra Triton incubation/wash to remove any remaining CP43 or CP47. The fractions may be stored in a -70°C freezer until ready for use.

A.1.2.6 Concentrating the sample

Often the sample will be too dilute for experimental use straight off the column, particularly since it must be mixed with glycerol for use in the cryostat. We concentrate the samples using a spin filter (Millipore Amicon Ultra 10 kDa 4mL). Evenly distribute the sample to be concentrated between two vials and spin at 3800g for 20 minutes at room temperature (Beckman GS-15R). Discard the liquid at the bottom of the vial and note the volume of sample remaining above the filter. Dilute at a ratio of 4:1 with the dilution buffer (BTS without $MgSO_4$ or sucrose) in order to reduce the concentration of salt and sucrose in the sample, and repeat the spin. Collect the now-concentrated sample with a syringe and keep at 4°C until ready for use in the experimental setup. Note that this step should not be done far in advance of the experiment nor refrozen at -70°C; having diluted the sucrose concentration, the sample no longer has sufficient cryoprotectant. For 77K experiments, glycerol will be added in a 2:1 (v/v) ratio to form an optical glass in the sample cell.

A.1.3 Reduced D1-D2 preparation

In the experiments in Appendix E we use a chemically reduced version of the D1D2-cyt.*b559* reaction center. Treatment with sodium dithionite and exposure to actinic light introduces a negative charge on the $Pheo_{D1}$ preventing further charge transfer to this chromophore. This preparation must be done carefully in an oxygen-

free environment since exposure to oxygen will re-oxidize the pheophytin. We follow a procedure similar to that of Jankowiak et al. [5].

With room lights off, we prepare a positive-pressure nitrogen environment within a glove bag containing everything needed to create a vacuum-safe sample cell including concentrated D1D2-cyt.*b559* reaction centers as prepared above, sodium dithionite, and small volumes of glycerol and low-salt BTS-200 buffer. We bubble nitrogen through the glycerol for 24 hours to ensure that the viscous liquid is sufficiently free of oxygen, and we leave the BTS-200 buffer in a petri dish with large surface area for a number of hours prior to sample preparation. We prepare a concentrated sodium dithionite solution using 62.5 mg of sodium dithionite in 0.5 mL of BTS-200. To 15 μL of the D1D2-cyt.*b559* sample we add 2.5 μL of the sodium dithionite solution and 35 μL of glycerol, resulting in a final sodium dithionite concentration of 6 mg/mL and maintaining the 2:1 ratio of glycerol/buffer needed in the experiment. This may require vortexing to thoroughly mix. Approximately 35 μL of this mixture is placed in the sample cell and the cell is sealed to air. In order to activate the dithionite, the sample cell is placed under 2 cm of water and exposed to incandescent light for 30 minutes. A linear absorption spectra was taken to ensure the sample was indeed reduced.

A.2 Purification from *Acaryochloris marina*

In addition to the D1D2-cyt.*b559* reaction center purified from spinach, it is of interest to create analogous complexes from novel systems, such as *Acaryochloris marina*. Most of the chlorophylls within this cyanobacteria's photosystems consist of chlorophyll *d* [9], leading to a shifted Q_y absorption near 700 nm instead of 680 nm. Unfortunately, an analogous complex to the D1D2-cyt.*b559* reaction centers from spinach with just 6 or 8 pigments has not yet been purified. In bacterial systems, the thylakoid membranes are not structured as they are in plants (A.1), and both

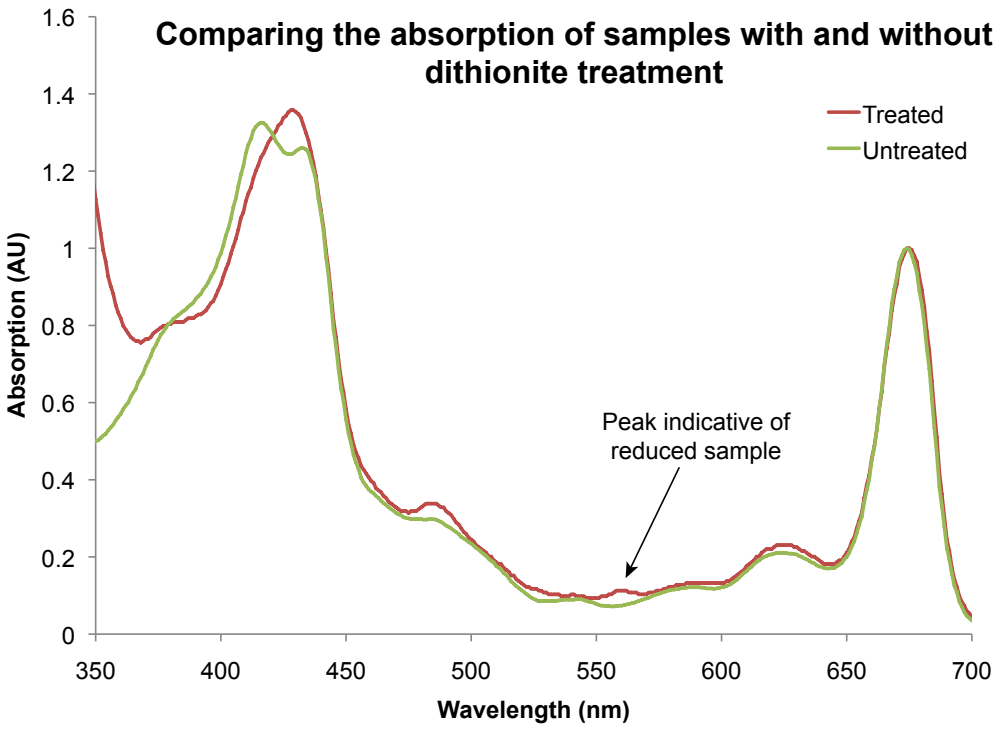

Figure A.3: Room temperature absorption spectrum of D1D2-cyt.*b559* reaction centers in a 2:1 glycerol mixture, both with and without dithionite treatment. The spectra are normalized to the Q_y absorption peak.

PSI and PSII are evenly distributed within the membranes. Therefore, there is not an equivalent PSII-rich BBY particle, and we are unable to separate PSI and PSII in the same manner. Chen et al. have purified "large" and "small" photosystem II complexes from *A. marina*, where the small complex has ∼20 chlorophylls [3]. With samples generously provided by Robert Blankenship, we have attempted our own protocol for purification of an analogous complex with helpful discussions from Min Chen as well.

A.2.1 Initial attempts

We initially received frozen and pelleted thylakoid membranes from the Blankenship group. The cultured cells had been broken in a PBS buffer (0.75 M phosphate, pH 7.0) with a bead beater. After a spin to remove the unbroken cells, the membranes were pelleted out with ultracentrifugation, frozen, and sent to us. The first goal is to separate photosystem I from photosystem II. Once photosystem II is separated, the purification for a "D1D2" complex should not vary significantly from the spinach preparation.

A.2.1.1 First attempt

In our initial attempt, we used many of the same buffers as in our preparations from spinach, and expected to separate PSI from PSII via column chromatography after solubilization of the membranes. We resuspended the pellet in BTS-400 with 0.03% DM, and calculated the chlorophyll content. The procedure for calculating the chlorophyll content is similar to that above, but with different absorption measurements and coefficients to account for the change to chlorophyll *d*. We use the

Buffer (Total Volume)	Volume	Ingredient	Stock Molarity	Final Molarity
Buffer C	136.92 g	Sucrose		400 mM
(1 L)	100 mL	MES	0.5 M	50 mM
	10 mL	$MgCl_2$	1.0 M	10 mM
	50 mL	$CaCl_2$	0.2 M	10 mM
Buffer E-X	136.92 g	Sucrose		400 mM
(1 L)	100 mL	MES	0.5 M	50 mM
	10 mL	$MgCl_2$	1.0 M	10 mM
	50 mL	$CaCl_2$	0.2 M	10 mM
	X*10 mL	$MgSO_4$	0.1 M	X mM

Table A.4: A list of buffers used in the purification of complexes from *A. marina*. Note that Buffer E is an elution buffer, and we replace X in the buffer name with the concentration of $MgSO_4$ (in mM). Also note that after membrane solubilization, all buffers will have fresh dodecyl maltoside (0.03% unless otherwise noted).

equations from [8] for methanol:

$$C_{chl\ a+chl\ d} = 12.69 \cdot A_{664} + 9.83 \cdot A_{691} \tag{A.4}$$

$$C_{chl\ d} = -0.33 \cdot A_{664} + 12.94 \cdot A_{691} \tag{A.5}$$

We solubilized the membranes at a chlorophyll concentration of 1 mg/mL with 1% DM on ice in the dark for 10 minutes. A spin for 20 minutes with the SE-12 rotor at 19,500 rpm at room temperature pelleted out any unsolubilized material; the supernatant was loaded with a peristaltic pump onto a Q-sepharose column equilibrated with BTS-400 with 0.03% DM. Flow-through was monitored with a UV monitor and by eye. A large fraction of material flowed straight through the column. With thorough washes between each step, we eluted what remained on the column stepwise from 10 mM $MgSO_4$ to 1 M $MgSO_4$, at which point the column was still visibly green. We concluded that we should try a weak ion exchange column in lieu of the strong ion exchanger, Q-Sepharose.

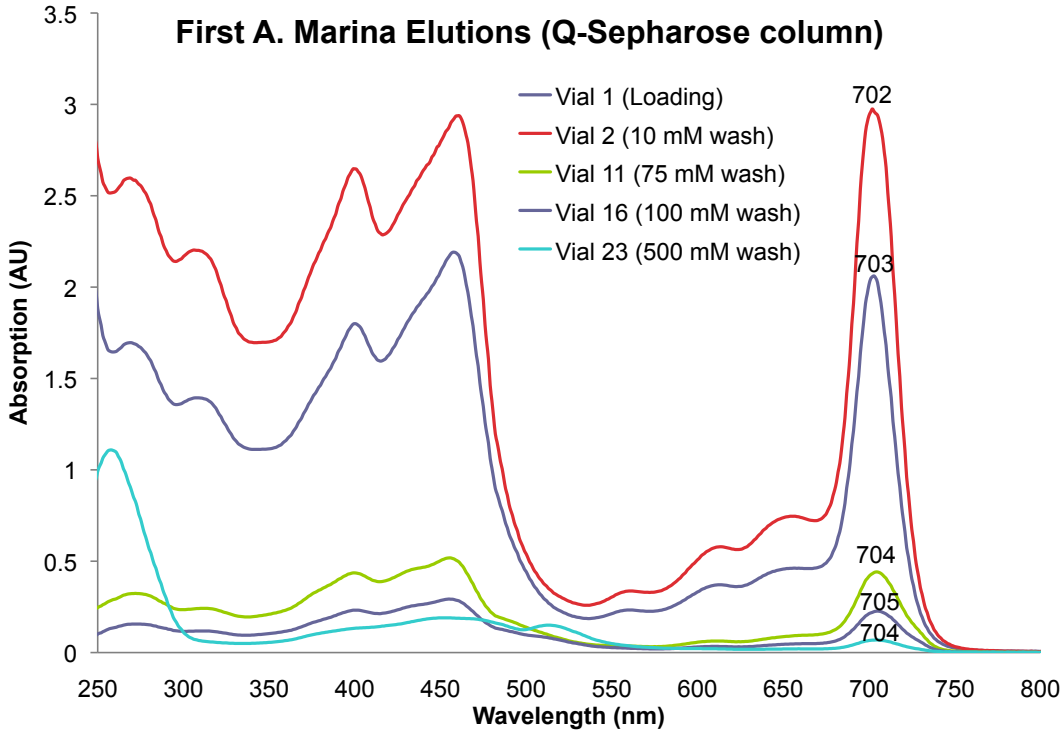

Figure A.4: Room temperature absorption spectrum of the elutions from the first *A. marina* preparation. The numbers above the Q_y peak indicate the wavelength of the maximum absorption, which can serve as an indicator for determining if a fraction has PSI or PSII.

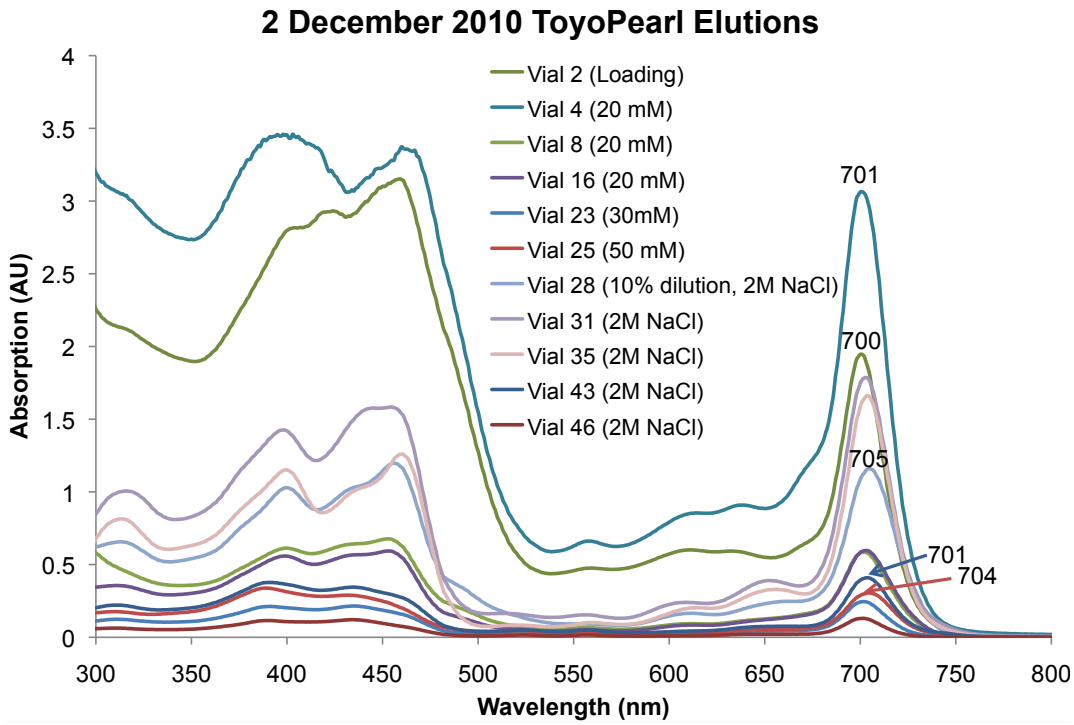

Figure A.5: Room temperature absorption spectrum of the elutions from the second *A. marina* preparation.

A.2.1.2 Second elution

In this procedure, we imitated the protocol and buffers in [13]. We noticed that that the previously resuspended sample had some solids that had settled. This suggests DNA contamination. We again solubilized the membranes stirring, on ice, in the dark, at 1 mg/mL with 1% DM in buffer C, although we allowed 30 minutes for the solubilization. Again, a 20 minute spin with the SE-12 rotor at 19,500 removed any unsolubilized material. The supernatant was loaded onto a DEAE-Toyopearl column, and was washed with buffer E-20. We eluted stepwise to E-50 with little coming off the column, so we tried Buffer C + 2 M NaCl to clean the column.

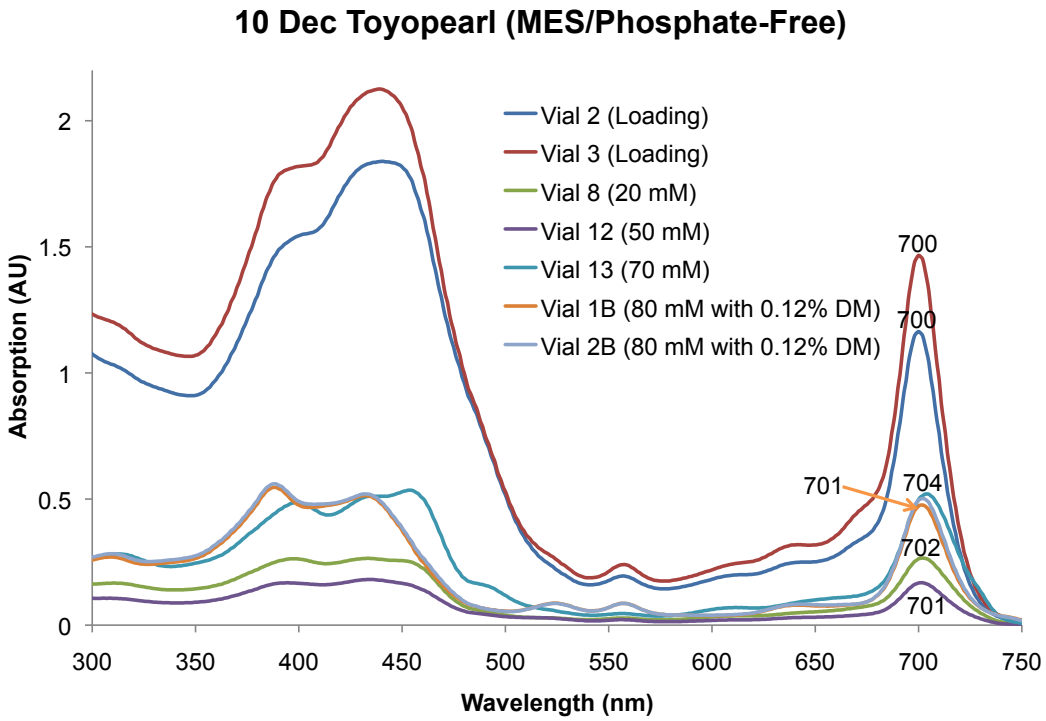

Figure A.6: Room temperature absorption spectrum of the elutions from the third *A. marina* preparation.

A.2.1.3 Third elution

That such large concentrations of salt had been needed to clean the column in the previous elutions, we became suspicious of the PBS buffer and subsequently performed three wash/centrifugation steps with a fresh pellet and buffer C to remove any residual phosphates. This washed sample was used for this and the next preparation. (Note, the chlorophyll concentration in this preparation was ~0.5 mg/mL.) We allowed for an even longer solubilization step with 1% DM for 2 hours in the dark on ice. After spinning (20 minutes, 19,500 rpm, SE-12 rotor), we loaded the supernatant on the DEAE-Toyopearl column and washed with buffer E-20. We eluted stepwise to E-100 with little success. We considered that there was not enough detergent on the column, and tried washing with buffer E-80 with 0.12% DM which cleaned the column.

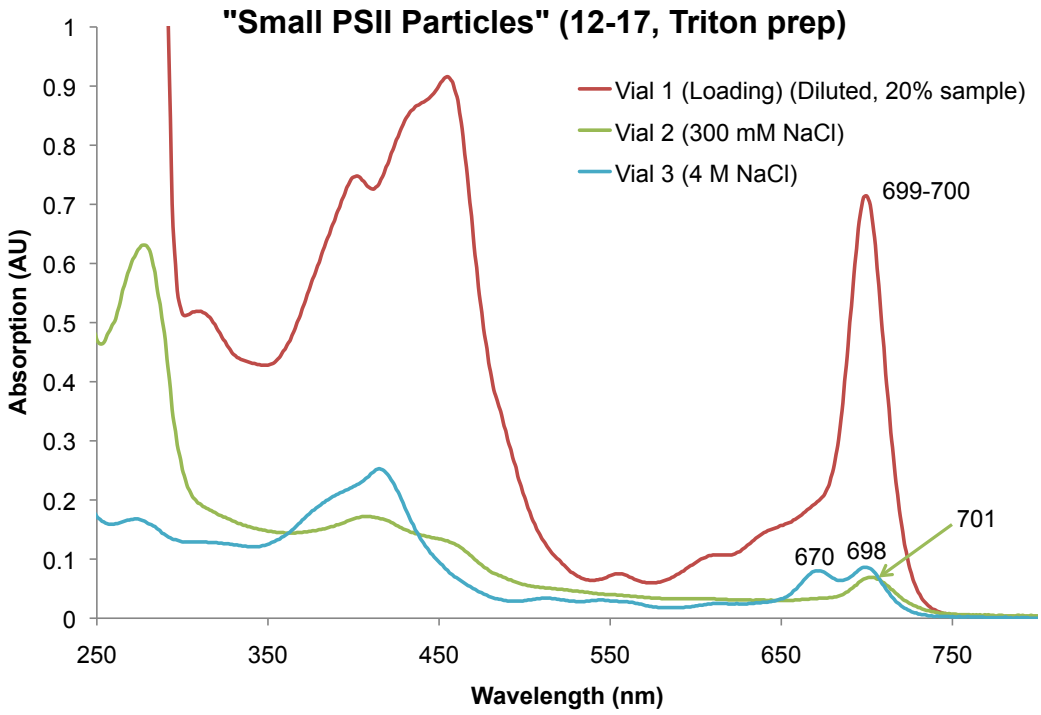

Figure A.7: Room temperature absorption spectrum of the elutions from the "small" particle preparation.

A.2.1.4 Fourth elution

In our fourth and final preparation, we attempted to reproduce the "small" particle sample from [3]. With the phosphate-"free" sample, we pelleted the cells and resuspended in 50 mM MES. We solubilized the membranes with 4.5% Triton (in MES) for two hours in the dark on ice. A 30 minutes spin at 19,500 rpm in the SE-12 rotor at 4°C removed unsolubilized material and the supernatant was loaded onto a DEAE-Toyopearl column equilibrated with 50 mM MES with 0.2% Triton. Most of the sample came through immediately, but what remained was eluted with 50 and 75 mM NaCl with 0.2% Triton, then 75 and 300 mM NaCl with 0.12% DM. The column was cleaned with 4M NaCl with 0.12% DM.

A.2.2 Intended protocol

None of our initial attempts were successful at separating PSI and PSII. We note that the spectra showed degraded samples and the initial wash steps in the third and fourth preparations may not have been sufficient to remove all the phosphate. Aggregation on the column may have been an issue, so all buffers should have increased detergent concentrations, Future attempts will begin with whole cells; the thylakoid preparation will no longer use a high-phosphate buffer and DNAases will be used when the cells are broken to prevent contamination from DNA. Once we have clean thylakoid membranes, one method for photosystem II purification will be to follow the equivalent protocol for *Synechocystis* with a larger detergent concentration, similar to the third elution above. The other method follows that from Min Chen [2].

A.2.2.1 Thylakoid preparation

Starting with washed cells, we follow a protocol adapted from [2] for preparing oxygen evolving thylakoid membanes. After harvesting, pellet the cells (GS3 Sorvall, 6500 rpm, 10 min, 4°C) and wash in washing buffer twice at ∼20-40 mL washing buffer per mg chl *d*. Place the washed cells in an ice box for at least 30 minutes, and pellet once again (GS3 Sorvall, 6500 rpm, 8 min, 4°C).

Resuspend the cells in 15 mL of break buffer. Add an equal volume of silicon carbide beads and break the cells in a bead beater for 20 seconds 6 times, allowing for a 5 minute cool down period. Use less than 3 times the original volume and wash the beads; spin at 1000 rpm for 5 minutes twice to remove the beads. Spin the supernatant again (5000 rpm, 10 min) to pellet any unbroken cells or cellular debris.

Add 40 mM $CaCl_2$ to the supernatant to stabilize the membranes and centrifuge (SS34 rotor, 19,000 rpm, 60 min) to collect the pelleted thylakoid membranes. The membranes may be resuspended in a freezing buffer (20-25% (v/v) glycerol, 20 mM MES pH 6.5, 20 mM $CaCl_2$, and 20 mM $MgCl_2$) and stored at -70°C.

Buffer	Final Molarity	Ingredient
Washing Buffer	0.8 M	Sucrose
	40 mM	MES (pH 6.3-6.5)
Break Buffer	0.8 M	sucrose
	40 mM	MES (pH 6.5)
	1 mg/15mL	PMSF
	100 mg/15 mL	BAS
Freezing Buffer	20-25% (v/v)	glycerol
	20 mM	MES (pH 6.5)
	20 mM	$CaCl_2$
	20 mM	$MgCl_2$
M Buffer	20 mM	MES (pH 6.0)
	20 mM	$CaCl_2$
	10 mM	$MgCl_2$
	500 mM	Manitol
MAX Buffer	20 mM	MES (pH 6.0)
	20 mM	$CaCl_2$
	10 mM	$MgCl_2$
	500 mM	Manitol
	X mM	$MgSO_4$

Table A.5: A list of buffers used in the protocol by Chen for purification of complexes from *A. marina* [2]. Note that after membrane solubilization, all buffers will have fresh dodecyl maltoside (0.03% unless otherwise noted).

A.2.2.2 PSII separation

Resuspend thylakoid membranes in M buffer to a chlorophyll *d* concentration of 0.75 mg/mL to 0.9 mg/mL. Solubilize the membranes in 1% DM in M buffer at room temperature in the dark for 30 minutes. (Note, add detergent such that the M buffer has 10% w/v DM and add enough such that the final concentration is 1% in the sample. Spin to remove unsolubilized material (20 min, room temperature, 19,500 rpm, SS-34 rotor). Load the supernatant onto a Q-sepharose column equilibrated with buffer M and 0.03% DM. Wash the column with five column volumes of buffer MA15, 4 column volumes of MA25, and collect fractions in a gradient from MA25-MA200 within 3 column volumes. This should separate phycobiliproteins, PSII, PSI and Pcb-type light harvesting complexes.

Reload the PSII containing fraction(s) onto a clean Q-sepharose column, equilibrated with MA30 with 0.03% DM. Wash with five column volumes of MA3 and begin an $MgSO_4$ concentration from 30 mM to 120 mM gradient for elution in seven column volumes. PSI and PSII should come off the column at different salt concentrations. Compare the peak absorption of the Q_y band after elution to determine which fractions contain PSI or PSII; the peaks are at 708.5 nm [10] and 702 nm [11], respectively.

A.2.2.3 "D1D2" purification

The fractions that contain PSII will be diluted back to a low concentration of $MgSO_4$ and reloaded onto the Q-sepharose column. Wash thoroughly with MA15. Incubate the material on the column with 10% Triton in MA15 for 20 minutes and wash thoroughly with MA15. Repeat the Triton incubation and wash until the eluant has no UV absorption and is visibly colorless. Increase the $MgSO_4$ concentration stepwise until the absorption of the eluant increases and begin collecting fractions. A thorough examination of the fraction will be necessary to determine the pigment and

protein composition of the eluant.

References

[1] D. Berthold, G. Babcock, and C. F. Yocum. A highly resolved, oxygen-evolving photosystem II preparation from spinach thylakoid membranes. *FEBS Letters*, Jan 1981.

[2] M. Chen. O_2 active thylakoid membranes preparation and PSI and PSII complexes isolation from *Acaryochloris marina*. Private communication, Jan 2011.

[3] M. Chen, A. Telfer, S. Lin, A. Pascal, A. W. D. Larkum, J. Barber, and R. E. Blankenship. The nature of the photosystem II reaction centre in the chlorophyll *d*-containing prokaryote, *Acaryochloris marina*. *Photochemical & Photobiological Sciences*, 4(12):1060–1064, Nov 2005.

[4] C. Eijckelhoff, H. van Roon, M. L. Groot, R. van Grondelle, and Jan P Dekker. Purification and spectroscopic characterization of photosystem II reaction center complexes isolated with or without Triton X-100. *Biochemistry*, 35(39):12864–12872, 1996.

[5] R. Jankowiak, M. Rätsep, R. Picorel, and M. Seibert. Excited states of the 5-chlorophyll photosystem II reaction center. *Journal of Physical Chemistry*, Oct 1999.

[6] G. Mackinney. Absorption of light by chlorophyll solutions. *Journal of Biological Chemistry*, 1941.

[7] Jeffrey A. Myers. *Two-dimensional electronic spectroscopy of the photosystem II D1D2-cyt.*b559 *reaction center complex*. PhD thesis, University of Michigan, 2010.

[8] R. J. Ritchie. Consistent sets of spectrophotometric chlorophyll equations for acetone, methanol and ethanol solvents. *Photosynthesis Research*, 89(1):27–41, Jul 2006.

[9] H. Schiller, H. Senger, H. Miyashita, S. Miyachi, and H. Dau. Light-harvesting in *Acaryochloris marina*-spectroscopic characterization of a chlorophyll *d*-dominated photosynthetic antenna system. *FEBS Letters*, Jan 1997.

[10] T. Tomo, Y. Kato, T. Suzuki, S. Akimoto, T. Okubo, T. Noguchi, K. Hasegawa, T. Tsuchiya, K. Tanaka, and M. Fukuya. Characterization of highly purified photosystem I complexes from the chlorophyll *d*-dominated cyanobacterium *Acaryochloris marina* MBIC 11017. *Journal of Biological Chemistry*, 283(26):18198, 2008.

[11] T. Tomo, T. Okubo, S. Akimoto, M. Yokono, H. Miyashita, T. Tsuchiya, T. Noguchi, and M. Mimuro. Identification of the special pair of photosystem II in a chlorophyll *d*-dominated cyanobacterium. *Proceedings of the National Academy of Sciences*, Apr 2007.

[12] P. J. van Leeuwen, M. C. Nieveen, E. J. van de Meent, J. P. Dekker, and H. J. van Gorkom. Rapid and simple isolation of pure photosystem II core and reaction center particles from spinach. *Photosynthesis Research*, 28:149–153, 1991.

[13] D. V. Vavilin. Methods for the isolation of functional photosystem II core particles from the cyanobacterium *Synechocystis* sp. PCC 6803. In Robert Carpentier, editor, *Photosynthesis Research Protocols (Methods in Molecular Biology)*. Springer Protocols, 2011.

APPENDIX B

Calculating the Response Function within the Doorway-Window Approximation

This appendix gives the expressions necessary to calculate the final response function given in Equation 5.13 in Chapter V and repeated here for clarity:

$$S^{(3)}(t_3,t_2,t_1) = R^{(c)}(t_3,t_2,t_1) + \sum_{\mu\nu} W_\mu(t_3) G_{\mu\nu}(t_2) D_\nu(t_1) + W_0(t_3) D_0(t_1) \tag{B.1}$$

The following expressions can be found in the appendices from [1].

B.1 Coherent contribution

We start with the coherent contribution, $R^{(c)}$. This term is split up perturbatively, such that:

$$R^{(c)}(t_3,t_2,t_1) = R(t_3,t_2,t_1) - R(t_3,\infty,t_1) \tag{B.2}$$

The first term represents the response function for $H_1 = 0$, while $R(t_3,\infty,t_1)$ can be expressed in terms of the doorway-window functions such that the total coherent

contribution is recast:

$$R^{(c)}(t_3,t_2,t_1) = R(t_3,t_2,t_1) - \sum_{\mu} W_{\mu}(t_3)D_{\mu}(t_1) - W_0(t_3)D_0(t_1) \tag{B.3}$$

Note that the third term here cancels the final term in Equation B.1.

Within the rotating wave approximation, only three pathways of the $H_1 = 0$ ressponse function survive:

$$R(t_3,t_2,t_1) = R_I(t_3,t_2,t_1) + R_{II}(t_3,t_2,t_1) + R_{III}(t_3,t_2,t_1) \tag{B.4}$$

$$\begin{aligned} R_I(t_3,t_2,t_1) = &- i\sum_{\mu\nu} d_\mu d_\mu d_\nu d_\nu \exp[-f^{(1)}_{\mu\nu}(0,t_2+t_1,t_3+t_2+t_1,t_1)] \\ &\times \exp[-i\epsilon_\mu(t_3+t_2) + i\epsilon_\nu(t_2+t_1)] \end{aligned} \tag{B.5}$$

$$\begin{aligned} R_{II}(t_3,t_2,t_1) = &- i\sum_{\mu\nu} d_\mu d_\mu d_\nu d_\nu \exp[-f^{(1)}_{\mu\nu}(0,t_1,t_3+t_2+t_1,t_2+t_1)] \\ &\times \exp[-i\epsilon_\mu t_3 + i\epsilon_\nu t_1] \end{aligned} \tag{B.6}$$

$$\begin{aligned} R_{III}(t_3,t_2,t_1) = &- i\Bigg\{ \sum_{\mu\nu\bar{\alpha}} d_{\mu\bar{\alpha}} d_{\nu\bar{\alpha}} d_\nu d_\mu \exp[-f^{(2)}_{\mu\nu,\bar{\alpha}}(t_1,t_2+t_1,t_3+t_2+t_1,0)] \\ &\times \exp[-i\epsilon_\mu(t_3+t_2+t_1) + i\epsilon_{\bar{\alpha}} t_3 + i\epsilon_\nu t_2] \Bigg\}^* \end{aligned} \tag{B.7}$$

where

$$\begin{aligned} f^{(1)}_{\mu\nu}(\tau_4,\tau_3,\tau_2,\tau_1) \equiv &g_{\mu\mu}(\tau_2-\tau_1) - g_{\mu\nu}(\tau_3-\tau_1) + g_{\mu\nu}(\tau_4-\tau_1) \\ &+ g_{\mu\nu}(\tau_3-\tau_2) - g_{\mu\nu}(\tau_4-\tau_2) + g_{\nu\nu}(\tau_4-\tau_3) \end{aligned} \tag{B.8}$$

and

$$
\begin{aligned}
f^{(2)}_{\mu\nu,\bar{\alpha}}(\tau_4,\tau_3,\tau_2,\tau_1) \equiv & g_{\mu\mu}(\tau_2-\tau_1) - g_{\mu\bar{\alpha}}(\tau_2-\tau_1) + g_{\mu\bar{\alpha}}(\tau_3-\tau_1) - g_{\mu\nu}(\tau_3-\tau_1) \\
& + g_{\mu\nu}(\tau_4-\tau_1) - g_{\mu\bar{\alpha}}(\tau_3-\tau_2) + g_{\mu\nu}(\tau_3-\tau_2) \\
& - g_{\mu\nu}(\tau_4-\tau_2) + g_{\bar{\alpha}\bar{\alpha}}(\tau_3-\tau_2) - g_{\bar{\alpha}\nu}(\tau_3-\tau_2) \\
& + g_{\bar{\alpha}\nu}(\tau_4-\tau_2) - g_{\bar{\alpha}\nu}(\tau_4-\tau_3) + g_{\nu\nu}(\tau_4-\tau_3)
\end{aligned}
\tag{B.9}
$$

The doorway and window functions needed to calculate the coherent contribution at $t_2 = \infty$ and the other components of the response function will be given in the next section.

B.2 Doorway-window functions

This section evaluates the doorway and window functions to the zeroth order in H_1:

$$\bar{D}_\nu(\tau,t) = D_\nu(t)\delta(\tau) \tag{B.10}$$

$$\bar{W}_\mu(t,\tau) = W_\mu(t)\delta(\tau) \tag{B.11}$$

and they can be represented in a form:

$$D_\nu(t) = D^L_\nu(t) + D^L_\nu(-t) \tag{B.12}$$

$$W_\mu(t) = W^L_\mu(t) + W^L_\mu(-t) \tag{B.13}$$

Calculating the correlation functions using the second order cumulant expansion, we can obtain:

$$D_\nu^L(t) = -\, d_\nu^2 \exp[-i\epsilon_\nu t - g_{\nu\nu}(t)] \tag{B.14}$$

$$\begin{aligned} W_\mu^L(\tau) = \lim_{t\to\infty} \Big\{ & i d_\mu^2 \exp[-f_{\mu\mu}^{(1)}(-t,0,\tau,-t)] \exp[-i\epsilon_\mu \tau] \\ & - \sum_{\bar{\nu}} i d_{\mu\bar{\nu}}^2 \exp[-f_{\mu\mu,\bar{\nu}}^{(2)}(-t,\tau,0,-t)] \exp[-i(\epsilon_{\bar{\nu}} - \epsilon_\mu)\tau] \Big\} \end{aligned} \tag{B.15}$$

which can be simplified by using the following identities:

$$\lim_{t\to\infty} f_{\mu\mu}^{(1)}(-t,0,\tau,-t) = g_{\mu\mu}^*(\tau) - 2i\lambda_{\mu\mu}\tau \tag{B.16}$$

$$\lim_{t\to\infty} f_{\mu\mu,\bar{\nu}}^{(2)}(-t,\tau,0,-t) = g_{\mu\mu}(\tau) + g_{\bar{\nu}\bar{\nu}}(\tau) - 2g_{\mu\bar{\nu}}(\tau) - 2i(\lambda_{\mu\bar{\nu}} - \lambda_{\mu\mu})\tau \tag{B.17}$$

The terms D_0 and W_0 cancel, but I reproduce them here for completeness:

$$D_0(t) = -\sum_\nu D_\nu(t) \tag{B.18}$$

$$W_0(t) = i\sum_\mu [D_\mu^L(t) - D_\nu^L(-t)] \tag{B.19}$$

B.3 Master equation kernel

This section contains the expressions necessary to calculate the kernel, $K_{\mu\nu}$, for use in the master equation (Equation 5.14) for solving the time dependence of $G_{\mu\nu}$. The kernel is calculated to second order in H_1, such that

$$\bar{K}_{\mu\nu}(t) = K_{\mu\nu}^L(t) + K_{\mu\nu}^L(-t) \tag{B.20}$$

where $K^L_{\mu\nu}(t)$ can be evaluated as:

$$K^L_{\mu\nu}(\tau) = K^F_{\mu\nu}(\tau)\{\ddot{g}_{\mu\nu,\nu\mu}(\tau) - [\dot{g}_{\nu\mu,\nu\nu}(\tau) - \dot{g}_{\nu\mu,\mu\mu}(\tau) + 2i\lambda_{\nu\mu,\nu\nu}] \times [\dot{g}_{\nu\nu,\mu\nu}(\tau) - \dot{g}_{\mu\mu,\mu\nu}(\tau) + 2i\lambda_{\mu\nu,\nu\nu}]\} \tag{B.21}$$

for $\tau > 0$. For $\tau < 0$,

$$K^L_{\mu\nu}(\tau) = [K^L_{\mu\nu}(-\tau)]^* \tag{B.22}$$

These equations use the time derivatives of the line broadening function, $g(t)$, defined in Equation 5.8. The second time derivatives arise from use of the second order cumulant expansion used to calculate $\langle q^{(c)}_{\nu\mu}(\tau) q^{(c)}_{\mu\nu}(\tau)\rangle$, while the single time derivatives come from a single time integration of the correlation functions. Furthermore,

$$K^F_{\mu\nu}(\tau) = \exp\big[- i(\epsilon_\mu - \epsilon_\nu)\tau - g_{\mu\mu,\mu\mu}(\tau) - g_{\nu\nu,\nu\nu}(\tau) + g_{\nu\nu,\mu\mu}(\tau) + g_{\mu\mu,\nu\nu}(\tau) - 2i(\lambda_{\nu\nu,\nu\nu} - \lambda_{\mu\mu,\nu\nu})\tau\big] \tag{B.23}$$

while

$$\lambda_{\mu\nu,\mu'\nu'} \equiv - \lim_{\tau\to\infty} \mathrm{Im}\left[\frac{dg_{\mu\nu,\mu'\nu'}(\tau)}{d\tau}\right] \tag{B.24}$$

Finally, we apply the Markovian approximation to obtain the final kernel for use in Equation 5.14:

$$K_{\mu\nu} \equiv \int_0^\infty dt \bar{K}_{\mu\nu}(t) \tag{B.25}$$

References

[1] W. Zhang, T. Meier, V. Chernyak, and S. Mukamel. Exciton-migration and three-pulse femtosecond optical spectroscopies of photosynthetic antenna complexes. *Journal of Chemical Physics*, Jan 1998.

APPENDIX C

Simulating Optical Responses with Spectron

All the numerical simulations in this thesis have been computed using the Spectron software package, generously provided by the Mukamel group at the University of California-Irvine and Darius Abramavicius of Vilnius University. This appendix contains example input files necessary for calculating spectra for the 2007 Novoderezhkin model, as seen in section 5.2 [3], and for the tight-binding electron-hole model as seen in section C.3 [2]. Additional information can be found in the Spectron user manual [1].

C.1 Overall framework

The input files used within Spectron can be broken down into at least four sections: Registration, System, Bath, and signals. Each section is demarcated by a dollar sign and the section name, and is concluded with an $END command as shown here for the registration section:

```
$REGISTRATION
     LA
     PP
$END
```

Symbol	Meaning
LA	linear absorption (1D)
CD	circular dichroism (1D)
KI	rephasing photon echo (2D)
KII	non-rephasing photon echo (2D)
KIII	double-quantum coherence signal (2D)
KIIIA	double-quantum coherence signal (2D, different projection)
PP	pump-probe (2D)
TDLR	Time domain linear response function (1D)
TDRS	Time domain third order response functions (3D)

Table C.1: List of the signal types available for calculation within Spectron.

The registration section of the input file tells Spectron which optical responses it will be calculating later in the program. For each signal type listed in the $REGISTRATION section, a corresponding section must be included. Signal types are shown in Table C.1; in this appendix we will focus on the linear absorption and the two-dimensional pump-probe spectrum. Note that the 2D pump-probe can also be collected by calculating the rephasing and the non-rephasing signals separately and adding them appropriately. As these signals are computationally expensive to calculate, when looking to calculate absorptive spectra, the pump-probe option will be most efficient.

The $SYSTEM section contains all of the input parameters used to define the system of interest, such as the system hamiltonian and dipoles in the local site basis. The $SYSTEM area will vary depending on the framework used, and will be discussed in more detail within the section for each framework.

The $BATH section is used to define the model of system-bath coupling and will contain parameters for the spectral density. Sample parameters are found in table C.2. The "input-spec-dens" file is a simple text file, formatted as a single column of numbers, ordered as in table C.3

Each signal type listed in the $REGISTRATION section must have a correspond-

Parameter	Value	Comments
`OSCILLATORS_NUM`	1	Number of different bath coordinates
`TEMPERATURE`	77	Temperature (K)
`SPECTRAL_DENSITIES`	input-spec-dens	Numerical spectral density file name

Table C.2: List of the parameters used within the $BATH section of Spectron.

Example	Comments
0	
0	
0	The first five rows are simply 0
0	
0	
20000	Number of frequency points in the file
0	Initial frequency
0.2	Frequency step size
0	C"(ω) begins here
0.702436214819	
1.40476748393	
2.10688891412	
2.80869571708	
...	

Table C.3: The first thirteen lines of an example "input-spec-dens" file, along with comments.

Parameter	Value	Comments
CAL_METHODS	SOS_CGF_F	Calculation method; see Spectron user guide
INI_FREQ	12000	Initial frequency
FIN_FREQ	18000	Final frequency
NUM_FREQ	600	Number of frequency points to calculate
NUM_SHOTS	5000	Number of random draws for averaging
OUT_FILE	output-file.la	Relative path to the desired output file

Table C.4: List of the parameters used within the $LA section for calculating linear absorption spectra within Spectron.

ing section at the end of the input file, describing the parameters desired for each signal type. For readability, I list the parameters from the simulations in section 5.2 in table form in tables C.4 and C.5. Table C.6 gives additional parameters that may be used. Unless otherwise stated, units of frequency will be in wavenumbers (cm^{-1}), dipole strengths in Debye (D), time is in femtoseconds (fs), and length in angstroms (Å). Also note that anytime a file name is given, Spectron will treat it as a relative file path unless the full path is given, so inputs and outputs will appear relative to the directory from which you run Spectron.

C.2 Frenkel framework

The $SYSTEM parameters for the excitonic Frenkel framework are found in Table C.7. Each file here is treated in the site basis; Spectron calculates the excitonic basis from these inputs. All input files are tab-delimited. The "input-hamilonian" file consists of the system Hamiltonian in a lower-triangular form and the "input-dipoles" file has 3 columns for x, y, and z, and one row for each chromophore or site. By default, Spectron assumes that each site is a 3-level system, with the stated anharmonicity; 2-level systems can be used by adding "ELECTRONIC 1" to the $SYSTEM section.

Parameter	Value	Comments
NUM_SHOTS	1500	Number of random draws for averaging
CAL_METHOD	SOS_CGF_G	Calculation method; see Spectron user guide
OPT_POL1	1 0 0	Polarization vector for field 1 (x y z)
OPT_POL2	1 0 0	Polarization vector for field 2 (x y z)
OPT_POL3	1 0 0	Polarization vector for field 3 (x y z)
OPT_POL4	1 0 0	Polarization vector for field 4 (x y z)
OPT_WAV1	0 0 1	Wavevector for field 1 (x y z)
OPT_WAV2	0 0 1	Wavevector for field 2 (x y z)
OPT_WAV3	0 0 1	Wavevector for field 3 (x y z)
OPT_WAV4	0 0 1	Wavevector for field 4 (x y z)
INI_FREQ1	12500	Initial frequency for ν_1
FIN_FREQ1	17500	Final frequency for ν_1
NUM_FREQ1	200	Number of frequency points to calculate for ν_1
INI_FREQ3	12500	Initial frequency for ν_3
FIN_FREQ3	17500	Final frequency for ν_3
NUM_FREQ3	200	Number of frequency points to calculate for ν_3
DEL_TIME2	1000	t_2 value (fs)
OUT_FILE	output-file.pp	Relative path to the desired output file

Table C.5: List of the parameters used within the $PP section for calculating pump-probe spectra within Spectron. These same options may be used in the $KI or $KII sections.

Parameter	Comments
CEN_FREQ1	Central frequency of field 1 for multi-color simulations
WID_FREQ1	Bandwidth of field 1
PULSE_ENVELOPES	8 tab-separated numbers: cen_freq1, wid_freq1, cen_freq2, etc.
ADD_PULSE_ENV	Set to 1 to turn on the previous option
FAKE	Set to 1 to skip signal generation for system test

Table C.6: List of optional parameters that can be used within a signal section to more fully define the optical fields.

Parameter	Value	Comments
SYSTEM_KEYWORD	Excitonic_Disordered_ens__	Specifies the Frenkel framework; see Spectron user guide
NUMMODES	9	Number of chromophores or sites
INP_HAM_L_	input-hamiltonian	Site basis Hamiltonian file
INP_DIP_L_	input-dipoles	Site basis dipole file
ANHARMONICITY	150	Site basis anharmonicity for overtone states
INP_D_2_L_	input-2exc-dipole-corrections	Corrections for dipoles to the 2-exciton manifold
FORM_D_2_L	1	Required for 2-exciton dipole corrections
DISORDER_INTRA_DIAG_GAUSS_F	input-disorder	Input disorder file of standard deviations
SYSTEM_BATH_COUPLING_MM	input-scaling	System-bath coupling/scaling file
TRANSPORT	1	Turns on population transport
REDFIELD_MODIFIED	1	Uses modified Redfield theory

Table C.7: List of the parameters used within the $SYSTEM section in the Frenkel excitonic framework.

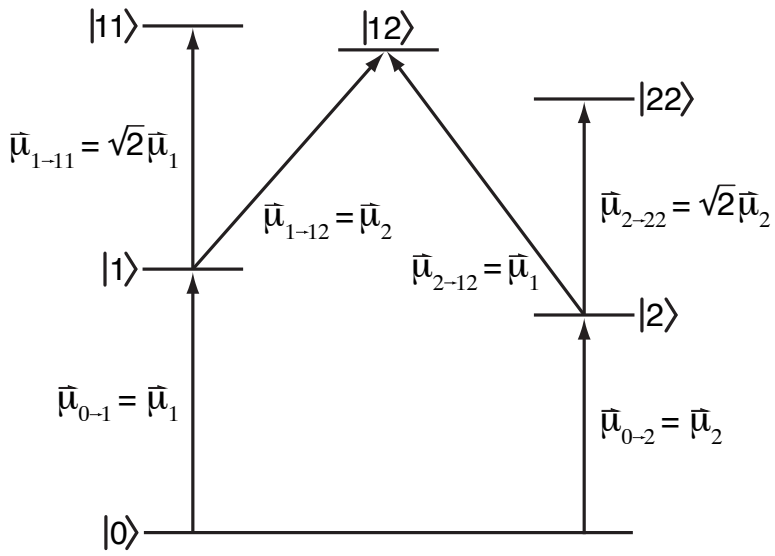

Figure C.1: Diagram depicting the default transition dipoles from the one-exciton to the two-exciton manifolds. Overtone states are assumed to be less strong by a factor of $\sqrt{2}$ while the combination states simply result from both original dipoles.

If diagonal disorder is desired, include the "input-disorder" file. This file contains one row for each site with the standard deviation of the gaussian distribution from which the diagonal energies are to be drawn. (The mean of the distribution is the energy given in the input Hamiltonian.) Be sure to use the `NUM_SHOTS` keyword in your signal sections to include averaging. Unlike the other input files, "input-scaling" is a single row, with one column per site. This file contains multiplicative factors for the spectral density specified in the $BATH section. This allows you to selectively increase (or decrease) the system-bath coupling for any particular site.

While the transition dipoles from the ground to the excited state are explicit inputs in Spectron, the transition dipoles from the one-exciton states to the two-exciton states are not explicitly input. By default, the transitions are given as in figure C.1, where overtone states are a factor of $\sqrt{2}$ weaker than the transition dipole,

and combination states require both individual dipoles to be excited:

$$\begin{aligned} \boldsymbol{\mu}_{j\to jj} &= \sqrt{2}\boldsymbol{\mu}_j \\ \boldsymbol{\mu}_{j\to jl} &= \boldsymbol{\mu}_l \\ \boldsymbol{\mu}_{j\to kl} &= 0, \qquad \text{when } j \neq k, l \end{aligned} \tag{C.1}$$

The Novoderezhkin model treats the overtone states differently, and it disallows combination states that involve both the charge transfer state and one of its constituent chromophores:

$$\begin{aligned} \boldsymbol{\mu}_{j\to jj} &= 0.5\boldsymbol{\mu}_j \\ \boldsymbol{\mu}_{j\to jl} &= \boldsymbol{\mu}_l \\ \boldsymbol{\mu}_{j\to jl} &= 0, \qquad \text{if } j \text{ is a CT state involving chromophore } l \end{aligned} \tag{C.2}$$

The "input-2exc-dipole-corrections" file contains a list of corrections to the default method, and a sample input file is shown in the body of table C.2. The corrections are an additive factor to the default Spectron dipoles. The first line of the file states how many correction rows are in the file: in this case, 10. The subsequent rows have three integers denoting which transition (in the $j \to kl$ notation) is being corrected. The sites are indexed beginning at 0. Since the primary change in the Novoderezhkin model is the transitions to the overtone states, most of the rows involve the $j = k = l$. (Note that $\boldsymbol{\mu}_8$, the CT state, is zero, so the overtone needs no correction.) The last two lines prevent the combination states $|80\rangle$ and $|81\rangle$ from existing since sites 0 and

j	k	l	$\mu_{c,x}$	$\mu_{c,y}$	$\mu_{c,z}$
10					
0	0	0	-2.5726	1.4010	-2.1889
1	1	1	3.6561	-0.0711	-0.0107
2	2	2	3.4057	-0.2311	-1.3117
3	3	3	-2.0937	2.5768	-1.5327
4	4	4	-1.7962	-1.6578	1.2440
5	5	5	0.0850	-1.1982	2.4656
6	6	6	-0.4730	1.6346	3.2368
7	7	7	-0.2896	-3.6091	-0.5130
8	8	0	-2.814	1.5325	-2.3943
8	8	1	3.9992	-0.077742	-0.011742

Table C.8: Example "input-2exc-dipole-corrections" input file, describing corrections to the assumed transition dipoles from the 1-exciton to the 2-exciton manifold.

1 both contribute to the CT state 8. The values given here as calculated as follows:

$$
\begin{aligned}
\boldsymbol{\mu}_{j\to jj}: \qquad \sqrt{2}\boldsymbol{\mu}_j + \boldsymbol{\mu^c}_{j\to jj} &= 0.5\boldsymbol{\mu}_j \\
\boldsymbol{\mu^c}_{j\to jj} &= -0.914214\boldsymbol{\mu}_j \\
\boldsymbol{\mu}_{8\to 80}: \qquad \boldsymbol{\mu}_0 + \boldsymbol{\mu^c}_{8\to 80} &= 0 \\
\boldsymbol{\mu^c}_{8\to 80} &= -\boldsymbol{\mu}_0 \\
\boldsymbol{\mu}_{8\to 81}: \qquad \boldsymbol{\mu}_1 + \boldsymbol{\mu^c}_{8\to 81} &= 0 \\
\boldsymbol{\mu^c}_{8\to 81} &= -\boldsymbol{\mu}_1
\end{aligned}
\tag{C.3}
$$

Parameter	Value	Comments
SYSTEM_KEYWORD	Excitonic_Disordered_CT	Specifies CT framework; see Spectron user guide
NUMSITES	8	Number of sites (does not including CT states)
COO_S	input-coord	File containing coordinates of each site (3 columns, x,y,z)
DIP_X	input-dipoles	File containing transition dipoles for each site (3 columns, x,y,z)
CT_RESTRICTIONS	state-restrictions	File specifying which CT states are allowed
HAM_E	input-elevels	File containing electron energy levels
HAM_EXC	input-energies	File containing transition energies of each site
DECAY_L_WF_E	4.5	Electron decay length
EN_HOPPING_E	350	Electron hopping energy
DECAY_L_WF_H	4.5	Hole decay length
EN_HOPPING_H	350	Hole hopping energy
LENGTH_U_OEH	9	Electron-hole interaction energy cutoff length
LENGTH_U_OEE	9	Electron-electron interaction energy cutoff length
LENGTH_U_OHH	9	Hole-hole interaction energy cutoff length
DISORDER_MOD	34 78	Std. dev. of the disorder distribution for "regular" and CT states
MEAN_2EXC_ESCAPE_RATE	200	The mean 2 exciton escape rate; the inverse of the lifetime
MEDIUM_DIELECTRIC_CONSTANT	1	Dielectric constant used for Coulomb interaction and dipole coupling
ORBITAL_BATH_COUPLING_MM	input-couplings	File containing three matrices for spectral density coefficients
TRANSPORT	1	Turns on population transport
REDFIELD_MODIFIED	1	Uses modified Redfield theory

Table C.9: List of the parameters used within the $SYSTEM section in the charge transfer framework.

	P_{D1}	P_{D2}	Chl_{D1}	Chl_{D2}	$Pheo_{D1}$	$Pheo_{D2}$	$Chlz_{D1}$	$Chlz_{D2}$
P_{D1}	1	1	0	0	0	0	0	0
P_{D2}	0	1	0	0	0	0	0	0
Chl_{D1}	0	0	1	0	0	0	0	0
Chl_{D2}	0	0	0	1	0	0	0	0
$Pheo_{D1}$	0	0	0	0	1	0	0	0
$Pheo_{D2}$	0	0	0	0	0	1	0	0
$Chlz_{D1}$	0	0	0	0	0	0	1	0
$Chlz_{D2}$	0	0	0	0	0	0	0	1

Table C.10: Example "state-restrictions" file (without the header or side labels). A 1 specifies that the combination is allowed, while a 0 is forbidden. The rows indicate the location of the electron, and the columns specify the location of the hole. In this example, one CT state is allowed: $P^{+}_{D2}P^{-}_{D1}$.

C.3 Charge transfer framework

The $SYSTEM parameters for the charge transfer framework are found in table C.9. The `NUMSITES` keyword specifies the number of sites in the model. Note that this does not include any CT states; it is strictly the number of chromophores. The "input-coord" is a text file containing the coordinates of each chromophore in three columns (x,y,z). In these models, I have used the numerical average of the nitrogen atoms in a given chlorophyll molecule, as retrieved from a crystal structure. The "input-dipoles" file is the same is it was for the Frenkel framework: one row for each chromophore, and 3 columns for μ_x, μ_y, and μ_z.

An example of the "state-restrictions" file can be found in Table C.10. This allows you to allow or disallow any particular electron-hole combination. A file with a diagonal matrix of ones will only allow the equivalent of Frenkel excitons. Otherwise, the location of the electron is specified by the row, and the location of the hole is specified by the column.

In the charge transfer framework, we must specify more than the simple transition energy of each molecule; we must specify the relative energies of each electron and hole

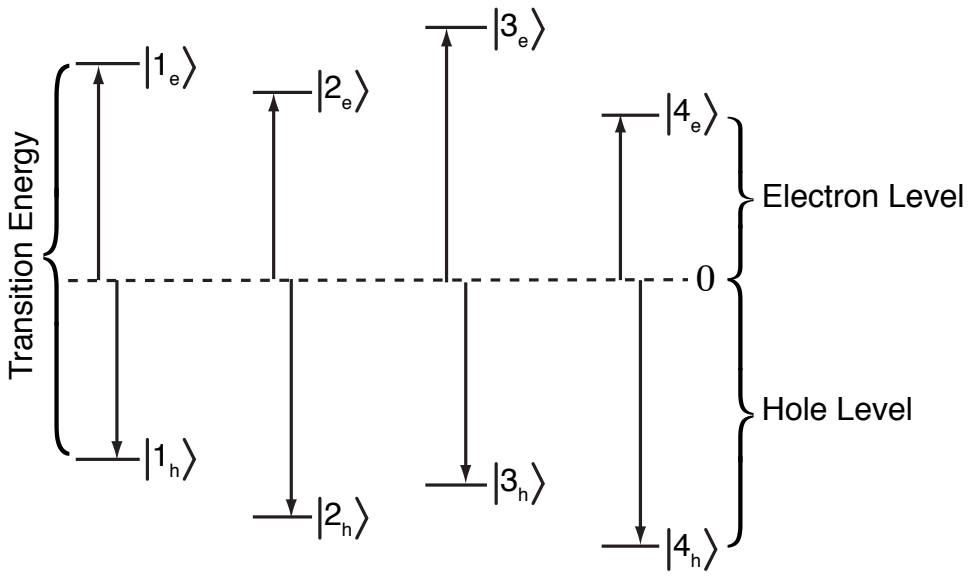

Figure C.2: Diagram depicting the energy level diagram within the CT framework. In this framework, you must specify two of the three quantities: transition energy (HAM_EXC), electron levels (HAM_E), and hole levels (HAM_H).

level, so that the transition energy of a charge transfer state and hopping probabilities can be calculated. A single column of transition energies for each chromophore is contained in the "input-energies" file, while the electron energy levels are given in the "input-elevels" file. An example is found in table C.11.

There are four parameters that determine the rate of electron and hole hopping: `DECAY_L_WF_E`, `EN_HOPPING_E`, `DECAY_L_WF_H`, `EN_HOPPING_H`, where the E denotes electron and the H denotes hole. In general, Spectron allows the rate to differ between them, but we begin with identical electron and hole hopping rates; example parameters are given in table C.9. The rates for both follow the the model:

$$t^{e,h}_{mn,m\neq n} = h^{e,h}_0 \exp\left(-\frac{|\mathbf{r}_m - \mathbf{r}_n|}{l_{e,h}}\right) \tag{C.4}$$

where e, h denotes either hole or electron, $h^{e,h}_0$ refers to either of the `EN_HOPPING_` parameters, and $l_{e,h}$ can be controlled through either of the `DECAY_L_WF_` parameters.

Electron Level
8333.21
8333.21
7000
7000
1778.44
1778.44
12739.84
12739.84

Table C.11: Example "input-elevels" file, giving the electron levels for the 8 chromophores in the photosystem II reaction center.

Three parameters are used to control the strength of the Coulombic interaction between the electrons and holes: `LENGTH_U_OEH`, `LENGTH_U_OEE`, and `LENGTH_U_OHH`, control the interactions between electron-hole pairs, electron-electron pairs, and hole-hole pairs, respectively. The value given for this length is a cutoff frequency, to set the interaction energy to be finite at zero. The model used for each of these is as follows:

$$V_{mn}^{eh,ee,hh} = \begin{cases} \frac{V_0^{eh,ee,hh}/\epsilon}{|\mathbf{r}_m - \mathbf{r}_n|} & \text{for } |\mathbf{r}_m - \mathbf{r}_n| > R_0^{eh,ee,hh} \\ \frac{V_0^{eh,ee,hh}/\epsilon}{R_0^{eh,ee,hh}} & \text{for } |\mathbf{r}_m - \mathbf{r}_n| \leq R_0^{eh,ee,hh} \end{cases} \tag{C.5}$$

where $R_0^{eh,ee,hh}$ is the length parameter given in table C.9. If the length parameters are not specified in the input file, the default value is 5Å. Note that $V_0^{eh,ee,hh}$ can also be varied using the following keywords: `STRENGTH_U_OEH`, `STRENGTH_U_OEE`, and `STRENGTH_U_OHH`. If these are not specified, the default value is the standard interaction strength for two charges:

$$V_0^{eh,ee,hh} = \frac{q_e^2}{4\pi\epsilon_0} \tag{C.6}$$

As in the Frenkel framework, diagonal disorder is included by drawing the value for the transition energy of any given state from a Gaussian distribution with the

mean given by the input values and the standard deviation given by `DISORDER_MOD`. This framework allows for chromophoric states and charge transfer states to have separate standard deviations and both are given in the input file, separated by a tab.

This framework also allows for interaction strengths to be scaled by using an effective dielectric constant. This scales the Coulombic interactions seen in equation C.5 as well as the dipole-dipole couplings.

The system-bath coupling is handled slightly differently in the charge transfer framework. Electron and hole levels of different molecules are allowed to fluctuate independently. The excitonic transition energies then vary according to equation C.7, where $C(\omega)$ is the spectral density given in the \$BATH section, and m_e or m_h indicates the location of the electron or hole. An example of the input couplings file is shown in table C.12.

$$\begin{aligned} C''^{(ee)}_{mm,nn}(\omega) &= \delta_{m_e n_e} \lambda^{ee}_{mn} C(\omega) \\ C''^{(eh)}_{mm,nn}(\omega) &= \delta_{m_e n_h} \lambda^{eh}_{mn} C(\omega) \\ C''^{(he)}_{mm,nn}(\omega) &= \delta_{m_h n_e} \lambda^{he}_{mn} C(\omega) \\ C''^{(hh)}_{mm,nn}(\omega) &= \delta_{m_h n_h} \lambda^{hh}_{mn} C(\omega) \end{aligned} \tag{C.7}$$

The total spectral density becomes:

$$C''_{mm,nn}(\omega) = C''^{(ee)}_{mm,nn}(\omega) + C''^{(eh)}_{mm,nn}(\omega) + C''^{(he)}_{mm,nn}(\omega) + C''^{(hh)}_{mm,nn}(\omega) \tag{C.8}$$

The "input-couplings" file contains the λ^{ee},λ^{eh}, and λ^{hh} matrices. Note that $\lambda^{eh}_{mn} = \lambda^{he}_{nm}$, so only λ^{eh}_{nm} is given. Two of the matrices, λ^{ee} and λ^{hh} are symmetric, and are thus given in lower triangular form in the file, while λ^{eh} is not symmetric in general.

Example "input-couplings" file							
0.8							
0	0.8						
0	0	0.8					
0	0	0	0.8				
0	0	0	0	0.8			
0	0	0	0	0	0.8		
0	0	0	0	0	0	0.8	
0	0	0	0	0	0	0	0.8
-0.3	0	0	0	0	0	0	0
0	-0.3	0	0	0	0	0	0
0	0	-0.3	0	0	0	0	0
0	0	0	-0.3	0	0	0	0
0	0	0	0	-0.3	0	0	0
0	0	0	0	0	-0.3	0	0
0	0	0	0	0	0	-0.3	0
0	0	0	0	0	0	0	-0.3
0.8							
0	0.8						
0	0	0.8					
0	0	0	0.8				
0	0	0	0	0.8			
0	0	0	0	0	0.8		
0	0	0	0	0	0	0.8	
0	0	0	0	0	0	0	0.8

Table C.12: Example "input-couplings" file, giving the λ^{ee},λ^{eh}, and λ^{hh} matrices. This set of matrices gives an effective scaling factor of 1 for chromphoric states and 1.6 for charge transfer states.

Parameter	Value	Comments
PRINT_HAM_1	1	Prints 1-exciton Hamiltonian in the site basis
PRINT_EVALUES	1	Prints 1-exciton eigenvalues
PRINT_EVECTORS	1	Prints 1-exciton eigenvectors
PRINT_EL_DIPOLES_1	1	Prints 1-exciton transition dipoles
PRINT_REDFIELD_M	1	Prints non-zero Redfield tensor components
PRINT_POPULATION_M	1	Prints population transport rate matrix
PRINT_EIGENVALUES_2	1	Prints 2-exciton eigenvalues
PRINT_EIGENVECTORS_2	1	Prints 2-exciton eigenvectors

Table C.13: List of the some of the common variables that can be printed to standard out. The keywords printed here can be used in either the Frenkel or CT frameworks.

C.4 Running Spectron

Spectron is compiled and run in a UNIX environment. The executable is located within the installation directory, which contains Spectron's version number: `spectron-2.8.1-mpi.debug/bin/spectron2`. The `-v` flag turns on verbose mode, allowing for additional parameters to be printed during execution. The `-i` flag precedes the relative path to the input file. For the Frenkel framework, an additional flag specifying the units used is necessary: `-u de_an_cm`. Standard output can be redirected to a log file using `>relative/pathtologfile.log` immediately following the input file name. Including the keywords from Table C.13 in any given $SYSTEM section will print additional parameters to the screen or the log file.

The output file from a linear absorption calculation will be a text file with two columns: Frequency (cm^{-1}) and Signal (AU). A 2D calculation will contain 6 columns: Frequency 1 index, Frequency 3 index, Frequency 1 value (cm^{-1}), Frequency 3 value (cm^{-1}), Signal amplitude (real portion), and Signal amplitude (imaginary portion). Note that in these calculations the imaginary component of the pump-probe signal corresponds to an absorptive spectrum.

References

[1] D. Abramavicius and C. Falvo. Spectron user manual. Distributed with Spectron code.

[2] D. Abramavicius and S. Mukamel. Energy-transfer and charge-separation pathways in the reaction center of photosystem II revealed by coherent two-dimensional optical spectroscopy. *Journal of Chemical Physics*, Jan 2010.

[3] V. I. Novoderezhkin, J. P. Dekker, and R. van Grondelle. Mixing of exciton and charge-transfer states in photosystem II reaction centers: modeling of Stark spectra with modified Redfield theory. *Biophysical Journal*, 93(4):1293–1311, 2007.

APPENDIX D

Simulating the Renger model

We also consider a recent model of the Renger group [1, 2]. Unlike the Novoderezhkin model in Section 5.2, the Renger model is not fully excitonic. Instead, it compartmentalizes the chromophores. The six innermost chromophores are treated excitonically with their own modified Redifield theory [3].[1] The peripheral chlorophylls are treated individually, and transfer from the peripheral chromophores is treated using modified Förster theory [5, 6].

D.1 System Hamiltonian

The system Hamiltonian is shown in Table D.1. Site energies were previously optimized through a genetic algorithm fit to different linear spectroscopies, including absorption, linear dichroism, circular dichroism, and fluorescence spectra [2] although the site energy of $\mathrm{Chl}_{\mathrm{D1}}$ was allowed to vary freely. The couplings between the chromophores were primarily derived via the ab initio TrEsp (transition charge from electrostatic potential) method [7]. This method fits transition charges from the electrostatic potential derived from time-dependent density functional theory for the 3.0

[1] The Renger version of modified Redfield theory uses harmonic oscillators as opposed to the brownian oscillators of Zhang et al. [4].

	P_{D1}	P_{D2}	Chl_{D1}	Chl_{D2}	$Pheo_{D1}$	$Pheo_{D2}$	$Chlz_{D1}$	$Chlz_{D2}$
P_{D1}	15015							
P_{D2}	150	15015						
Chl_{D1}	-42	-60	14749					
Chl_{D2}	-53	-36	7	14993				
$Pheo_{D1}$	-6	21	47	-5	14881			
$Pheo_{D2}$	17	-3	-4	35	3	14815		
$Chlz_{D1}$	1	1	3	0	-4	0	14993	
$Chlz_{D2}$	1	1	0	2	0	-4	0	14970

Table D.1: The system hamiltonian used in the 2008 Renger model [1], with couplings derived from a TrEsp calculation [7].

Å crystal structure [8]. The charges are rescaled to give an effective transition dipole strength of 4.4 D for Chl *a* and 3.4 D for Pheo. The coupling between P_{D1} and P_{D2} was optimized by the fits to the spectra. This model did not specify parameters for a two-exciton Hamiltonian.

As in the Novoderezhkin model, the authors incorporate static disorder by allowing each transition energy to be drawn from a Gaussian distribution centered around the value in Table D.1 and averaging over many such draws. For each chromophore, the FWHM of this distribution is 200 cm^{-1}, although this value was allowed to vary freely for Chl_{D1} and eventually set to be 120 cm^{-1}.

While the Renger model does not permanently include a charge transfer state, this model is used to calculate difference spectra: when calculating the spectra of a complex involving charge transfer, any pigment that is oxidized (or reduced) is removed from the system. In addition, they calculate the electrochromic shifts of the other pigments due to the presence of an additional positive (or negative) charge:

$$\Delta E = \frac{1}{4\pi\epsilon_{\text{eff}}} \sum_i \delta q_i \frac{\mathbf{r_i}}{|\mathbf{r}_i|^3} \Delta\boldsymbol{\mu} \tag{D.1}$$

The authors use a 15° rotation from the N_B-N_D axis towards the N_C atom for $\Delta\boldsymbol{\mu}$, and choose $\epsilon_{\text{eff}} = 2$ for cryogenic temperatures.

D.2 System-bath interactions

The spectral density used in the Renger model was extracted [9] from fluorescence line-narrowing experiments of B777-complexes [10]:

$$J(\omega) = \sum_{i=1,2} \frac{s_i}{7!2\omega_i^4} \omega^3 e^{-(\omega/\omega_i)^{1/2}} \tag{D.2}$$

with $s_1 = 0.4$, $s_2 = 0.25$, $\omega_1 = 0.557$ cm^{-1}, and $\omega_2 = 1.936$ cm^{-1}. In order to compare this spectral density to the Novoderezhkin model, we use $C''(\omega) = \omega^2 J(\omega)$ as our input into Spectron to account for the differences in notation between the two implementations of modified Redfield theory. This overall spectral density has an ω^5 dependence. This strong frequency dependence drastically changes the behavior of $\frac{dC''(\omega)}{d\omega}$ as $\omega \to 0$ as compared to an overdamped brownian oscillator model. In the overdamped brownian oscillator, $\lim_{\omega\to 0} \frac{dC''(\omega)}{d\omega} =$ constant, while $\lim_{\omega\to 0} \frac{dC''(\omega)}{d\omega} = 0$ in this model. When this limit is zero, Spectron returns oscillitory behavior in the linear absorption. Therefore, we add a small OBO component to the spectral density, seen in Figure D.1 with the bold green line.

D.3 Additional considerations

The Renger model includes many slight variations from the modified Redfield theory implemented in Spectron. As I mentioned earlier, the Renger model uses modified Förster theory to describe the rate of transfer from the peripheral chlorophylls to the central pigments:

$$k_{\mathrm{n}\to\mathrm{M}} = \frac{2\pi}{\hbar^2} |V_{\mathrm{nM}}|^2 \int_{-\infty}^{\infty} d\omega D_{\mathrm{I}}^{(\mathrm{n})}(\omega) D_{\mathrm{M}}(\omega) \tag{D.3}$$

where n represents a localized state (in this case, a peripheral chlorophyll), M represents an excitonic state, and V_{nM} is the coupling between site n and exciton M, given by $V_{\mathrm{nM}} = \sum_{\mathrm{m}} V_{\mathrm{nm}} c_{\mathrm{m}}^{(\mathrm{M})}$. The rate is given by the integral of the fluorescence lineshape

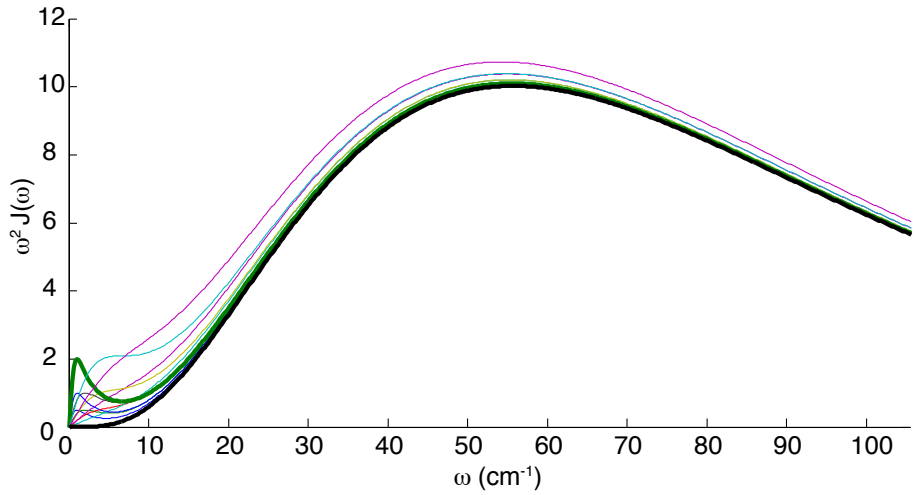

Figure D.1: The bold black line is the original spectral density in the Renger model. The bold green line is the spectral density used within the Spectron calculations, incorporating an OBO component. The unbolded spectral densities all returned oscillatory behavior in the linear absorption.

of the donor, $D_{\mathrm{I}}^{(\mathrm{n})}(\omega)$ and the absorption of the of the excitonic state, $D_{\mathrm{M}}(\omega)$.

Additionally, the Renger framework of modified Redfield theory includes additional reorganization effects due to the off-diagonal part of the exciton-phonon coupling (the last term in Equation D.4):

$$\omega_{\mathrm{adjusted}} = \omega_{\mathrm{M}} - \gamma_{\mathrm{MM}} E_\lambda/\hbar + \sum_{\mathrm{K}} (1 - \delta_{\mathrm{MK}}) \gamma_{\mathrm{MK}} \tilde{C}^{(\mathrm{Im})}(\omega_{\mathrm{MK}}) \tag{D.4}$$

where E_λ is the reorganization energy, and

$$\gamma_{\mathrm{MK}} = \sum_{\mathrm{m,n}} e^{R_{\mathrm{mn}}/R_{\mathrm{c}}} c_{\mathrm{m}}^{(\mathrm{M})} c_{\mathrm{m}}^{(\mathrm{K})} c_{\mathrm{n}}^{(\mathrm{M})} c_{\mathrm{n}}^{(\mathrm{K})} \tag{D.5}$$

where R_{c} is the correlation radius of protein vibrations, and $c_{\mathrm{m}}^{(\mathrm{M})}$ is the exciton coefficient for transforming from the site basis to the exciton basis: $|M\rangle = \sum_m c_{\mathrm{m}}^{(\mathrm{M})} |\mathrm{m}\rangle$. The value was set at 5 Å, although they found the spectra were not critically dependent on it. This term is also used to calculate the exciton relaxation dephasing

time:

$$\tau_{\mathrm{M}}^{-1} = \sum_{\mathrm{K}} \gamma_{\mathrm{MK}} \tilde{C}^{(\mathrm{Re})}(\omega_{\mathrm{MK}}) \tag{D.6}$$

Neglecting these additional reorganization effects and setting τ_{M}^{-1} to zero recovers the lineshape of the modified Redfield theory used in Spectron and the Novoderezhkin model.

Again, the Renger model does not include an optical charge transfer state, although it does include an additional decay constant attributed to electron transfer:

$$k_{\mathrm{et}} = \sum_{\mathrm{M}} \frac{e^{-\epsilon_{\mathrm{M}}/kT}}{\sum_{\mathrm{N}} e^{-\epsilon_N/kT}} e^{-\epsilon_{\mathrm{N}}/kT} \left| c_{\mathrm{donor}}^{(M)} \right|^2 k_{\mathrm{intr}} \tag{D.7}$$

where ϵ_{M} is the energy of exciton M, $\left| c_{\mathrm{donor}}^{(M)} \right|^2$ is the probability of the electron donor participating in state M, and k_{intr} is the intrinsic rate for electron transfer from the donor and a neighbor.

D.4 Results

The linear absorption spectrum calculated in Spectron for our "almost" Renger model is shown in figure D.2 for 2500 instances of disorder. This calculation neglects the components of the model listed in Section D.3. Clearly the compromises made to the Renger model in order to use Spectron are detrimental to the model; the linear absorption obtained here neither matches their published results, nor experimental data. As a result, we did not pursue computationally expensive simulations of 2D spectra since good agreement with the linear absorption spectrum is a prerequisite.

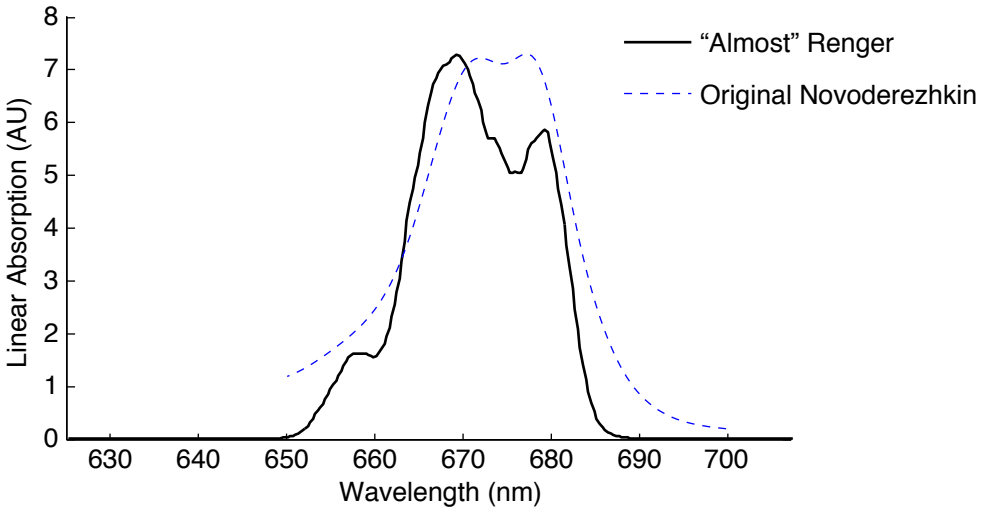

Figure D.2: The 77K linear absorption for the Renger model as it is able to be implemented in Spectron, averaged over 2500 instances of disorder.

References

[1] G. Raszewski, B. A. Diner, E. Schlodder, and T. Renger. Spectroscopic properties of reaction center pigments in photosystem II core complexes: revision of the multimer model. *Biophysical Journal*, 95(1):105–119, 2008.

[2] G. Raszewski, W. Saenger, and T. Renger. Theory of optical spectra of photosystem II reaction centers: location of the triplet state and the identity of the primary electron donor. *Biophysical Journal*, Jan 2005.

[3] T. Renger and R. A. Marcus. Variable-range hopping electron transfer through disordered bridge states: Application to DNA. *Journal of Physical Chemistry A*, 107, Sep 2003.

[4] W. Zhang, T. Meier, V. Chernyak, and S. Mukamel. Exciton-migration and three-pulse femtosecond optical spectroscopies of photosynthetic antenna complexes. *Journal of Chemical Physics*, Jan 1998.

[5] Z. Fetisova, A. Freiberg, K. Mauring, V. Novoderezhkin, A. Taisova, and K. Timpmann. Excitation energy transfer in chlorosomes of green bacteria: theoretical and experimental studies. *Biophysical Journal*, Aug 1996.

[6] H. Sumi. Theory on rates of excitation-energy transfer between molecular aggregates through distributed transition dipoles with application to the antenna system in bacterial photosynthesis. *Journal of Physical Chemistry B*, Dec 1998.

[7] M. E. Madjet, A. Abdurahman, and T. Renger. Intermolecular Coulomb couplings from ab initio electrostatic potentials: application to optical transitions of strongly coupled pigments in photosynthetic antennae and reaction centers. *Journal of Physical Chemistry B*, Aug 2006.

[8] B. Loll, J. Kern, W. Saenger, A. Zouni, and J. Biesiadka. Towards complete cofactor arrangement in the 3.0 Å resolution structure of photosystem II. *Nature*, Jan 2005.

[9] T. Renger and R. A. Marcus. On the relation of protein dynamics and exciton relaxation in pigment-protein complexes: An estimation of the spectral density and a theory for the calculation of optical spectra. *Journal of Chemical Physics*, 116(22), Jun 2002.

[10] T. M. H. Creemers, C. A. De Caro, R. W. Visschers, R. van Grondelle, and S. Völker. Spectral hole burning and fluorescence line narrowing in subunits of the light-harvesting complex LH1 of purple bacteria. *Journal of Physical Chemistry B*, Oct 1999.

APPENDIX E

Reduced Photosystem II Reaction Centers

E.1 Experimental studies

One way of elucidating the charge transfer pathways involved in photosystem II is to block one or more pathways by pre-reducing the system. In photosystem II reaction centers, this can be done by chemically reducing the pheophytin. Using a sodium dithionite treatment as laid out in Appendix A.1.3, we can effectively block charge transfer to the pheophytin. By comparing the 2DES and 2D DAS of the reduced and the un-reduced versions, we can see if the spectral signatures we assigned to the charge transfer to the pheophytin are indeed eliminated or reduced.

We have completed some preliminary work on the reduced photosystem at 77K. The data has been taken and post-processed in the same manner as the original data from Chapter IV. In general, the lineshapes observed are quite similar, so I show the spectrum only for $t_2 = 1.5$ ps, and compare it to the original data (Figure E.1). The color scale for each spectrum is relative to the maximum and minimum of each respective data set. Since the reduced data has a lower amplitude, it implies that the signal has a larger decay relative to the maximum signal compared to the

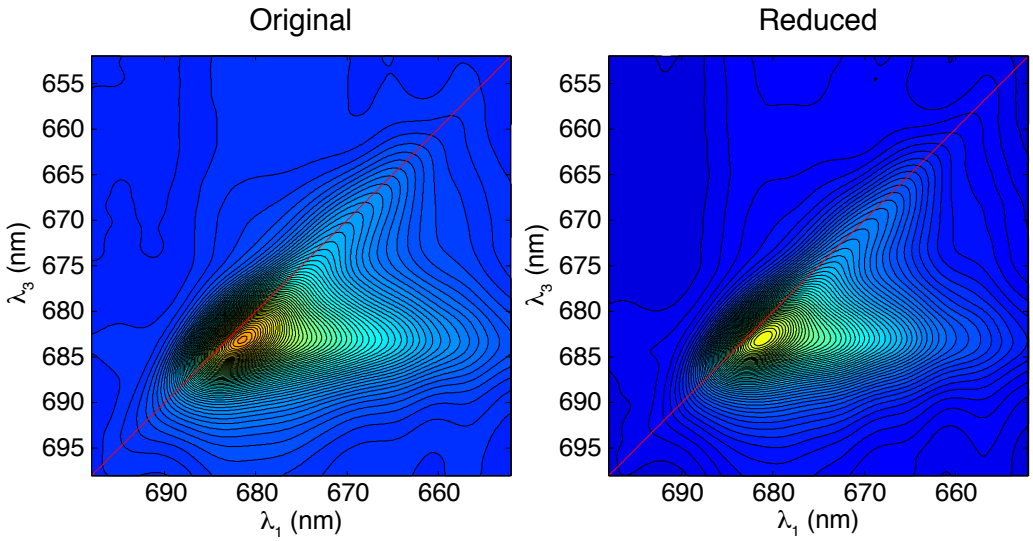

Figure E.1: A comparison of the original data (left) with the chemically reduced sample (right) at $t_2 = 1.5$ps. The color scale on each spectrum is scaled to the maxima and minima of its respective data set.

original data. Additionally, while the lineshapes are quite similar, we note that the reduced data does not have as broad (in λ_1) a crosspeak as the original data, perhaps indicating that the decay pathway for the bluest states is altered.

I also show the preliminary 2D DAS for the reduced data. Within the critical 1-4 ps window for charge transfer, we notice that the lifetimes in the diagonal region are much less heterogeneous than they are in the corresponding original data (see Figure 4.7). The peak in the weighted histogram also shifts from just over 2 ps in the original data to approximately 1 ps in the reduced data. This suggests that the charge transfer pathway supposed to have a 3 ps lifetime is no longer available to the system, and that the 3 ps lifetime correspons to the pathway involving the pheophytin, consistent with the work of Romero et al. [1].

Additionally, when looking at the 5-80 ps regime, we notice that the broad histogram peak from 40-60 ps in the original data is largely absent here. Since this region is presumed to be from secondary charge transfer events (both of which involve the pheophytin), the reduced data supports this statement. Future experiments

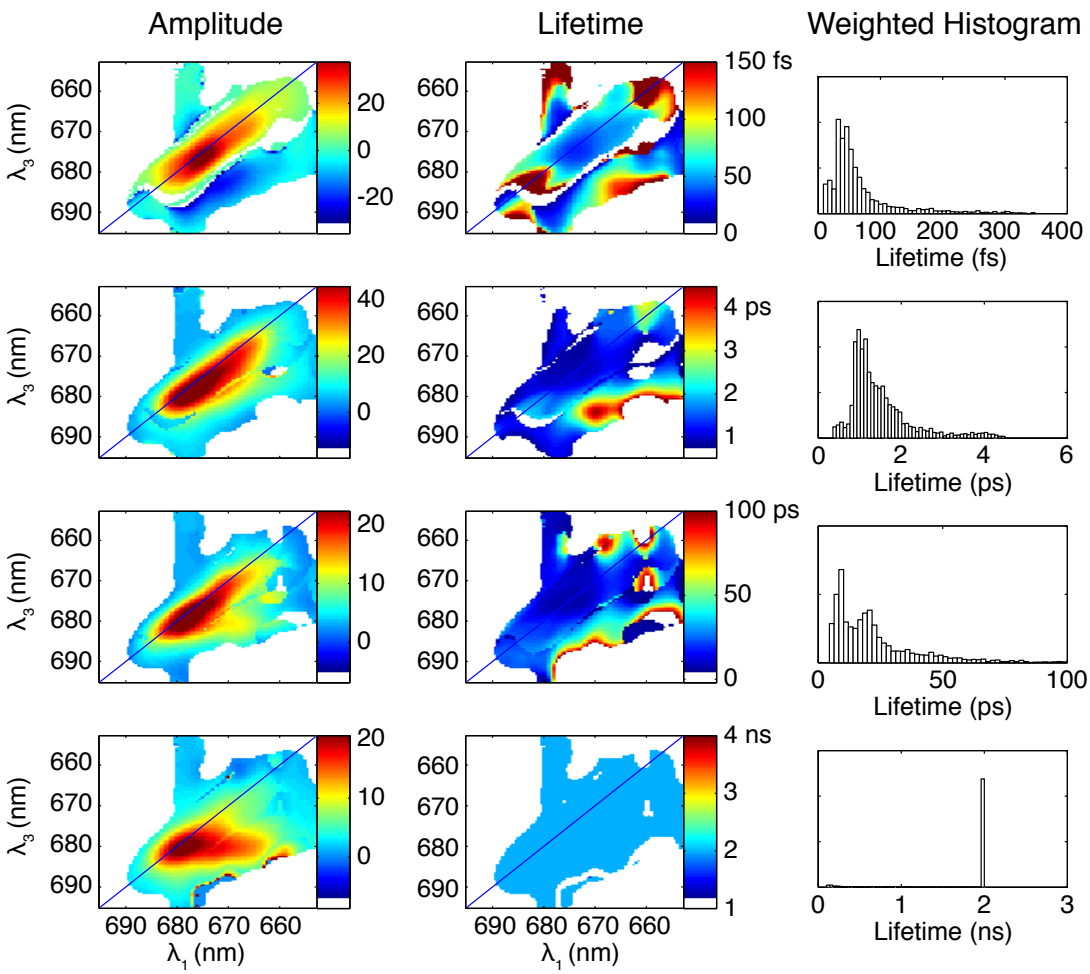

Figure E.2: The preliminary 2D DAS for the chemically reduced photosystem II reaction center at 77K.

with reduced reaction centers will be used to refine and clarify the analysis presented here.

E.2 Modeling

In addition to the reduced PSII experiments, we also plan on modeling the response of the reduced systems. In order to incorporate a negative charge on the pheophytin within the framework of the models, we will need to add appropriate electrochromic shifts of the nearby pigments. Raszewski, Saenger, and Renger [2]

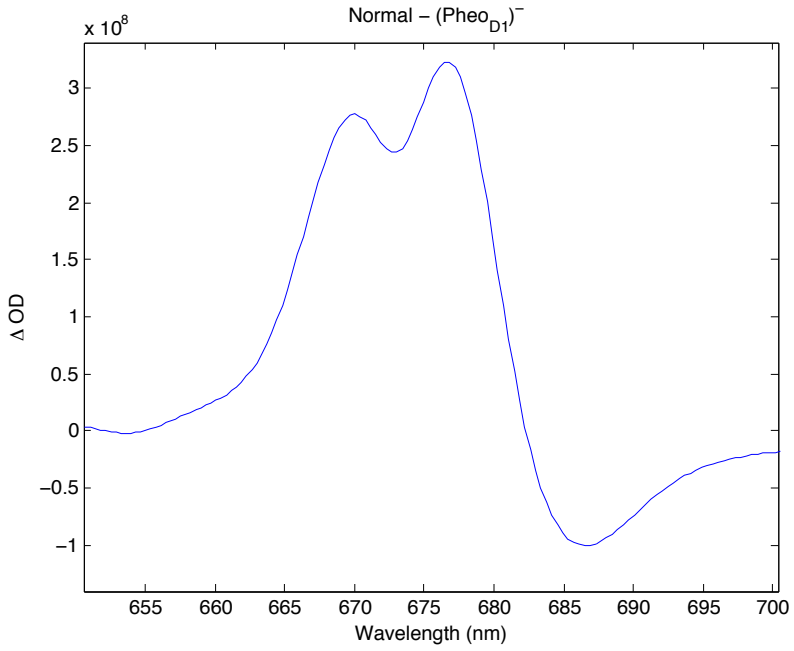

Figure E.3: A simulated difference linear absorption spectrum for the photosystem II reaction center.

have previously incorporated an electrochromic shift when calculating triplet-singlet spectra of photosystem II reaction centers:

$$\Delta E = \frac{1}{4\pi\varepsilon_{\text{eff}}} \sum_i \delta q_i \frac{\mathbf{r}_i}{r_i^3} \Delta\boldsymbol{\mu} \tag{E.1}$$

In the above equation, δq_i represents the partial charges on the atoms where the charge resides, ε_{eff} is an effective dielectric constant, and $\Delta\boldsymbol{\mu} = \boldsymbol{\mu}_e - \boldsymbol{\mu}_g$ represents the change in the permanent dipole moment of the excited and ground state. For chlorophylls, this has been found to have a value of ∼1 D, and is roughly oriented in the N_B-N_D direction [3]. In Renger's implementation of including reduced pigments, he additionally neglected the oscillator strength and couplings of the charged pigment.

We calculated a difference absorption spectrum for the original Novoderezhkin model [4] minus a reduced version, including the electrochromic shifts and neglecting the D1 pheophytin. We assumed the charge was evenly distributed amongst the four

central nitrogen atoms of the pheophytin. Although more complicated models of charge distribution could be used, ΔE was quite small, and the distance effects are unlikely to be significant.

This is a relatively simple way of including a reduced pigment with the context of simulations. Neglecting a pigment is not only easier, but it reduces the computational cost of the models as well. In future simulations, however, it will likely be necessary to include the charged pigment, albeit with a shifted absorption and altered couplings. Since we expect the pheophytin is involved in the charge transfer states, it will also be necessary to remove those particular pathways when working with reduced systems.

Within the models presented here, the creation (or population) of a charge transfer state does not alter the other chromophores in the system. In the most recent Novoderezhkin model which aims to fit transient absorption kinetics [5], they incorporate electrochromic shifts into their two-exciton Hamiltonian. Electrochromic shifts are small, but incorporating them upon the creation of a charge transfer state might play a role in fine-tuning the spectra. In the context of current 2D simulations, however, this will not yet provide the greatest benefit in matching simulations to experimental data.

References

[1] E. Romero, I. H. M. van Stokkum, V. I. Novoderezhkin, J. P. Dekker, and R. van Grondelle. Two different charge separation pathways in photosystem II. *Biochemistry*, 49(20):4300–4307, 2010.

[2] G. Raszewski, W. Saenger, and T. Renger. Theory of optical spectra of photosystem II reaction centers: location of the triplet state and the identity of the primary electron donor. *Biophysical Journal*, Jan 2005.

[3] S. Krawczyk. Electrochromism of chlorophyll *a* monomer and special pair dimer. *Biochimica et Biophysica Acta-Bioenergetics*, 1991.

[4] V. I. Novoderezhkin, J. P. Dekker, and R. van Grondelle. Mixing of exciton and charge-transfer states in photosystem II reaction centers: modeling of Stark spectra with modified Redfield theory. *Biophysical Journal*, 93(4):1293–1311, 2007.

[5] V. I. Novoderezhkin, E. Romero, J. P. Dekker, and R. Grondelle. Multiple charge-separation pathways in photosystem II: Modeling of transient absorption kinetics. *ChemPhysChem*, 12(3):681–688, Feb 2011.